

**KINETICALLY-CONTROLLED SYNTHESIS OF MONO-, BI-, AND  
MULTI-METALLIC NANOCRYSTALS**

A Dissertation  
Presented to  
The Academic Faculty

by

Chenxiao Wang

In Partial Fulfillment  
of the Requirements for the Degree  
Doctor of Philosophy in the  
School of Chemistry and Biochemistry

Georgia Institute of Technology  
August 2023

**COPYRIGHT © 2023 BY CHENXIAO WANG**

# KINETICALLY-CONTROLLED SYNTHESIS OF MONO-, BI-, AND MULTI-METALLIC NANOCRYSTALS

Approved by:

Dr. Younan Xia, Advisor  
Department of Biomedical Engineering  
*Georgia Institute of Technology*

Dr. Joseph P. Sadighi  
School of Chemistry and Biochemistry  
*Georgia Institute of Technology*

Dr. Angus P. Wilkinson  
School of Chemistry and Biochemistry  
*Georgia Institute of Technology*

Dr. Andrew J. Medford  
School of Chemical and Biomolecular  
Engineering  
*Georgia Institute of Technology*

Dr. Henry S. La Pierre  
School of Chemistry and Biochemistry  
*Georgia Institute of Technology*

Date Approved: [July 12, 2023]

Dedicated to mom and dad with love.

## ACKNOWLEDGEMENTS

First and foremost, I would like to express my gratitude to my research advisor, Prof. Younan Xia, for his direction and indirection, for his acceptance and encouragement, for his support and criticism. His exemplary work ethics will serve as a lifelong inspiration for me. I am also grateful to my committee members, Profs. Angus Wilkinson, Henry La Pierre, Joseph Sadighi, and Andrew Medford, for their support and advice.

It has been a great pleasure to work with many creative and motivated friends and coworkers during my graduate study. In particular, I owe deep appreciation to Quynh Nguyen for her tremendous help, Dr. Zhiheng Lyu for helping me start my research, Dr. Minghao Xie, Dr. Yifeng Shi, and Dr. Ruhui Chen for the training and discussion they offered, Dr. Annemieke Janssen and Dr. Kyle Gilroy for their valuable career advice, and many other members of the Xia group for their constant help. I wish to thank the staff members at IEN for their support in instrumentation, especially Dr. Mengkun Tian and Dr. Yong Ding for their aid in electron microscopy and far beyond. I would also like to thank Dr. Miaofang Chi, and Dr. Zhennan Huang at ORNL for their provision of crucial data.

Personally, I owe my heartfelt gratitude to my family, and especially my parents, Liming Chen and Jianjun Wang, for their love, support, and trust in me. I hope to reunite with them soon and more often. My companions, Hongyu Su, Shihao Mi, Esteban Rojas-Gatjens, and Zhen Yu, have shared countless memorable moments of my life in Atlanta. They deserve a name at the finale of my doctoral endeavor.

I thank everyone with whom I had the privilege of sharing food and thoughts.

# TABLE OF CONTENTS

<b>ACKNOWLEDGEMENTS</b>	<b>iv</b>
<b>LIST OF TABLES</b>	<b>vii</b>
<b>LIST OF FIGURES</b>	<b>viii</b>
<b>LIST OF SYMBOLS AND ABBREVIATIONS</b>	<b>xi</b>
<b>SUMMARY</b>	<b>xiii</b>
<b>CHAPTER 1. Introduction</b>	<b>1</b>
1.1 Noble-Metal Nanocrystals: Structures, Properties, and Applications	1
1.2 Opportunities and Challenges in Controlling Noble-Metal Nanocrystals	5
1.3 General Strategies for Controlled Synthesis	9
1.3.1 Template-Mediated Growth	9
1.3.2 Dropwise Injection of the Precursor Solution	12
1.4 Scope of This Work	15
1.5 Notes to Chapter 1	17
1.6 References	18
<b>CHAPTER 2. Controlling the Nucleation and Growth of Gold on Amorphous Selenium Nanospheres to Enhance Their Cellular Uptake and Cytotoxicity</b>	<b>23</b>
2.1 Introduction	23
2.2 Results and Discussion	25
2.3 Conclusion	45
2.4 Experimental Section	46
2.5 Notes to Chapter 2	52
2.6 References	52
<b>CHAPTER 3. Synthesis of Palladium@Rhodium Nanocubes with Well-Defined {100} Surface and Controlled Shell Thicknesses</b>	<b>56</b>
3.1 Introduction	56
3.2 Results and Discussion	58
3.3 Conclusion	70
3.4 Experimental Section	71
3.5 Notes to Chapter 3	73
3.6 References	73
<b>CHAPTER 4. Facet-Controlled Synthesis of Platinum-Group-Metal Quaternary Alloys: The Case of Nanocubes and {100} Facets</b>	<b>76</b>
4.1 Introduction	76
4.2 Results and Discussion	79
4.3 Conclusion	102
4.4 Experimental Section	102
4.5 Notes to Chapter 4	107

<b>4.6</b>	<b>References</b>	<b>107</b>
<b>CHAPTER 5. Conclusions and Future Directions</b>		<b>111</b>
<b>5.1</b>	<b>Conclusions</b>	<b>111</b>
<b>5.2</b>	<b>Future Directions</b>	<b>114</b>
<b>5.3</b>	<b>Notes to Chapter 5</b>	<b>116</b>
<b>5.4</b>	<b>References</b>	<b>117</b>

## LIST OF TABLES

Table 3.1	Compositions of the Pd@Rh nanocubes with different shell thicknesses determined using ICP-MS.	63
Table 4.1	Compositions of the Rh@alloy core-shell nanocubes derived from ICP-MS and XPS measurements.	85
Table 4.2	Upper/lower limits and average values of the reaction rates calculated for the Ru, Rh, Pd, and Pt precursors.	95
Table 4.3	ECSAs and total metal loadings of the Rh@alloy cubes, Pd cubes, and Pt/carbon catalyst.	99

## LIST OF FIGURES

Figure 1.1	Schematic illustration of mono-metallic nanocrystals with different shapes.	2
Figure 1.2	Schematic illustration of bi-metallic nanocrystals with different morphologies.	4
Figure 1.3	Plot showing the process of homogeneous nucleation.	9
Figure 1.4	Preparation of Se-stabilized Pt/C catalyst through a galvanic replacement reaction.	11
Figure 1.5	Comparison of one-shot injection and dropwise injection of the precursor solution.	13
Figure 2.1	Galvanic replacement reaction between Se nanospheres and Au precursor at different initial pH values.	27
Figure 2.2	TEM images of the Se–Au nanoparticles obtained at different time points into the synthesis.	28
Figure 2.3	XRD, XPS, and TEM characterizations of the Se–Au Janus nanoparticles.	30
Figure 2.4	TEM images of the Se–Au nanoparticles obtained at different initial pH values.	31
Figure 2.5	Average diameters and numbers of Au nanoparticles on each <i>a</i> -Se nanosphere at different initial pH values.	32
Figure 2.6	TEM image of the Se–Au hybrid nanoparticles prepared using the standard protocol except for the introduction of Au precursor in one shot.	33
Figure 2.7	UV–vis spectra of the <i>a</i> -Se nanospheres and Se–Au hybrid nanoparticles obtained at different initial pH values.	34
Figure 2.8	Concentration of the Au precursor remaining in the reaction solution as a function of reaction time at initial pH of 8.2 and 11.0.	35
Figure 2.9	TEM images of the Se–Au hybrid nanoparticles obtained by adding Au precursor solution in one shot at different temperatures.	37

Figure 2.10	Schematic illustration and TEM images of the Se@Au core-shell nanoparticles.	38
Figure 2.11	TEM image of the Se-Au hybrid nanoparticles prepared using the standard protocol except that CTAB was replaced with KBr and PVP at different pH values.	40
Figure 2.12	FT-IR spectra of folic acid, OPSS-PEG-SVA, OPSS-PEG-FA, and Se-Au <sub>10</sub> -Ligand.	41
Figure 2.13	Plots showing the number of Se-Au hybrid nanoparticles internalized per HeLa cell and the cell viability.	43
Figure 2.14	Florescence micrographs of the HeLa cells that were cultured for 24 h with different Se-Au nanoparticles.	44
Figure 2.15	Fluorescence micrographs of the JC-1-stained HeLa cells that were cultured with different Se-Au nanoparticles.	45
Figure 3.1	TEM and EDX characterizations of the Pd@Rh <sub>3L</sub> nanocubes.	60
Figure 3.2	TEM image of the Pd@Rh nanocubes obtained with Rh(acac) <sub>3</sub> as the precursor.	61
Figure 3.3	XPS spectra of Pd and Rh elements in the Pd@Rh <sub>3L</sub> nanocubes.	61
Figure 3.4	TEM and HAADF-STEM images of the Pd@Rh <sub>0.6L</sub> and Pd@Rh <sub>1.5L</sub> nanocubes.	63
Figure 3.5	CV curves obtained from Pd nanocubes and Pd@Rh nanocubes with different shell thicknesses.	64
Figure 3.6	TEM images of the products obtained with modified protocols for Pd@Rh nanocubes.	66
Figure 3.7	TEM images of the products obtained at different temperatures.	67
Figure 3.8	TEM images recorded during <i>in situ</i> heating of the Pd and Pd@Rh nanocubes.	68
Figure 3.9	TEM characterizations of the Rh nanocages.	70
Figure 3.10	TEM images of the Pd@Rh nanocubes and Rh nanocages prepared by using 6-nm Pd cubes as seeds.	70

Figure 4.1	TEM images and size distributions of the Rh nanocubes and Rh@alloy nanocrystals of different morphologies.	81
Figure 4.2	XRD data of the Rh nanocubes and Rh@alloy nanocubes.	82
Figure 4.3	XPS spectra recorded from the Rh@alloy nanocubes.	84
Figure 4.4	High-resolution XPS spectra of Ru, Rh, Pd, and Pt elements in the Rh@alloy nanocubes.	84
Figure 4.5	XPS valence band structure of the Rh@alloy nanocubes.	85
Figure 4.6	HAADF-STEM and EDX characterizations of the Rh@alloy nanocubes.	86
Figure 4.7	TEM images of the products obtained with modified protocols.	87
Figure 4.8	ICP-MS measurement of the precursor concentrations and reaction rate constants.	88
Figure 4.9	Schematic illustration of the experimental setup and plot showing the instantaneous concentration of the precursor under dropwise addition of the precursor solution.	91
Figure 4.10	Simulated reaction rates under dropwise injection and one-shot injection of the precursor mixture	93
Figure 4.11	TEM images of the product obtained with no addition of the Rh seeds.	96
Figure 4.12	<i>In situ</i> HAADF-STEM images of the Rh@alloy nanocubes recorded after heating at different temperatures.	97
Figure 4.13	EDX characterizations of the Rh@alloy nanocubes after annealing at 500 °C for 30 min.	97
Figure 4.14	ECSA measurement of the Rh@alloy nanocubes, Pd nanocubes, and Pt/carbon catalyst.	99
Figure 4.15	EOR catalytic activities of the Rh@alloy nanocubes, Pd nanocubes, and Pt/carbon catalyst.	100
sFigure 4.16	EDX characterizations of one Rh@alloy nanocube after 75 cycles of CV scanning in the electrolyte containing 1 M KOH and 1 M ethanol.	101

## LIST OF SYMBOLS AND ABBREVIATIONS

AA	ascorbic acid
<i>a</i> -	amorphous
acac	acetylacetonate
ATCC	American Type Culture Collection
CTAB	cetyltrimethylammonium bromide
CV	cyclic voltammetry
DI	deionized
DMEM	Dulbecco's Modified Eagle Medium
DMSO	dimethyl sulfoxide
ECSA	electrochemical active surface area
EDX	energy-dispersive X-ray spectroscopy
$E_F$	Fermi energy level
EG	ethylene glycol
EOR	ethanol oxidation reaction
FA	folic acid
FBS	fetal bovine serum
<i>fcc</i>	face-centered cubic
GC	glassy carbon
HAADF	high-angle annular dark-field
STEM	scanning transmission electron microscopy
Hela	human cervical carcinoma cell line
HRTEM	high-resolution transmission electron microscopy

ICP-MS	inductively-coupled plasma mass spectrometry
MMNPs	Multi-metallic nanoparticles
MTT	3-(4,5-dimethyl-2-thiazolyl)-2,5-diphenyl-2-H-tetrazolium bromide
OPSS-PEG-FA	folic acid-terminated poly(ethylene glycol) disulfide conjugate
OPSS-PEG-SVA	orthopyridyl disulfide poly(ethylene glycol) succinimidyl valerate
ORR	oxygen reduction reaction
PBS	phosphate buffered saline
PGMs	platinum-group metals
PVP	poly(vinyl pyrrolidone)
RHE	reversible hydrogen electrode
ROS	reactive oxygen species
TEG	triethylene glycol
TEM	transmission electron microscopy
UPD	underpotential deposition
UV-vis	ultraviolet-visible
XPS	X-ray photoelectron spectroscopy
XRD	X-ray diffraction

## SUMMARY

Crucial in a myriad of applications ranging from catalysis to biomedicine, noble-metal nanocrystals exhibit physicochemical properties strongly governed by their size, morphology, and composition. The strong correlations offer opportunities to optimize their figures of merit, thereby augmenting their overall effectiveness. As research advances from simple mono-metallic nanocrystals to multi-metallic and hybrid nanostructures with diverse architectures and atomic distributions, the escalating complexity presents synthetic chemists with ever-increasing challenges. In this dissertation, I develop two general strategies, namely template-mediated growth and dropwise injection of precursor, aiming to control the structural characteristics of mono-, bi-, and multi-metallic nanocrystals, while exploring their potential applications in catalysis and biomedicine.

First, amorphous Se nanospheres were employed as templates to mediate the nucleation and growth of Au nanoparticles through a galvanic replacement reaction. By leveraging the reducing power of Se and the pH-sensitive reaction kinetics, precise control over the size and number of Au particles on each Se sphere was achieved, resulting in hybrid nanoparticles with diverse morphologies. The presence of Au patches on these hybrid nanoparticles provides an experimental handle to optimize the ligand distribution, significantly augmenting cellular uptake and cytotoxicity for the Se nanospheres. Shifting focus to a bi-metallic system, I employed Pd cubic nanocrystals as templates to direct the surface deposition of Rh in a layer-by-layer manner. With rigorous regulation of the reaction kinetics, I successfully synthesized Pd@Rh nanocrystals featuring smooth, well-defined {100} facets and large sizes. The strong Rh–Rh binding within the shell imparted

exceptional thermal stability to the core–shell nanocubes. Afterwards, chemical wet etching was employed to fabricate Rh nanocages with well-defined {100} surface and ultrathin walls from the core–shell nanocubes. Building upon these insights, I extended the two strategies to control the composition of complex alloys. By utilizing well-defined and highly stable Rh cubic nanocrystals as templates, together with a tight control over the reduction kinetics through dropwise injection of the precursor mixture, cubic-shaped nanocrystals featuring a nearly equimolar RuRhPdPt alloy surface were obtained. These alloy nanocubes demonstrated superior thermal stability in terms of both shape and composition, along with enhanced catalytic performance toward ethanol oxidation.

# CHAPTER 1. INTRODUCTION

## 1.1 Noble-Metal Nanocrystals: Structures, Properties, and Applications

A noble metal is ordinarily considered as a metallic element that is resistant to corrosion and is usually found in nature as an elementary substance. Most often, Au, Ag, Pt, Pd, Rh, Ir, Ru, and Os are the eight elements classified as noble metals. Constituting a major class of nanomaterials, noble-metal nanocrystals can be broadly defined as noble-metal structures or particles possessing a crystalline lattice and at least one dimension in the range of 1–100 nm. Due to their profound impacts on fundamental sciences and practical applications in the context of plasmonics [1–3], photonics [4–6], electronics [7–9], sensing [10, 11], catalysis [12–14], and biomedicine [15–17], noble-metal nanocrystals represent one of today’s most viable and exciting research topics.

In principle, a nanocrystal should adopt the same crystal structure as its bulk counterpart. In fact, most noble-metal nanocrystals (except Ru) are crystallized in the face-centered cubic (*fcc*) structure under ambient conditions, the same as their intrinsic bulk crystal structure. The crystal structure further dictates the geometric shape of these nanocrystals. Specifically, the high symmetry order of an *fcc* unit cell accounts for the highly symmetric shapes (*e.g.*, cube, cuboctahedron, or octahedron) that are often adopted by these metal nanocrystals. However, the confinement imposed by the inherent symmetry of the crystal structure can be lifted to a certain extent to obtain nanocrystals with exotic shapes [18]. For instance, it is not uncommon to observe two or multiple *fcc* crystal grains combined together to form one whole nanocrystal with singly- or multiply-twinned structures with the corresponding symmetry orders different from the *fcc* crystal lattice.



their aggregation into nuclei, evolution into different types of seeds with distinct internal structures and in diverse symmetry groups (shown in the middle ring), and then growth into nanocrystals with various shapes (depicted in the outer ring). Twin defects or stacking faults are indicated by the red lines, while the {100}, {110}, and {111} facets are represented by the green, purple, and yellow colors, respectively. The light orange color of the outermost ring signifies that the final nanocrystals have reduced symmetry relative to that of the initially formed seeds. Reprinted with permission from ref [18]. Copyright 2023 American Chemical Society.

Going beyond the realm of shape evolution, the architectural diversity of noble-metal nanocrystals can be significantly expanded when two or more distinct metals are brought together. For simplicity, the bi-metallic system can serve as an example to illustrate the concept. Based on the spatial distribution of the two constituent elements, the primary structures that can be adopted by bi-metallic nanocrystals include Janus, core-shell, intermetallic compounds, and alloys. From these foundational structures, a multitude of possible architectures can be achieved, with core-frame, core-satellite, and nanocage being a few notable examples (Figure 1.2) [23]. By manipulating the elemental composition and the spatial distributions of the two elements in the crystal lattice, the properties and performance of bi-metallic nanocrystals can be augmented for diverse applications. For example, the immediate merits and advantages that can be offered by the core-shell structure include: *i*) an avenue to produce cost-effective catalysts by replacing the bulk of a catalytic particle with an inexpensive and abundant metal [24, 25]; *ii*) the ability to process noble metals with high cohesive energies into nanocrystals with well-defined surface structures by replicating the atomic structures of the core [26, 27]; *iii*) the capability to access new crystal phases for the metal in the shell by templating against the atomic packing of the metal in the core [28–30]; and *iv*) an opportunity to enhance the properties of the shell metal by leveraging its electronic and/or geometric interactions with the core, and such enhancement will be particularly strong if the shell thickness is

controlled below six atomic layers [31]. As for the alloy structure, notable examples of novel and enhanced properties include the intensification of localized surface plasmon resonance with the incorporation of Ag into Au nanocrystals [32] and the discovery of highly active fuel cell catalysts by alloying Pt and Ni in a stoichiometric ratio of 3:1 [33]. The current trend toward fabrication of catalysts based on complex multi-metallic alloys or so-called “high-entropy alloys” highlights the increasing importance and urgency in studying alloy nanocrystals [34, 35]. With multiple elements combined into a single particle, the inherent compositional complexity and numerous possible atomic configurations make multi-metallic alloy nanocrystals an innovation platform for the advancement of efficient heterogeneous catalysts [36].

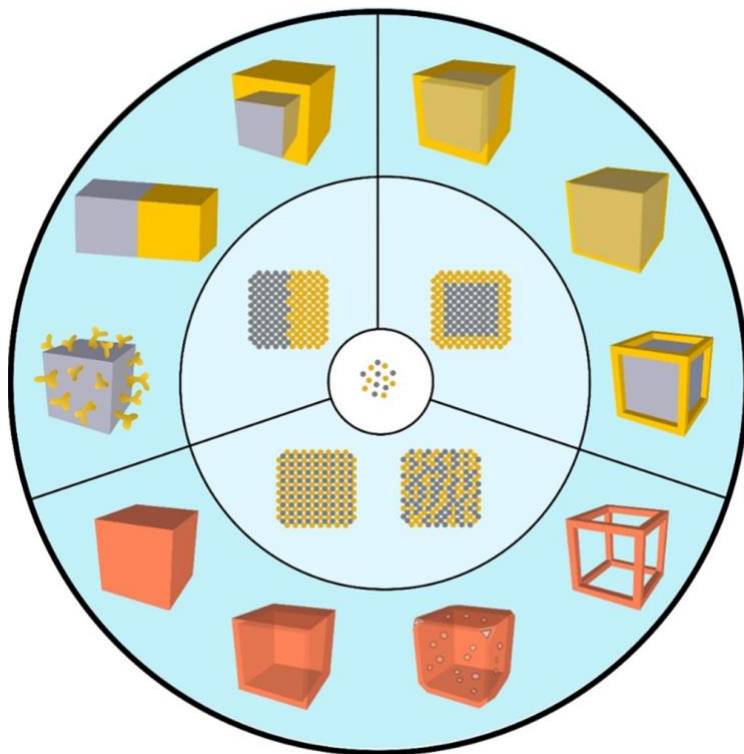


**Figure 1.2.** Schematic illustration depicting the evolution process from two types of metal atoms (yellow and gray) at the center, progressing to four types of atomic distributions in the middle ring, and then a diverse array of bi-metallic nanocrystals with distinct

architectures in the outer ring. The presence of an alloy or intermetallic compound is represented by an orange color, signifying the integration and blending of the two different metal atoms. Reprinted with permission from ref [23]. Copyright 2016 American Chemical Society.

In addition to the combination of metals, the integration of metallic and nonmetallic components into hybrid nanostructures offers a promising avenue to broaden the scope of nanoscale synthesis and achieve heterogeneous systems with a variety of new properties. These hybrid nanoparticles not only manifest a combination of the original properties of their constituents but also holds the potential to reveal unique synergistic effects. For example, among a myriad of possible hybrid architectures, the metal-semiconductor nanojunction is of particular interest as a basis for their utilization in photocatalysis, bioimaging, and photothermal therapies owing to the light-induced charge-separation characteristic [37].

## **1.2 Opportunities and Challenges in Controlling Noble-Metal Nanocrystals**

Starting as a scientific curiosity, research on nanocrystals has spanned from the development of methods for engineering their properties in a controllable manner to the exploration of new applications superior to their bulk counterparts, which is a result of the realization that the properties and applications of nanocrystals could be greatly augmented by posing a tight control over their internal structure [38, 39], size [40–42], morphology [43–45], and elemental composition [23, 46].

For mono-metallic nanocrystals, size and geometric shape are primary determinants of numerous physicochemical properties as they dictate the arrangement of atoms on the surface and influence the distribution of surface charges. A prototypical example of how nanocrystal properties rely heavily on the particle size and geometric shape can be found

in Ag nanocrystals, a class of multifunctional nanomaterials with extensive use in plasmonics, electronics, and catalysis. By simply adjusting the size of polycrystalline Ag nanoparticles in a pseudo-spherical shape within the range of 40–90 nm, the ultraviolet–visible (UV–vis) extinction spectra displayed a tunable resonance peak ranging from 410–500 nm [47, 48]. Transitioning to Ag nanocubes with an edge length of 90 nm would lead to the appearance of multiple resonance peaks in the spectra, with the most intense peak shifting to around 600 nm due to the presence of sharp edges and corners on the surface [47, 49]. In this scenario, the shape of metal nanocrystals provides a more effective means than size to tailor their surface plasmonic properties. When serving as catalysts, Ag nanocubes encased by {100} facets exhibit greater selectivity toward ethylene epoxidation relative to the conventional Ag nanoparticles with a quasi-spherical shape. This advantage arises from the favorable transformation of the surface oxametallacycle intermediate to ethylene epoxide on the Ag(100) surface [50, 51]. Similar correlations between other catalytic properties and size/shape have also been demonstrated for nanocrystals composed of other metals such as Au, Pt, Pd, and Rh [12]. These examples manifest the promise of size and shape controls in augmenting the performance and thereby accomplishing cost-effective utilization of precious metals notoriously known for their scarcity in the Earth’s crust.

When considering bi- and multi-metallic nanocrystals, the morphology and elemental distribution become two pivotal factors that govern their properties. In particular, the surface composition and arrangement of atoms play a crucial role in determining their potential in industrially important applications. The PdPt bi-metallic system can serve as an example to illustrate the strong relationship between the surface structure and their

performance as heterogeneous catalysts, the major use of these two elements. Through rationally designed synthetic protocols, PdPt nanocrystals can be prepared as Pd–Pt alloys or Pd@Pt core–shell structures [52]. When comparing these two structures in terms of their catalytic activity toward the oxygen reduction reaction (ORR), it is evident that the Pd@Pt core–shell nanocrystals exhibit significantly higher specific and mass activities than the alloys. The substantial enhancement observed in the core–shell structure can be attributed not only to the increased exposure of Pt—the catalytically more active element—on the nanocrystal surface but more essentially to the geometric and ligand effects inherent in the core–shell interaction [53–55]. Furthermore, this interplay can be manipulated by using Pd nanocrystals with different geometric shapes (*e.g.*, cube, octahedron, decahedron, icosahedron) as the core [55–58] or by simply tuning the thickness of the Pt shell during the synthesis [55, 56]. Similar correlations have also been demonstrated in many other combinations of bi- and multi-metallic systems and target reactions, although the influence can vary in a case-specific and sometimes intricate manner [23].

Even with only a limited number of noble-metal elements, nanocrystals can be possibly designed and produced with a nearly infinite variety of compositions, shapes, morphologies, and architectures. This vast landscape of potential developments holds numerous breakthroughs yet to be uncovered. However, along with the opportunities provided by this expanding family of materials comes the growing challenge of comprehending and managing these intricate structural features through chemical processes. Despite the development of numerous synthetic methods aimed at regulating size, morphology, and composition, there remains a growing disparity in our abilities to control these distinct aspects of synthesis.

For size control of mono-metallic nanocrystals, the strategy has proven to be straightforward. As the average size is inversely proportional to the number of particles and directly proportional to the feeding amount of precursor, separation of nucleation and successive template-mediated growth are two simple and efficient routes for precise tuning of nanocrystal size [59, 60]. However, when dealing with more complex structures like Janus and core-shell architectures, controlling the size of each constituent part (*e.g.*, interface area and shell thickness) becomes more challenging. In comparison, achieving morphology control in nanocrystals is a more complicated endeavor. Fundamentally, it is governed by the intrinsic crystal structure, which is typically shared by a group of similar elements [18]. Our progressive knowledge of the thermodynamic and kinetic parameter involved over the past two decades has facilitated systematic shape control of numerous noble metals [12]. Current research efforts aim to apply this knowledge to elements with high surface energies, such as Ir, Rh, and Ru, or to fabricate sophisticated hierarchical structures using well-understood materials such as Au, Ag, Pd, and Pt. On the other hand, composition control poses a significantly more abstruse scientific puzzle yet to be solved. As a prerequisite of control, understanding the composition of nanocrystals and how it is formed has been challenging, as it entails the three-dimensional distribution of multiple elements, which is not nearly as easy to visualize or quantify as shape or size. Even the most advanced tools are deficient to a certain extent when utilized to analyze the surface composition. To gain a better understanding of the composition and ultimately establish general guidelines for synthetic control of these nanomaterials, we need to explore an alternative and often overlooked approach—taking a closer look at the chemical reaction that rules their formation processes.

## 1.3 General Strategies for Controlled Synthesis

### 1.3.1 Template-Mediated Growth

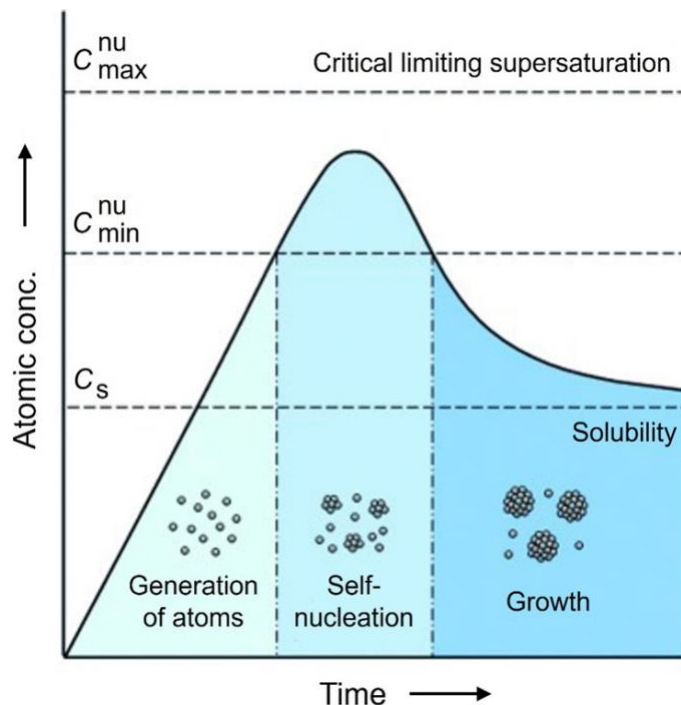


**Figure 1.3.** Plot of the concentration of atoms as a function of reaction time. This plot illustrates the major steps involved in a synthesis, including the generation of atoms, homogeneous nucleation, and growth. Reprinted with permission from ref [61]. Copyright 1950 American Chemical Society.

The synthesis of colloidal metal nanocrystals is traditionally based on the one-pot approach. This process begins with the formation of nuclei or seeds, which are created through the aggregation of freshly generated metal atoms in a homogeneous manner. These nuclei then act as templates to mediate the size increase and shape evolution through surface deposition. This process of particle formation follows the so-called LaMer model established in the 1950s (Figure 1.3) [61, 62]. Typically, the nucleation and growth processes usually happen simultaneously and compete with each other, especially under conditions of high supersaturation of metal atoms. These temporal and spatial variations

can result in polydisperse products, characterized by variations in size, shape, and internal structure.

A solution to address the issue of nonuniformity is to separate growth from nucleation through the introduction of well-defined nanocrystals as pre-formed templates, a technique called “seed-mediated growth” [63]. Through seed mediation, the final shape taken by the product becomes highly correlated with the structure of the seed. For instance, the growth of single-crystal nanocrystals often leads to the formation of cuboctahedral, cubic, octahedral, or rhombic dodecahedral nanocrystals as the final output. Both the initial seed and the product exhibit the same symmetry as the underlying *fcc* unit cells. Remarkably, if these symmetric products are used as seeds for a subsequent overgrowth, nanocrystals with symmetry-broken shapes, such as tetrahedra, rectangular bars, and octagonal rods, will be created [64–66]. Moreover, by employing twinned and stacking-fault-lined nanocrystals as seeds, seed-mediated growth opens up pathways to generate even more exotic shapes [67–69].

It is worth emphasizing that the role of the template extends beyond a physical support. The chemical features of the seed can also be utilized to direct and regulate the growth behavior of metal structures, especially through a spontaneous electrochemical process called “galvanic replacement” [70]. In a galvanic replacement synthesis, atoms from the metal template (substrate) undergo oxidation and dissolution (anode half reaction); meanwhile, electrons are released and transferred to the salt precursor containing another metal with a higher reduction potential (cathode half reaction). Consequently, the precursor is then reduced to form metal atoms that are then deposited onto the substrate. Galvanic replacement can be considered as a chemical redox reaction without the involvement of an

external reducing agent involved or as an electrochemical reaction with no physical separation between the anode and cathode. Notably, a distinctive characteristic of galvanic replacement synthesis is that the overall shape or morphology of the resulting product tends to replicate that of the substrate. For example, the reaction between Ag nanocubes (serving as the template) and  $\text{HAuCl}_4$  (the salt precursor) yields Ag–Au alloy cubic nanocages in a single step, offering an alternative approach for the fabrication of complex metal nanostructures [71].

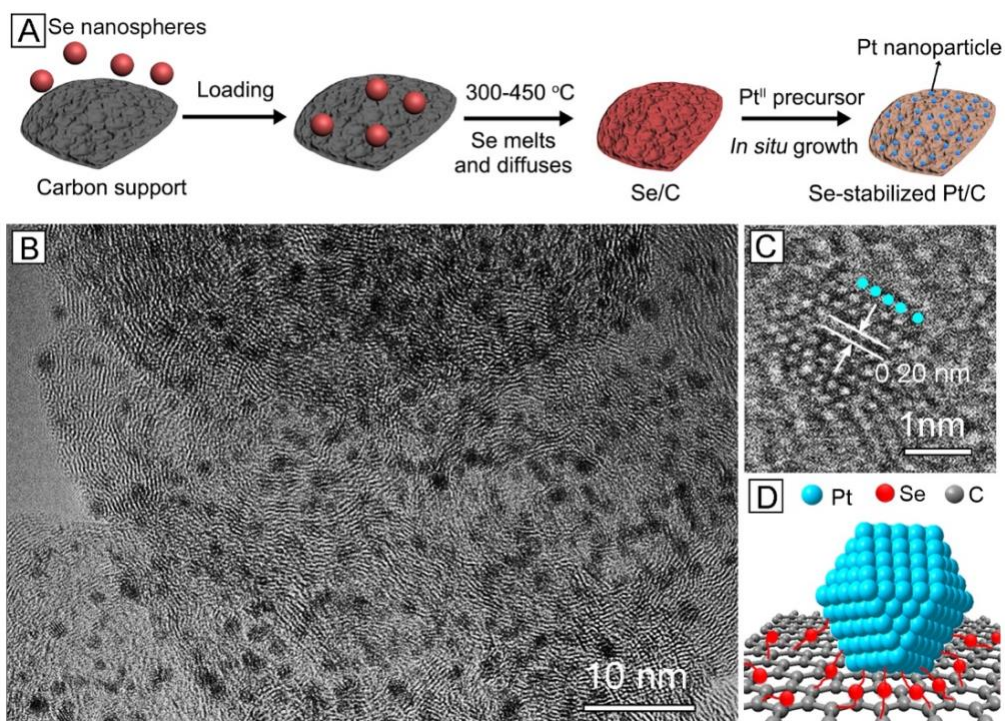


**Figure 1.4.** (A) Schematic showing the preparation of a Se-stabilized Pt/C catalyst. (B) TEM and (C) high-resolution TEM image of the Se-stabilized Pt/C catalyst. (D) Schematic showing how to anchor a Pt nanoparticle to the carbon surface through the Pt–Se–C linkage. Reproduced with permission from ref [75]. Copyright 2019 American Chemical Society.

While metal templates are naturally well-suited for mediating many metal nanostructures owing to their matching crystal structure, high crystallinity, and well-defined attributes, galvanic replacement also can be initiated on reductive nonmetallic

substrates such as Se [72], Te [73], and Si [74]. Due to the large lattice mismatch between these nonmetal elements and most noble metals, distinct surface nucleation and growth behaviors can be anticipated. For instance, the reaction between amorphous Se (*a*-Se) and a Pt precursor on a carbon support allows for the *in situ* synthesis of ultrasmall Pt nanoparticles linked to the Se thin film *via* Pt–Se bonds, generating an electrocatalyst with exceptional stability (Figure 1.4) [75].

### 1.3.2 Dropwise Injection of the Precursor Solution

In a conventional synthesis of colloidal nanocrystals, the precursor is typically introduced *via* “hot injection” or “heat up” method to achieve a tight control over the size distribution of the products [76]. In both approaches, the precursor solution is rapidly injected into the reaction mixture as a single shot (Figure 1.5A), followed by thermally-triggered reaction(s) and burst nucleation to initiate nanocrystal formation. Since nucleation involves a much higher energy barrier than growth, it necessitates a tremendously higher level of supersaturation to commence this process. The one-shot injection method fulfills this requirement by enabling a fast reaction kinetics at the initial stages when the precursor concentration is at its highest level.

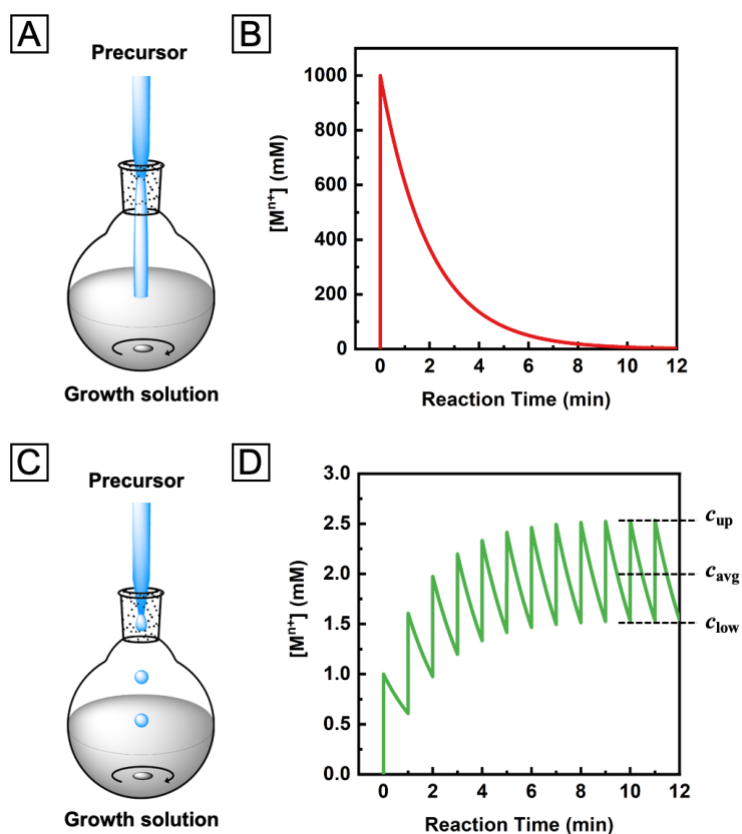


**Figure 1.5.** (A and B) Experimental setup for a colloidal synthesis involving one-shot injection of the precursor solution and plot of the instantaneous concentration of precursor as a function of reaction time.  $c_0 = 1$  M (equals to 1000 droplets of precursor solution),  $k = 0.5$  s<sup>-1</sup>. (C and D) Experimental setup for a synthesis involving dropwise injection of the precursor solution and plot of the instantaneous concentration of precursor as a function of reaction time.  $c_0 = 1$  mM,  $k = 0.5$  s<sup>-1</sup>,  $\tau = 1$  s. Note that the instantaneous concentrations (the vertical axis), and thereby the reaction rates, differ by several orders of magnitude between these two syntheses.

However, one notable drawback associated with one-shot injection is the exponential decay of precursor concentration and thus reaction rate over time (Figure 1.5B), which can pose challenges in certain aspects of synthetic control. For instance, when the system involves two or more metals, this feature is responsible for the spatial variations in composition, which is determined by the relative reduction rates of the respective precursors. When multiple metal precursors are reduced in the same solution, the

composition of each nanocrystal would constantly vary along the radial direction, depending on the ratio between the reduction rates of different precursors [52]. In this case, attempting to tune the reduction rate of any one of them by means of temperature and/or ligand exchange can lead to complex effects on the synthetic outcome, making it essentially impractical to experimentally control the spatial distribution of elements.

Since the variation in reaction rate is deeply rooted in the conversion and consumption of the precursor, a straightforward way to mitigate such variation is to maintain a constant precursor concentration by continually supplementing additional precursor into the system to compensate for consumption. By dividing the precursor solution into small droplets and introducing them into the reaction solution in multiple runs, rather than all at once, a steady level of concentration can be intuitively expected [77]. To simplify the analysis, we can create a model in which the precursor is added as droplets of a consistent size at a specific rate, while disregarding the consequent temperature fluctuations and volume increase in the reaction solution (Figure 1.5C). The reaction of the precursor from each droplet can be treated as an independent event, with its concentration following the same exponential decay as observed in the case of one-shot injection. For instance, the addition of the first droplet causes to a rapid increase in concentration, which then gradually decrease until the second droplet is added. The second droplet induces another sudden increase in precursor concentration, establishing a new starting point for the subsequent exponential decay (Figure 1.5D). Taken together, the concentration fluctuates up and down along with the addition of more droplets, while maintaining an overall upward trend. As the peak concentration continues to rise, the consumption rate of precursor also increases in proportion, eventually leading to an interesting situation in

which the decrease in concentration due to decay during the addition of two consecutive droplets is nearly identical to the increase in precursor concentration resulting from the subsequent droplet addition. This equilibrium leads to the establishment of a steady state. In this steady state, the precursor concentration fluctuates only between two extreme values, defined as the upper limit ( $c_{up}$ ) and lower limit ( $c_{low}$ ), so as the reaction rate.

The steady state achieved through dropwise precursor introduction offers many merits when compared to the inherent concentration variation associated with the one-shot injection method. First, it allows for the maintenance of a significantly lower precursor concentration, which is crucial for preventing self-nucleation during seed-mediated growth. By operating at a slower reaction rate, the growth behavior becomes predominantly controlled by surface diffusion, ensuring accurate replication of the template's morphology. Additionally, the precursor concentration in the steady state can be readily tuned by controlling the injection rate using a syringe pump. Interestingly, the reaction rate in the steady state is independent of the reactivity of the precursor, enabling the simultaneous reduction of precursors to different metals at the same rate. This facilitates the production of alloy nanocrystals with uniform and tunable compositions.

#### **1.4 Scope of This Work**

This work aims to explore several strategies for controlling the size, morphology, and composition of mono-, bi-, and multi-metallic nanocrystals, and to elucidate the mechanisms responsible for the formation of unique nanostructures, alongside an evaluation of their properties towards biomedical and catalytic applications. This dissertation is organized into three components: *i*) controlling the size and morphology of

Au nanoparticles on *a*-Se nanosphere templates to form hybrid nanostructures; *ii*) controlling the morphology of Rh shell on Pd cubic template to form bi-metallic core-shell nanocrystals; and *iii*) controlling the morphology and composition of a quaternary alloy shell on Rh cubic template to generate multi-metallic core-shell nanocrystals.

In Chapter 2, in collaboration with Dr. Haoyan Cheng, I report a comprehensive investigation of the nucleation and growth patterns of Au nanoparticles on the surface of *a*-Se nanospheres. With dropwise injection of Au precursor, its galvanic reaction with elemental Se results in the formation of Au atoms *in situ*. These atoms then undergo heterogeneous nucleation and growth right on the surface of the *a*-Se nanospheres. Without involving additional reducing agents, this process confines the nucleation of Au nanoparticles only on the surface of the *a*-Se nanospheres, with the number and size of the resultant Au particles being determined by the initially formed nuclei. The number of the initially formed Au nuclei on each *a*-Se nanosphere can be gradually increased from 1 to 2, 3, and 10 by increasing the pH value of the reaction mixture and thereby elevating the initial reduction rate. The as-obtained Au nanoparticles can serve as patches for the conjugation of a targeting ligand, such as folic acid-terminated poly(ethylene glycol) disulfide, to enhance the cellular uptake of *a*-Se nanospheres.

In Chapter 3, co-authored with Dr. Ying Lyu, I demonstrate a facile route to regulate the growth of a Rh overlayer on a Pd cubic template, enabling the synthesis of Pd@Rh nanocrystals. The product features smooth, well-defined {100} facets for the preparation of Rh nanocages. With slow dropwise injection of sodium hexachlororhodate(III) ( $\text{Na}_3\text{RhCl}_6$ ), a precursor with lower reactivity than rhodium acetate ( $\text{Rh}(\text{OAc})_3$ ), the reaction can be maintained at a decelerated pace to avoid homogeneous

nucleation. The  $\text{Br}^-$  ions from KBr serve as a bifunctional ligand to further slowdown the reaction *via* ligand exchange and ensure the formation of Rh(100) surface. The reaction is conducted at a high temperature of 210 °C to promote surface diffusion. Benefiting from the conformal coverage of an atomically thin Rh overlayer, the core–shell nanocubes exhibit enhanced thermal stability compared to the Pd mono-metallic counterparts, as evidenced by *in situ* electron microscopy observation. The subsequent chemical wet etching of the core–shell nanocubes leads to the generation of Rh nanocages with well-defined {100} surface and ultrathin walls.

In Chapter 4, I further explore the potential of template-mediated growth combined with dropwise injection of precursor to develop a transformative method for the creation of multi-metallic nanocrystals with controlled elemental compositions and surface structures. Through the use of Rh cubic seeds with excellent thermal stability, halide-free precursors to avoid oxidative etching, and a tight control over the reduction kinetics, I develop a robust protocol for the synthesis of nanocrystals featuring {100} facets and a nearly equimolar RuRhPdPt alloy on the surface. This work demonstrates the feasibility of not only controlling the surface composition of multi-metallic nanocrystals but also manipulating their facet or atomic arrangement on the surface. The as-prepared alloy nanocubes exhibited superior thermal stability in both shape and composition, as well as enhanced catalytic performance toward ethanol oxidation.

## **1.5 Notes to Chapter 1**

Part of this Chapter is adapted from the review articles co-authored by me: “Colloidal Synthesis of Metal Nanocrystals: From Asymmetrical Growth to Symmetry

Breaking” published in *Chemical Reviews* [18], “Galvanic Replacement Synthesis of Metal Nanostructures: Bridging the Gap between Chemical and Electrochemical Approaches” published in *Accounts of Chemical Research* [70], and “Bi-metallic Core–Shell Nanocrystals: Opportunities and Challenges” published in *Nanoscale Horizons* [78].

## 1.6 References

- [1] Rycenga, M.; Cobley, C. M.; Zeng, J.; Li, W.; Moran, C. H.; Zhang, Q.; Qin, D.; Xia, Y. *Chem. Rev.* **2011**, *111*, 3669–3712.
- [2] Kauranen, M.; Zayats, A. V. *Nat. Photon.* **2012**, *6*, 737–748.
- [3] Jones, M. R.; Osberg, K. D.; Macfarlane, R. J.; Langille, M. R.; Mirkin, C. A. *Chem. Rev.* **2011**, *111*, 3736–3827.
- [4] Lal, S.; Link, S.; Halas, N. J. *Nat. Photon.* **2007**, *1*, 641–648.
- [5] Koenderink, A. F.; Alù, A.; Polman, A. *Science* **2015**, *348*, 516–521.
- [6] Quan, L. N.; Kang, J.; Ning, C.-Z.; Yang, P. *Chem. Rev.* **2019**, *119*, 9153–9169.
- [7] Zhu, B.; Gong, S.; Cheng, W. *Chem. Soc. Rev.* **2019**, *48*, 1668–1711.
- [8] Kamyshny, A.; Magdassi, S. *Small* **2014**, *10*, 3515–3535.
- [9] Talapin, D. V.; Lee, J.-S.; Kovalenko, M. V.; Shevchenko, E. V. *Chem. Rev.* **2010**, *110*, 389–458.
- [10] Mayer, K. M.; Hafner, J. H. *Chem. Rev.* **2011**, *111*, 3828–3857.
- [11] Konstantatos, G.; Sargent, E. H. *Nat. Nanotechnol.* **2010**, *5*, 391–400.
- [12] Shi, Y.; Lyu, Z.; Zhao, M.; Chen, R.; Nguyen, Q. N.; Xia, Y. *Chem. Rev.* **2021**, *121*, 649–735.
- [13] Wu, Y.; Wang, D.; Li, Y. *Chem. Soc. Rev.* **2014**, *43*, 2112–2124.

- [14] Zhao, Z.; Chen, C.; Liu, Z.; Huang, J.; Wu, M.; Liu, H.; Li, Y.; Huang, Y. *Adv. Mater.* **2019**, *31*, 1808115.
- [15] Yang, X.; Yang, M.; Pang, B.; Vara, M.; Xia, Y. *Chem. Rev.* **2015**, *115*, 10410–10488.
- [16] Dreaden, E. C.; Alkilany, A. M.; Huang, X.; Murphy, C. J.; El-Sayed, M. A. *Chem. Soc. Rev.* **2012**, *41*, 2740–2779.
- [17] Alivisatos, P. *Nat. Biotechnol.* **2004**, *22*, 47–52.
- [18] Nguyen, Q. N.; Wang, C.; Shang, Y.; Janssen, A.; Xia, Y. *Chem. Rev.* **2023**, *123*, 3693–3760.
- [19] Personick, M. L.; Langille, M. R.; Zhang, J.; Harris, N.; Schatz, G. C.; Mirkin, C. A. *J. Am. Chem. Soc.* **2011**, *133*, 6170–6173.
- [20] Zhou, S.; Zhao, M.; Yang, T.-H.; Xia, Y. *Mater. Today* **2019**, *22*, 108–131.
- [21] Wang, H.; Zhou, S.; Gilroy, K. D.; Cai, Z.; Xia, Y. *Nano Today* **2017**, *15*, 121–144.
- [22] Xiong, Y.; Cai, H.; Wiley, B. J.; Wang, J.; Kim, M. J.; Xia, Y. *J. Am. Chem. Soc.* **2007**, *129*, 3665–3675.
- [23] Gilroy, K. D.; Ruditskiy, A.; Peng, H.-C.; Qin, D.; Xia, Y. *Chem. Rev.* **2016**, *116*, 10414–10472.
- [24] Wang, W.; Chen, Z.; Shi, Y.; Lyu, Z.; Cao, Z.; Cheng, H.; Chi, M.; Xiao K.; Xia, Y. *ChemCatChem* **2020**, *12*, 5156–5163.
- [25] Yang, X.; Liang, Z.; Chen, S.; Ma, M.; Wang, Q.; Tong, X.; Zhang, Q.; Ye, J.; Gu, L.; Yang, N. *Small* **2020**, *16*, 2004727.
- [26] Eom, N.; Messing, M. E.; Johansson, J.; Deppert, K. *ACS Nano* **2021**, *15*, 8883–8895.
- [27] Habas, S. E.; Lee, H.; Radmilovic, V.; Somorjai, G. A.; Yang, P. *Nat. Mater.* **2007**, *6*, 692–697.
- [28] Fan, Z.; Zhang, H. *Acc. Chem. Res.* **2016**, *49*, 2841–2850.
- [29] Yao, Y.; He, D.; Lin, Y.; Feng, X.; Wang, X.; Yin, P.; Hong, X.; Zhou, G.; Wu, Y.; Li, Y. *Angew. Chem. Int. Ed.*, **2016**, *55*, 5501–5505.

- [30] Zhao, M.; Figueroa-Cosme, L.; Elnabawy, A. O.; Vara, M.; Yang, X.; Roling, L. T.; Chi, M.; Mavrikakis, M.; Xia, Y. *Nano Lett.*, **2016**, *16*, 5310–5317.
- [31] Wang, X.; Figueroa-Cosme, L.; Yang, X.; Luo, M.; Liu, J.; Xie, Z.; Xia, Y. *Nano Lett.* **2016**, *16*, 1467–1471.
- [32] Ma, Y.; Li, W.; Cho, E. C.; Li, Z.; Yu, T.; Zeng, J.; Xie, Z.; Xia, Y. *ACS Nano* **2010**, *4*, 6725–6734.
- [33] Stamenkovic, V. R.; Fowler, B.; Mun, B. S.; Wang, G.; Ross, P. N.; Lucas, C. A.; Markovic, N. M. *Science* **2007**, *315*, 493–497.
- [34] Chen, P.-C.; Liu, X.; Hedrick, J. L.; Xie, Z.; Wang, S.; Lin, Q.-Y.; Hersam, M. C.; David, V. P.; Mirkin, C. A. *Science* **2016**, *352*, 1565–1569.
- [35] Yao, Y.; Huang, Z.; Xie, P.; Lacey, S. D.; Jacob, R. J.; Xie, H.; Chen, F.; Nie, A.; Pu, T.; Rehwoldt, M.; Yu, D.; Zachariah, M. R.; Wang, C.; Shahbazian-Yassar, R.; Li, J.; Hu, L. *Science* **2018**, *359*, 1489–1494.
- [36] Xin, Y.; Li, S.; Qian, Y.; Zhu, W.; Yuan, H.; Jiang, P.; Guo, R.; Wang, L. *ACS Catal.* **2020**, *10*, 11280–11306.
- [37] Ben-Shahar, Y. Stone, D.; Banin, U. *Chem. Rev.* **2023**, *123*, 3790–3851.
- [38] Li, J.; Sun, S. *Acc. Chem. Res.* **2019**, *52*, 2015–2025.
- [39] Xie, C.; Niu, Z.; Kim, D.; Li, M.; Yang, P. *Chem. Rev.* **2020**, *120*, 1184–1249.
- [40] An, K.; Somorjai, G. A. *ChemCatChem* **2012**, *4*, 1512–1524.
- [41] Cao, S.; Tao, F. F.; Tang, Y.; Li, Y.; Yu, J. *Chem. Soc. Rev.* **2016**, *45*, 4747–4765.
- [42] Ringe, E.; McMahon, J. M.; Sohn, K.; Cogley, C.; Xia, Y.; Huang, J.; Schatz, G. C.; Marks, L. D.; Van Duyne, R. P. *J. Phys. Chem. C* **2010**, *114*, 12511–12516.
- [43] Yang, H. *Angew. Chem. Int. Ed.* **2011**, *50*, 2674–2676.
- [44] Xia, Y.; Yang, X. *Acc. Chem. Res.* **2017**, *50*, 450–454.
- [45] Chen, Y.; Fan, Z.; Zhang, Z.; Niu, W.; Li, C.; Yang, N.; Chen, B.; Zhang, H. *Chem. Rev.* **2018**, *118*, 6409–6455.

- [46] Liu, X.; Wang, D.; Li, Y. *Nano Today* **2012**, *7*, 448–466.
- [47] Wiley, B. J.; Im, S. H.; Li, Z.-Y.; McLellan, J.; Siekkinen, A.; Xia, Y. *J. Phys. Chem. B* **2006**, *110*, 15666–15675.
- [48] Evanoff Jr., D. D.; Chumanov, G. *ChemPhysChem* **2005**, *6*, 1221–1231.
- [49] Zhang, Q.; Li, W.; Moran, C.; Zeng, J.; Chen, J.; Wen, L.-P.; Xia, Y. *J. Am. Chem. Soc.* **2010**, *132*, 11372–11378.
- [50] Christopher, P.; Linic, S. *J. Am. Chem. Soc.* **2008**, *130*, 11264–11265.
- [51] Christopher, P.; Linic, S. *ChemCatChem* **2010**, *2*, 78–83.
- [52] Zhou, M.; Wang, H.; Vara, M.; Hood, Z. D.; Luo, M.; Yang, T.-H.; Bao, S.; Chi, M.; Xiao, P.; Zhang, Y.; Xia, Y. *J. Am. Chem. Soc.* **2016**, *138*, 12263–12270.
- [53] Moseley, P.; Curtin, W. A. *Nano Lett.* **2015**, *15*, 4089–4095.
- [54] Bligaard, T.; Nørskov, J. K. *Electrochim. Acta* **2007**, *52*, 5512–5516.
- [55] Wang, X.; Choi, S.-I.; Roling, L. T.; Luo, M.; Ma, C.; Zhang, L.; Chi, M.; Liu, J.; Xie, Z.; Herron, J. A.; Mavrikakis, M.; Xia, Y. *Nat. Commun.* **2015**, *6*, 7594.
- [56] Park, J.; Zhang, L.; Choi, S.-I.; Roling, L. T.; Lu, N.; Herron, J. A.; Xie, S.; Wang, J.; Kim, M. J.; Mavrikakis, M. *ACS Nano* **2015**, *9*, 2635–2647.
- [57] Zhang, L.; Roling, L. T.; Wang, X.; Vara, M.; Chi, M.; Liu, J.; Choi, S.-I.; Park, J.; Herron, J. A.; Xie, Z.; Mavrikakis, M.; Xia, Y. *Science* **2015**, *349*, 412–416.
- [58] Wang, X.; Vara, M.; Luo, M.; Huang, H.; Ruditskiy, A.; Park, J.; Bao, S.; Liu, J.; Howe, J.; Chi, M.; Xie, Z.; Xia, Y. *J. Am. Chem. Soc.* **2015**, *137*, 15036–15042.
- [59] Chen, R.; Lyu, Z.; Shi, Y.; Xia, Y. *Chem. Mater.* **2021**, *33*, 3791–3801.
- [60] Zhang, Y.; Zhong, X.; Li, Z.; Xia, Y. *Part. Part. Syst. Charact.* **2014**, *31*, 266273.
- [61] LaMer, V. K.; Dinegar, R. H. *J. Am. Chem. Soc.* **1950**, *72*, 4847–4854.
- [62] Whitehead, C. B.; Ozkar, S.; Finke, R. G. *Chem. Mater.* **2019**, *31*, 7116–7132.

- [63] Xia, Y.; Gilroy, K. D.; Peng, H.-C.; Xia, X. *Angew. Chem. Int. Ed.* **2017**, *56*, 60–95.
- [64] Wang, Y.; Xie, S.; Liu, J. Y.; Park, J.; Huang, C. Z.; Xia, Y. *Nano Lett.* **2013**, *13*, 2276–2281.
- [65] Zhou, S.; Mesina, D. S.; Organt, M. A.; Yang, T.-H.; Yang, X.; Huo, D.; Zhao, M.; Xia, Y. *J. Mater. Chem. C* **2018**, *6*, 1384–1392.
- [66] Walsh, M. J.; Tong, W.; Katz-Boon, H.; Mulvaney, P.; Etheridge, J.; Funston, A. M. *Acc. Chem. Res.* **2017**, *50*, 2925–2935.
- [67] Wiley, B. J.; Wang, Z.; Wei, J.; Yin, Y.; Cobden, D. H.; Xia, Y. *Nano Lett.* **2006**, *6*, 2273–2278.
- [68] Zhou, L.; Qiu, X.; Lyu, Z.; Zhao, M.; Xia, Y. *Chem. Mater.* **2021**, *33*, 5391–5400.
- [69] Langille, M. R.; Zhang, J.; Mirkin, C. A. *Angew. Chem. Int. Ed.* **2011**, *50*, 3543–3547.
- [70] Cheng, H.; Wang, C.; Qin, D.; Xia, Y. *Acc. Chem. Res.* **2023**, *56*, 900–909.
- [71] Chen, J.; McLellan, J. M.; Siekkinen, A.; Xiong, Y.; Li, Z.-Y.; Xia, Y. *J. Am. Chem. Soc.* **2006**, *128*, 14776–14777.
- [72] Mayers, B.; Jiang, X.; Sunderland, D.; Cattle, B.; Xia, Y. *J. Am. Chem. Soc.* **2003**, *125*, 13364–13365.
- [73] Shi, Q.; Zhu, C.; Du, D.; Wang, J.; Xia, H.; Engelhard, M. H.; Feng, S.; Lin, Y. *J. Mater. Chem. A* **2018**, *6*, 8855–8859.
- [74] Yae, S.; Nasu, N.; Matsumoto, K.; Hagihara, T.; Fukumuro, N.; Matsuda, H. *Electrochim. Acta* **2007**, *53*, 35–41.
- [75] Cheng, H.; Cao, Z.; Chen, Z.; Zhao, M.; Xie, M.; Lyu, Z.; Zhu, Z.; Chi, M.; Xia, Y. *Nano Lett.* **2019**, *19*, 4997–5002.
- [76] Kwon, S. G.; Hyeon, T. *Small* **2011**, *7*, 2685–2702.
- [77] Peng, H.-C.; Park, J.; Zhang, L.; Xia, Y. *J. Am. Chem. Soc.* **2015**, *137*, 6643–6652.
- [78] Wang, C.; Shi, Y.; Qin, D.; Xia, Y. *Nanoscale Horiz.* **2023**, DOI: 10.1039/D3NH00098B.

# CHAPTER 2. CONTROLLING THE NUCLEATION AND GROWTH OF GOLD ON AMORPHOUS SELENIUM NANOSPHERES TO ENHANCE THEIR CELLULAR UPTAKE AND CYTOTOXICITY

## 2.1 Introduction

The development of nanomedicine and related applications calls for the optimization of cellular uptake of nanoparticles by tailoring the interaction between the cell membrane and nanoparticles [1–3]. For synthetic nanoparticles, this can be achieved by functionalizing their surface with a ligand to specifically target the receptor expressed on the cell membrane. To this end, it is often necessary to tightly control both the coverage density and spatial distribution of the ligand on the surface of nanoparticles in order to optimize their cellular uptake and cytotoxicity [4]. Despite some progress in manipulating the coverage density of ligands, it remains a challenge to experimentally tailor the surface distribution of the ligand in a controllable fashion.

Nanospheres made of amorphous selenium (*a*-Se) have recently received increasing interest as a new platform material for nanomedicine owing to their biological activity and pharmacological actions [5–7]. Upon internalization, they can kill cancer cells by generating reactive oxygen species (ROS) and thereby inducing mitochondria-mediated apoptosis in a dosage-dependent manner [8]. Their relatively inert surface, however, calls for modification with a noble metal, followed by conjugation with a bioactive ligand. To this end, the strong reducing power of elemental Se has been leveraged for the *in situ*

deposition of noble-metal nanoparticles on its surface through a galvanic replacement mechanism [9, 10], and *a*-Se nanospheres could also serve as templates for the fabrication of hollow particles made of Pt and other inorganic materials [11–13]. In such a synthesis, metal atoms are generated *in situ* on the surface of each *a*-Se nanosphere, followed by their heterogeneous nucleation and growth into a polycrystalline shell with a controllable thickness [14]. Significantly, the strong reducing power and the amorphous structure of *a*-Se nanospheres offer a simple and versatile system to control the nucleation and growth of noble-metal nanoparticles without involving the interferences from faceting and surface capping agents. In principle, if the as-deposited noble metal is gold, it would offer a robust handle to further conjugate thiol-terminated compounds through the Au–S covalent bonding [15]. Nevertheless, how to control the number of Au patches and thus the distribution of the ligand on the surface of an *a*-Se nanosphere remain to be demonstrated.

Herein, I investigate the nucleation and growth of Au nanoparticles from the surface of *a*-Se nanospheres. The galvanic reaction between ionic Au precursor and elemental Se results in the formation of Au atoms *in situ*, followed by their heterogeneous nucleation and growth right on the surface of the *a*-Se nanospheres. Different from other systems involving additional reducing agents, Au atoms can only be generated on the surface of the *a*-Se nanospheres during the nucleation stage. As a result, the initial nucleation on the surface of the *a*-Se nanosphere plays a pivotal role in determining the number and size of the resultant Au nanoparticles. The number of the initially formed Au nuclei on each *a*-Se nanosphere can be gradually increased from 1 to 2, 3, and 10 by increasing the pH value of the reaction mixture and thereby increasing the initial reduction rate. The as-formed Au nanoparticles can serve as patches for the conjugation of a targeting ligand such as folic

acid-terminated poly(ethylene glycol) disulfide. This work allows one to control the nucleation and growth pattern of Au nanoparticles and thus the distribution of targeting ligand on the surface of  $\alpha$ -Se nanospheres to enhance their uptake by cells.

## 2.2 Results and Discussion

**Controlling the Nucleation and Growth of Au on the Surface of  $\alpha$ -Se Nanospheres.** When an aqueous suspension of  $\text{HAuCl}_4$  is dropwise injected into an aqueous suspension containing  $\alpha$ -Se nanospheres, galvanic replacement will be initiated immediately between the Au precursor and Se atoms due to their significant difference in reduction potential. In the initial step of the reaction, Se atoms will be oxidized and dissolved into the reaction mixture (Figure 2.1A). At the same time, the electrons generated in the oxidation process will be captured by Au precursor to generate Au atoms *via* a reduction reaction. In this synthesis, the  $\alpha$ -Se nanospheres serve the dual roles as a reducing agent and a substrate for the heterogeneous nucleation of Au atoms formed *in situ*. Since the surface of  $\alpha$ -Se nanospheres is amorphous in structure, the Au atoms tend to nucleate and grow by themselves, contributing to the persistence of an island growth mode. In addition, the Au atoms should be confined to the original site of formation due to the large lattice mismatch between crystalline Au and  $\alpha$ -Se, as well as the strong binding between Au and Se. This is very different from the case involving the galvanic replacement reaction between Ag nanocubes and Au ions [16, 17]. Because Au and Ag solids share the same face-centered cubic (*fcc*) structure, together with closely matched lattice constants (4.0786 Å and 4.0862 Å for Au and Ag, respectively), the Au atoms are able to epitaxially nucleate from and diffuse across the entire surface of the Ag template. In the following step, the Se atoms will be continuously oxidized to release electrons, which can be easily transported

to the Au surface. The Au ions tend to be reduced to Au atoms on the newly formed Au surface because Au is a good electron conductor, and the energy barrier should be lower than that on the Se surface [18]. By separating oxidation and reduction to different sites on the surface, one can mitigate the transport issue of chemical reagents involved [19]. The overall reaction underlying this galvanic replacement process between Se atoms and Au ions can be summarized as follows:



Since the reaction involved the use of hydroxide ions ( $\text{OH}^-$ ), I was able to control the reduction rate of the Au precursor by preadjusting the pH value of the reaction solution, thereby controlling the initial number of Au nuclei and thus the average number of Au nanoparticles on each *a*-Se nanosphere. The formation of different number of Au nanoparticles on the surface of each *a*-Se nanosphere can be attributed to the nucleation of Au on one/multiple sites when the reduction kinetics is changed by pH variation (Figure 2.1B). As a unique feature of this system, the morphology of the final product is determined by the number of nucleation sites formed in the initial stage of a synthesis, which, in turn, can be readily controlled by adjusting the experimental parameters that affect the initial reduction rate. In a sense, the formed Au atoms only contribute to the size enlargement of the Au nanoparticles.

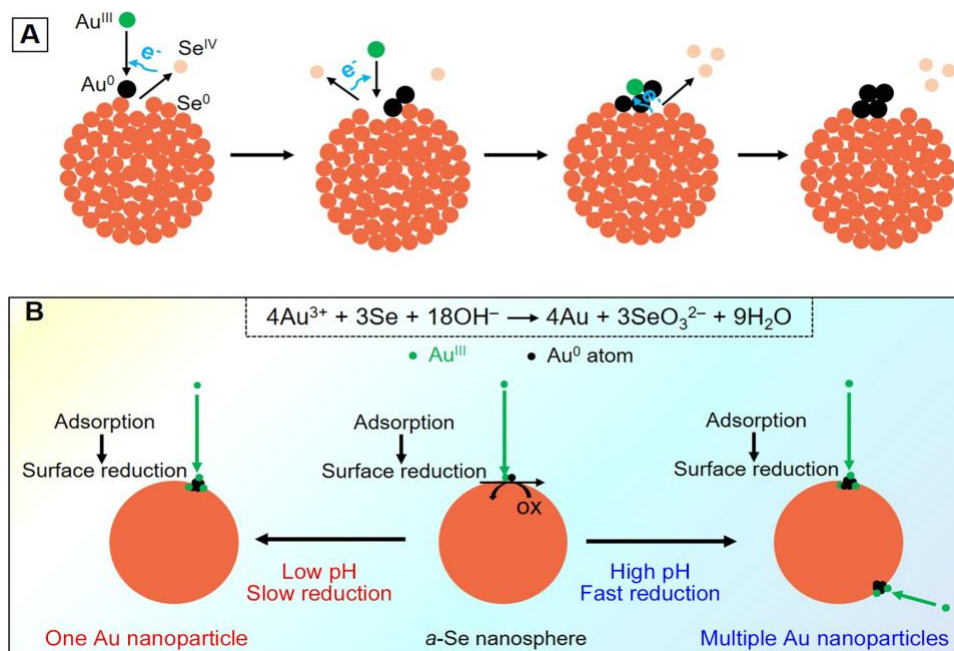


**Figure 2.1.** (A) Schematic illustration of the different stages involved in the reduction of a Au precursor to Au atom on the surface of an  $\alpha$ -Se nanosphere through a galvanic replacement reaction, as well as the nucleation and growth of Au nanoparticles. (B) Depending on the pH value of the reaction mixture, the initial reduction rate can be readily controlled to generate different numbers of Au nanoparticles on the surface of each  $\alpha$ -Se nanosphere.

I confirmed this proposed mechanism by sampling the particles formed at different stages of a standard synthesis for transmission electron microscopy (TEM) analysis. Indeed, on each  $\alpha$ -Se nanosphere, the size of the Au nanoparticle increased with prolonging the reaction time while no additional nucleation site was observed during the growth process. After the introduction of  $HAuCl_4$  for 25 min, there was a tiny Au nanoparticle with an average diameter of 1.3 nm on each  $\alpha$ -Se nanosphere (Figure 2.2A), indicating slow nucleation and growth in the first 25 min. As the reaction proceeded to 1 h, the Au nanoparticles grew to an average diameter of  $10.4 \pm 2.1$  nm (Figure 2.2B). When the reaction time was further prolonged to 2 h, the average diameter of the Au nanoparticles increased to  $14.3 \pm 3.4$  nm (Figure 2.2C). During the growth process, no additional nucleation site was

observed and the average number of Au nanoparticles per *a*-Se nanosphere was essentially kept at one. To further support my argument, I also analyzed the particles obtained by injecting different volumes of Au precursor solution into the reaction mixture. The average sizes of the Au nanoparticles increased from  $5.5\pm 1.3$  to  $9.7\pm 2.4$  and  $18.8\pm 3.5$  nm when the volume of the precursor solution was increased from 0.125 to 0.25 and 1.0 mL (Figure 2.2D–F). Despite the change in size, the number of Au nanoparticles on each *a*-Se nanosphere remained the same (one Au nanoparticle per *a*-Se nanosphere) regardless of the amount of the precursor solution added.

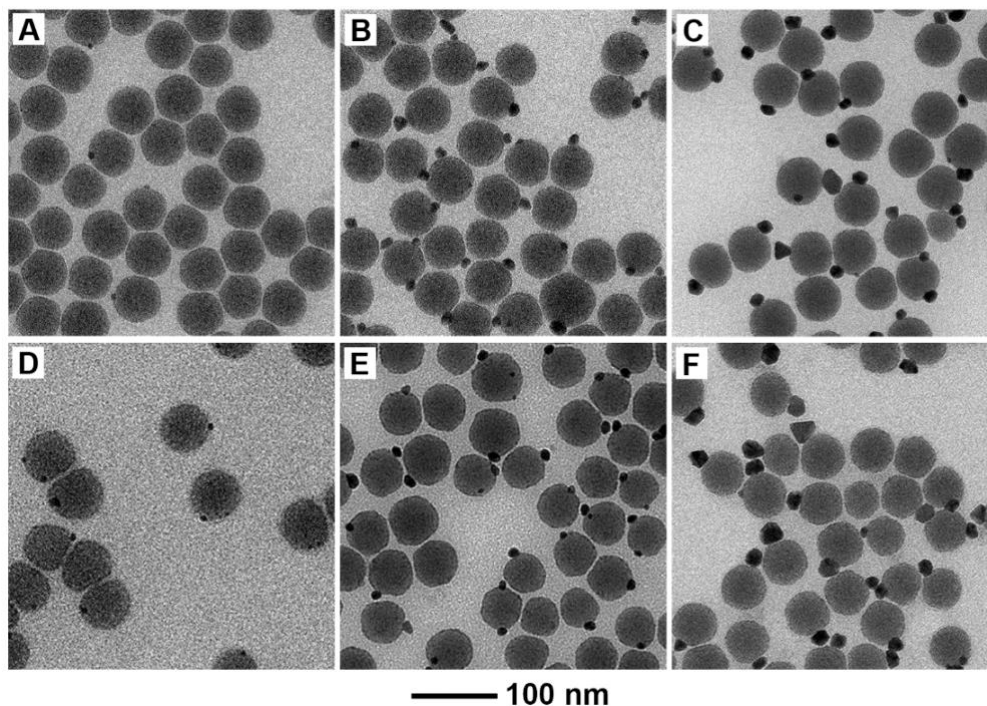


**Figure 2.2.** (A–C) TEM images of Se–Au dimers obtained at different time points into a standard synthesis: (A) 25 min, (B) 1 h, and (C) 2 h. (D–F) TEM images of Se–Au dimers obtained at room temperature by injecting (D) 0.125, (E) 0.25, and (F) 1.0 mL of 0.4 mM HAuCl<sub>4</sub> solution into an aqueous mixture containing *a*-Se nanospheres and cetyltrimethylammonium bromide. The initial pH of the reaction solution was set to 8.2 while all other conditions were kept the same as the standard synthesis.

To elucidate the composition, phase, and structure of the hybrid nanoparticles, I analyzed freshly prepared Se–Au<sub>1</sub> dimers (similar to the one shown in Figure 2.2C) by X-ray diffraction (XRD), X-ray photoelectron spectroscopy (XPS), and advanced electron microscopy. The results are summarized in Figure 2.3. For the XRD data, the peaks at  $2\theta$  of 38.1°, 44.4°, 64.6°, 77.5°, and 81.7° can be assigned to the diffraction from (111), (200), (220), (311), and (222) planes of *fcc* Au (Figure 2.3A). The XPS spectrum further confirmed that the Au in the hybrid nanoparticles was dominated by Au<sup>0</sup> in the zerovalent state (Figure 2.3B). The high-resolution transmission electron microscopy (HRTEM) and high-angle annular dark-field scanning transmission electron microscopy (HAADF-STEM) images indicated that the as-formed Au nanoparticle was polycrystalline (Figure 2.3C,D). The lattice spacing of 0.236 nm can be indexed to the (111) plane of *fcc* Au. The polycrystalline structure can be attributed to the slow reduction kinetics of the Au precursor. The prior work of my group indicated that a fast reduction rate tended to favor the formation of single-crystal Au nanoparticles while a slow reduction rate can lead to the formation of twinned products [20]. Altogether, the results from these multidimensional characterizations demonstrated that the nanoparticles formed on the surface of the *a*-Se nanospheres were made of Au rather than other Au-containing compounds such as AuSe. This conclusion is reasonable because all the syntheses of AuSe reported in the literature [21] were conducted in much harsher conditions (*e.g.*, elevated temperatures) than what was involved in the current synthesis. However, I cannot exclude the existence of a small portion of AuSe at the Au–Se interface between polycrystalline Au nanoparticle and amorphous *a*-Se nanosphere. At the current stage of technological development, it is

challenging to characterize this nonflat interface. Nevertheless, the exposed surface on the as-formed Au nanoparticles should be made of Au rather than AuSe.

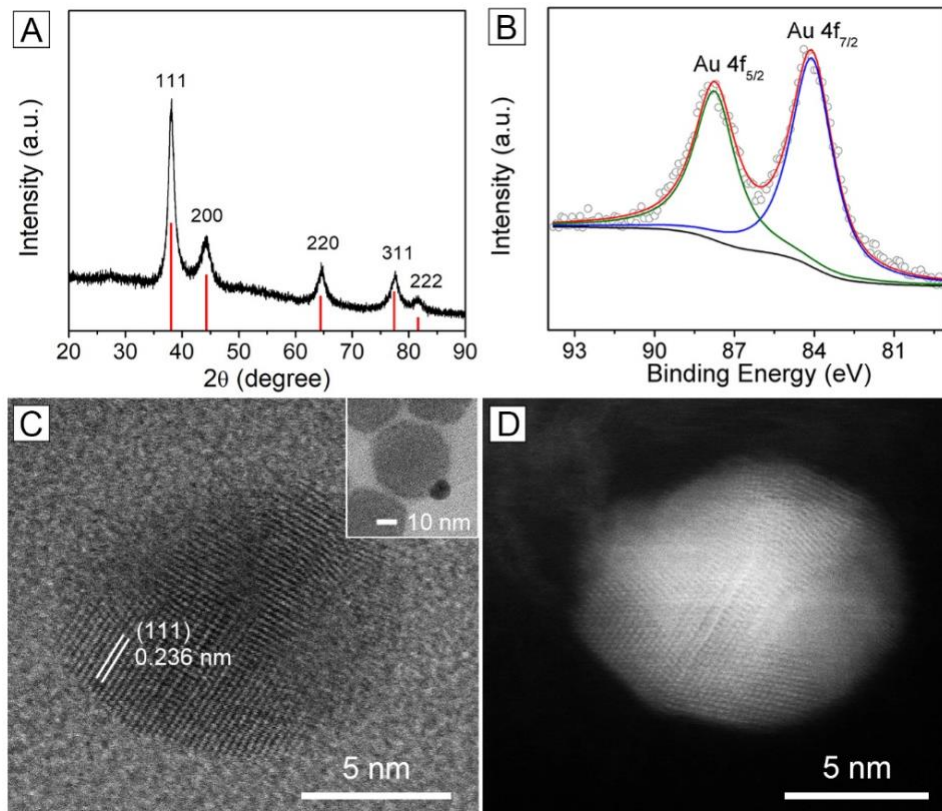


**Figure 2.3.** (A) XRD pattern recorded from a freshly prepared Se–Au<sub>1</sub> sample. The red bars indicate the diffraction peaks of *fcc* Au (PDF# 04-0874). (B) XPS spectrum recorded from the same batch of sample, indicating the dominance of zerovalent Au. (C) HRTEM and (D) HAADF-STEM images of a Au nanoparticle on one Se–Au<sub>1</sub> particle. The lattice spacing of 0.236 nm can be assigned to the (111) plane of *fcc* Au. Both the HRTEM and HAADF-STEM images suggest a polycrystalline structure for the Au nanoparticle. Inset in panel C: a TEM image of the whole Se–Au<sub>1</sub> particle.

The influence of the initial pH on the morphology of the particles can be seen in Figure 2.4. When the initial pH was set to 6.0 prior to the introduction of HAuCl<sub>4</sub>, Au only nucleated and grew on *ca.* 35% of the *a*-Se nanospheres to generate Se–Au hybrid nanoparticles with a Janus structure (Figure 2.4A). The percent of Se–Au Janus nanoparticles increased to 82% when the initial pH was increased to 8.2 (Figure 2.4B). If

the initial pH was further increased, more than one Au nanoparticles would start to form on the surface of each *a*-Se nanosphere. On average, 2, 3, and 10 Au nanoparticles would be formed on the surface of each *a*-Se nanosphere when the initial pH was adjusted to 9.0, 10.0, and 11.0, respectively (Figure 2.4C–E). It should be pointed out that, due to the strong contrast between Se and Au under TEM imaging, essentially all the Au nanoparticles on each *a*-Se nanosphere could be easily resolved even though they overlapped along the direction of electron beam. At a higher pH of 11.7, Au nanoparticles were able to nucleate and grow from numerous sites on the surface of each *a*-Se nanosphere, resulting in the formation of Se–Au hybrid structure with a relatively rough surface (Figure 2.4F).

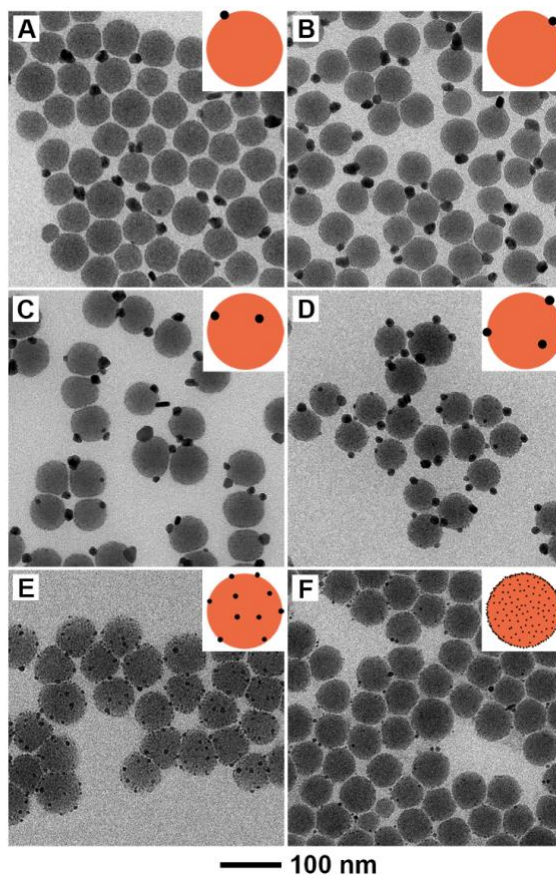


**Figure 2.4.** TEM images of Se–Au hybrid nanoparticles obtained at different initial pH values of (A) 6.0, (B) 8.2, (C) 9.0, (D) 10.0, (E) 11.0, and (F) 11.7, respectively. Insets: the corresponding two-dimensional models.

As more nucleation sites were involved at a higher initial pH, the size of the resultant Au nanoparticles decreased (Figure 2.5). Specifically, the average diameter of the Au nanoparticles decreased from  $18.1 \pm 2.9$  nm to  $17.8 \pm 2.2$ ,  $15.6 \pm 2.1$ ,  $11.7 \pm 2.0$ , and  $7.2 \pm 1.8$  nm, respectively, when the initial pH was set to 6.0, 8.2, 9.0, 10.0, and 11.0. According to the heterogeneous nucleation and growth theory, the growth mode of a second material on the surface of a substrate was mainly determined by the surface energies, supersaturation, atomic bonding, and lattice mismatch [22–24]. Generally speaking, island growth is expected to dominate over conformal deposition if the lattices of the two materials are heavily mismatched [25]. When the substrate was made of an amorphous material, the lattice of the Au nanoparticles could not match with that of the substrate at all, leading to island growth of Au on the surface of *a*-Se nanospheres. A similar phenomenon was also observed in the synthesis of SiO<sub>2</sub>@Au core–shell nanoparticles, where the SiO<sub>2</sub> surface also had an amorphous structure [26].

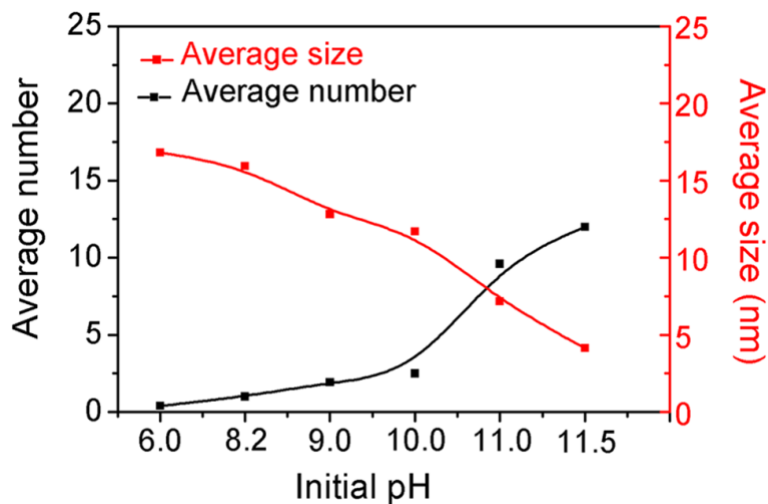


**Figure 2.5.** The average diameters and numbers of Au nanoparticles on each *a*-Se nanosphere at different initial pH values.

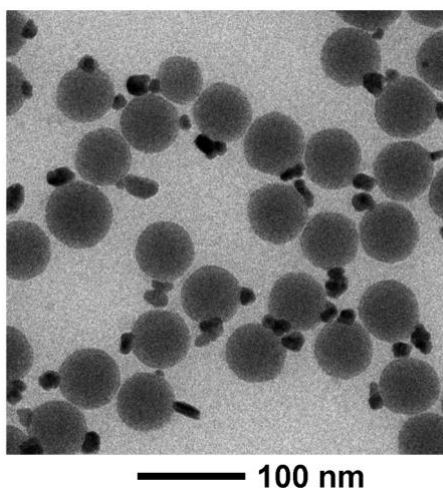


**Figure 2.6.** TEM image of the Se–Au hybrid nanoparticles prepared using the standard protocol except for the introduction of Au precursor in one shot. Compared with the sample shown in Figure 2.4B (*i.e.*, involving dropwise addition), the Au nanoparticles were more broadly distributed in terms of size and shape.

It is worth emphasizing that the dropwise injection of Au precursor allowed me to attain the same initial experimental parameters (*e.g.*, pH value and precursor concentration) at the early stage of each synthesis, leading to essentially identical nucleation on the surface of the *a*-Se nanospheres for all the experimental groups. Even though the pH value of the reaction system might change with reaction time or the introduction of more  $\text{HAuCl}_4$ , the number of Au nanoparticles on each *a*-Se nanosphere would not change because the number of nucleation sites had been fixed at the very beginning of the synthesis. When the introduction of the Au precursor was switched from dropwise titration to one shot injection while keeping all other experimental parameters the same as the standard protocol, the much higher initial concentration of the Au precursor resulted in the formation of Au nanoparticles with broader distributions in size and shape (Figure 2.6). It is worth noting that the initial pH value would quickly drop from 8.2 to 6.5 if the acidic  $\text{HAuCl}_4$  precursor was introduced in one shot. The increase in Au precursor concentration and the decrease

in pH value tended to have opposite effects on the reaction kinetics, which could influence the initial number of Au nuclei formed on the surface of each *a*-Se nanosphere. Our result indicate that more than one Au nanoparticles could be formed on some of the *a*-Se nanospheres.

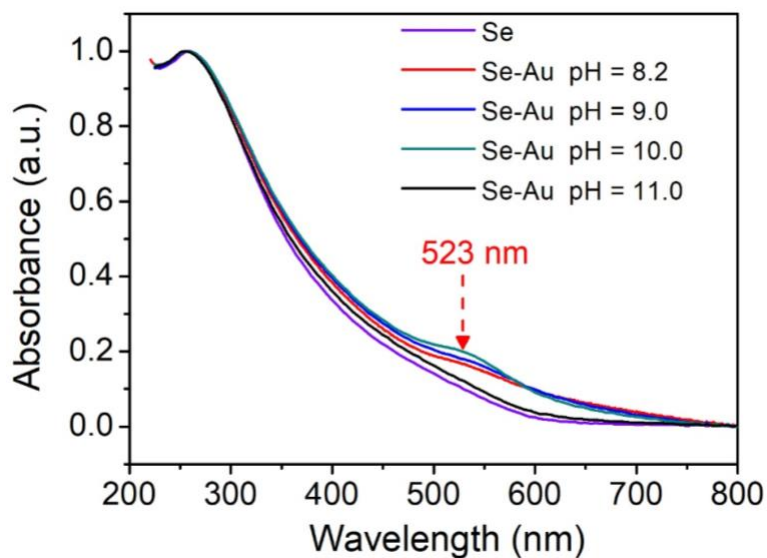


**Figure 2.7.** UV-vis spectra recorded from aqueous suspensions of the *a*-Se nanospheres, and the Se-Au hybrid nanoparticles obtained at different initial pH values, as shown in Figure 2.4B-E.

Ultraviolet-visible (UV-vis) spectroscopy was used to monitor the optical properties of the *a*-Se nanospheres before and after the deposition of Au nanoparticles at different initial pH (Figure 2.7). The absorption peak of pristine *a*-Se nanospheres was located at 259 nm. After reacting with the Au precursor, a new peak appeared at 523 nm, indicating the formation of Au nanoparticles. The intensity of this new peak gradually increased when the initial pH was increased from 8.2 to 10.0. However, the intensity of this peak suddenly dropped to the baseline when the initial pH was further increased to 11.0. This change was consistent with the dramatic reduction in size for the Au

nanoparticles. For all these samples, no obvious alteration was observed for the peak associated with the  $\alpha$ -Se nanospheres because of their negligible change in size before and after the galvanic reaction.

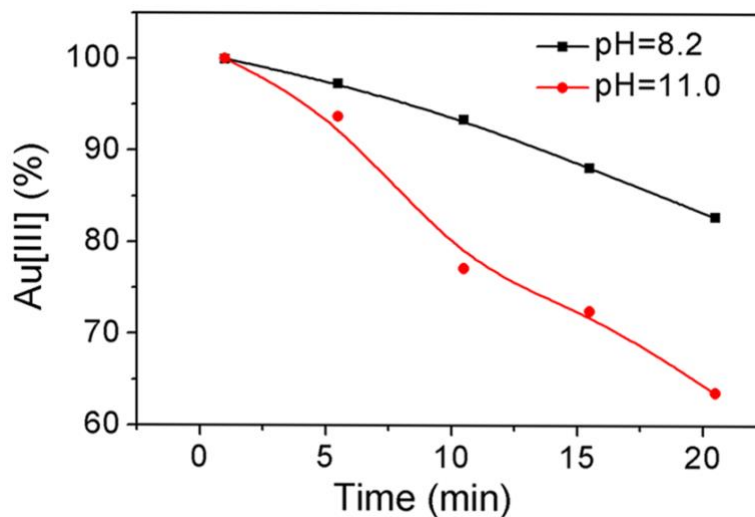


**Figure 2.8.** Plots showing the concentration of Au precursor remaining in the reaction solution as a function of reaction time at initial pH of 8.2 and 11.0.

**Mechanistic Investigation of the Synthesis.** To elucidate the mechanistic details, I tracked the reduction of the Au precursor under different initial pH by injecting the precursor in one shot, quenching the reaction with concentrated HCl, and then measuring the concentration of the Au precursor remaining in the reaction mixture using inductively-coupled plasma mass spectrometry (ICP-MS) (Figure 2.8). The results indicated that, in the first 10 min of a synthesis, the concentration of Au precursor decreased by a much greater percent at an initial pH of 11.0 relative to the case with an initial pH of 8.2. In other words, the reduction of Au precursor in the initial stage of a synthesis was greatly accelerated at a higher concentration of  $\text{OH}^-$ . In the synthesis,  $\alpha$ -Se nanospheres served as both the reducing agent and substrate by directly donating electrons to the Au precursor at

the solid-liquid interface. Therefore, at a higher pH, more Au atoms would be generated on the surface of each  $\alpha$ -Se nanosphere, providing a stronger driving force to create more nucleation sites. It is worth emphasizing that when a large amount of the Au precursor was added in one shot, as in the case of ICP-MS measurement, the pH would be greatly lowered due to the acidity of the precursor. As a result, the difference in reduction rate shown in Figure 2.8 should be an underestimate of the actual difference between two initial pH values in the case of standard protocol involving dropwise injection of the precursor.

**Formation of Se@Au Core-Shell nanospheres.** In addition to lattice mismatch, the bond energy between the substrate and the deposited metal also plays an important role in determining the formation of a core-shell structure. Since the bond energy of Au-Se ( $251.0 \pm 14.6 \text{ kJ} \cdot \text{mol}^{-1}$ ) is slightly stronger than that of Au-Au ( $226.2 \pm 0.5 \text{ kJ} \cdot \text{mol}^{-1}$ ) [27], it is feasible to generate Se@Au core-shell structure. If the reduction rate was fast enough to allow numerous Au nuclei to form on the surface of an  $\alpha$ -Se nanosphere, it should be able to obtain Se@Au core-shell nanospheres despite the large lattice mismatch between Au and  $\alpha$ -Se.

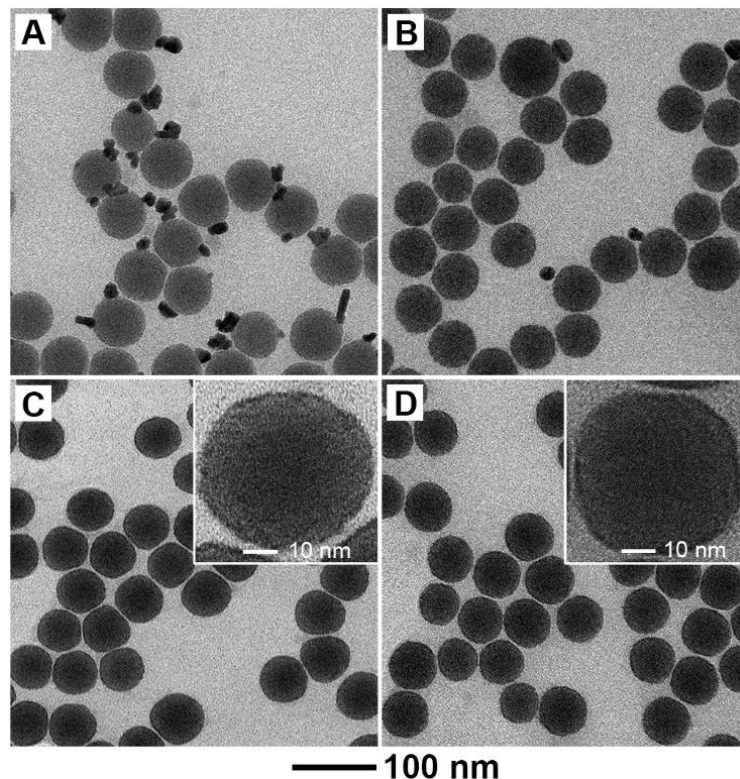


**Figure 2.9.** TEM images of the Se–Au hybrid nanoparticles obtained by adding (in one shot) 1.0 mL of 0.4 mM HAuCl<sub>4</sub> solution at different temperatures and then waiting for 4 h: (A) 25, (B) 40, and (C) 60 °C, respectively. (D) TEM image of the Se–Au hybrid nanoparticles prepared by introducing (in one shot) 2 mL of 0.4 mM HAuCl<sub>4</sub> at 60 °C.

To this end, we investigated the role of reaction temperature, another experimental parameter that can significantly affect the reaction kinetics. The dropwise addition of precursor was also replaced by one shot injection to quickly increase the concentration of Au. Figure 2.9 shows TEM images of the products obtained at different reaction temperatures, with the initial pH being kept the same. At 25 °C, most of the products were dimeric particles, with the Au nanoparticles taking an irregular morphology (Figure 2.9A). In contrast, when the temperature was increased to 40 °C, a mixture of Se–Au dimeric particles and Se@Au core–shell nanospheres were obtained due to the acceleration in reduction rate (Figure 2.9B). At 60 °C, the reduction of Au on the surface of *a*-Se nanospheres was further accelerated, resulting in a boosted nucleation event and

simultaneous formation of numerous Au nuclei on the surface of each *a*-Se nanosphere. In this case, Se@Au core-shell nanospheres with a relatively smooth surface were obtained (Figure 2.9C,D). The possible mechanism involved in the formation of Se@Au core-shell particles is illustrated in Figure 2.10A. The Au shell could be clearly distinguished from the *a*-Se core under TEM when viewed at a high magnification (Figure 2.10B). Due to the high vacuum environment of TEM and high energy of electron beam, the *a*-Se was quickly evaporated during electron irradiation to leave Au hollow nanospheres with a relatively uniform size (Figure 2.10C) under TEM when the microscope was operated at 110 kV.

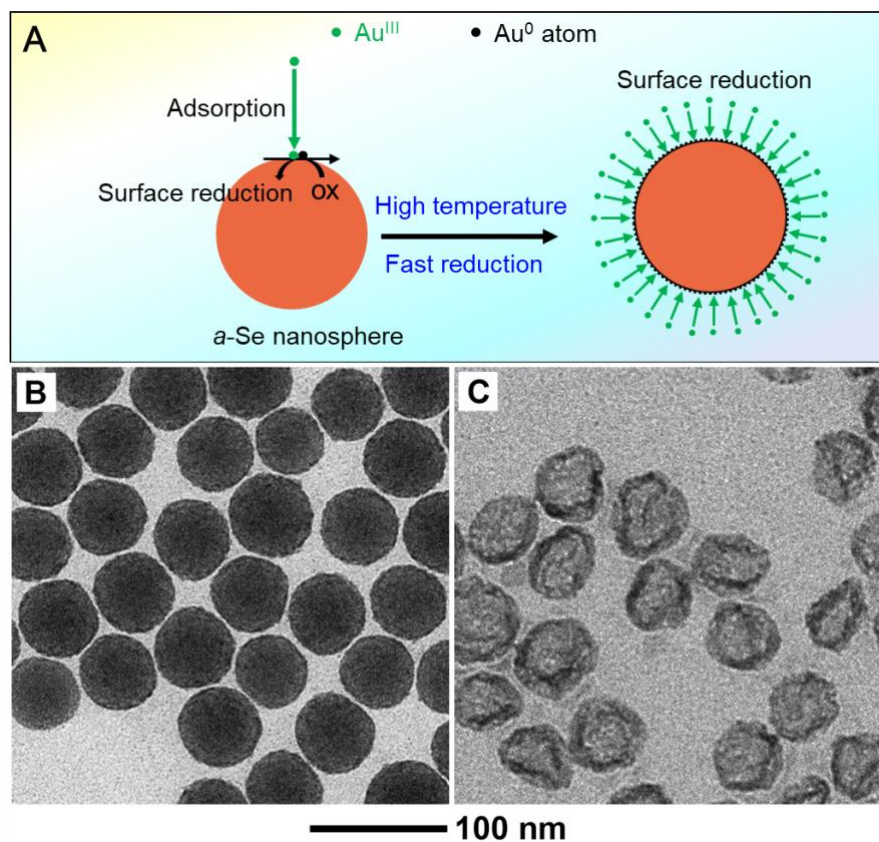


**Figure 2.10.** (A) Schematic illustration of the mechanism involved in the formation of Se@Au core-shell nanoparticles. Due to the fast initial reduction kinetics, a large number of Au nuclei are simultaneously formed on the surface of the *a*-Se nanosphere, resulting in the formation of a core-shell structure. (B) TEM image of the Se@Au core-shell nanoparticles obtained by injecting 2 mL of 0.4 mM H<sub>2</sub>AuCl<sub>4</sub> solution into the reaction

solution in one shot. The initial pH value of the reaction solution was set to 8.2 and the reaction temperature was held at 60 °C for 4 h. (C) TEM image of Au hollow nanoparticles obtained after the Se in the core had been removed by evaporation as a result of e-beam irradiation for 1 min in the TEM.

**Replacement of CTAB with PVP and KBr.** As one of the most commonly used cationic surfactants for the aqueous synthesis of Au nanoparticles, the Br<sup>-</sup> ions from CTAB can coordinate with Au through ligand exchange between Cl<sup>-</sup> and Br<sup>-</sup>. This ligand exchange process can slow down the reduction of Au and help control the synthesis of Au-Se hybrid nanoparticles with different structures. However, CTAB is also known for its cytotoxicity [28] although it can be replaced by a disulfide- or thiol-based compound due to the stronger Au-S covalent bonding. To address this potential issue, we attempted to replace CTAB with non-toxic reagents for the synthesis (Figure 2.11). When 0.5 mL of CTAB (100 mM) was replaced with 0.5 mL of KBr (100 mM) containing 5.5 mg of PVP, Se-Au hybrid nanoparticles with a dimeric structure was obtained at an initial pH of 8.6. When the initial pH was increased to 9.3 and 10.0, the average number of Au nanoparticles per *a*-Se nanosphere also increased. This trend is similar to what was observed when CTAB was used for the synthesis. Compared to the sample shown in Figure 2.4D (*i.e.*, involving the use of CTAB as a surfactant and at the same initial pH of 10.0), more Au nanoparticles per *a*-Se nanosphere were observed in the case of KBr plus PVP. This difference might originate from the additional reducing power of PVP in enhancing the reduction kinetics [29].

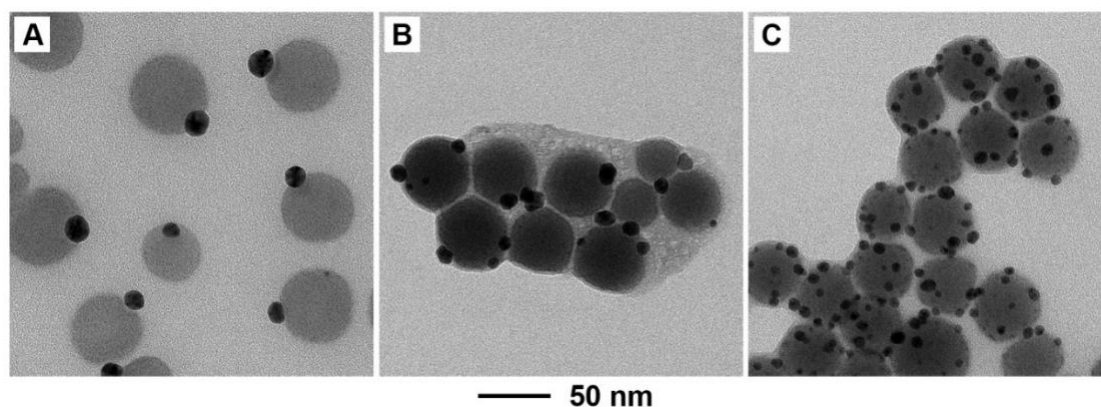


**Figure 2.11.** TEM image of the Se–Au hybrid nanoparticles prepared using the standard protocol except that CTAB was replaced with equal molar amount of KBr and 5.5 mg of PVP. The initial pH value was adjusted to (A) 8.6, (B) 9.3 and (C) 10.0, respectively. The average numbers of Au nanoparticles per *a*-Se nanosphere were about 1, 2, and 7, respectively.

**Dependence of Cellular Uptake on Ligand Distribution.** My collaborators utilized these Se–Au hybrid nanoparticles with enriched surface properties as a model system to study the influence of ligand distribution on cellular uptake and cytotoxicity. As a major advantage, the Au nanoparticles on each *a*-Se nanosphere could serve as patches to conjugate various targeting ligands through the Au–S linkage. For the Se@Au core–shell structure, their cytotoxicity was expected to be compromised because the biologically active *a*-Se was completely covered by Au shell with good biocompatibility. As such, my collaborators chose to focus on Se–Au hybrid nanoparticles with 1, 3 and 10 Au nanoparticles as a model system. After conjugation with OPSS-PEG-FA, the samples were denoted Se–Au<sub>1</sub>–Ligand, Se–Au<sub>3</sub>–Ligand, Se–Au<sub>10</sub>–Ligand, respectively. Based on the FT-IR spectra (Figure 2.12), the CTAB adsorbed on the surface of Au nanoparticles during their synthesis were replaced by the disulfide-based OPSS-PEG-FA due to the stronger Au–S covalent bonding.

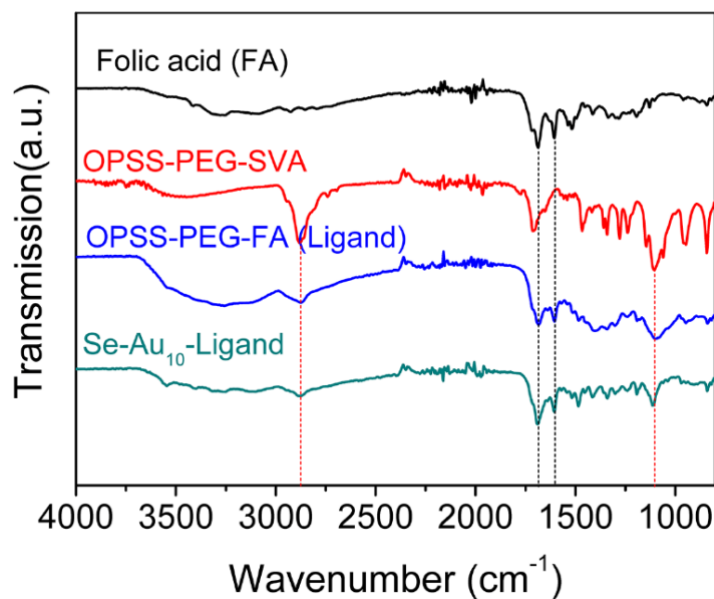


**Figure 2.12.** FT-IR spectra of folic acid, OPSS-PEG-SVA, OPSS-PEG-FA, and Se-Au<sub>10</sub>-Ligand. The characteristic peaks at 1687 and 1606 cm<sup>-1</sup> in the spectrum of FA correspond to N-H bending vibration and C=O stretching of the -CONH group, respectively [30]. For OPSS-PEG-SVA, the peaks at 2881 cm<sup>-1</sup> can be assigned to the aliphatic C-H stretching vibration [31], whereas the peak at 1105 cm<sup>-1</sup> is associated with C-O stretching vibration [32]; both of which are characteristic of PEG. The Se-Au<sub>10</sub>-Ligand showed both characteristic peaks of FA and PEG chains, indicating that folic acid-terminated poly(ethylene glycol) thiol (OPSS-PEG-FA) was successfully conjugated to the surface of Se-Au<sub>10</sub> hybrid nanoparticles.

My collaborators then cultured Hela cells with the Se-Au hybrid nanoparticles with and without conjugation of the OPSS-PEG-FA ligand. The number of the Se-Au hybrid nanoparticles internalized per cell was measured after removal of the surface-bound particles using the I<sub>2</sub>/KI etchant [33]. The etching solution with tolerable cytotoxicity can selectively dissolve the Se-Au nanoparticles on the cell surface within a short period of time, leaving behind those inside the cells untouched. Thus, my collaborators were able to derive the number of nanoparticles internalized by the cells, as well as those attached to the outer surface of the cell membrane. As shown in Figure 2.13A,B, the Se-Au hybrid nanoparticles with more Au nanoparticles on the surface gave a much higher endocytosis

efficiency, which was further increased by ligand modification. This trend indicates that a larger number of Au nanoparticles on the surface of the *a*-Se nanospheres, and thus an increased number of ligands, could greatly enhance the ligand–receptor affinity [34]. Typically, delivery of nanoparticles into a cell involves their binding to the cell surface, followed by internalization *via* receptor-mediated endocytosis. The different efficiencies in cellular uptake might result from their differences in terms of receptor availability, ligand–receptor interaction, and the equilibrium condition between the ligand distribution and cell perception.

My collaborators also evaluated the therapeutic effect of the Se–Au hybrid nanoparticles, with and without ligand modification, by analyzing cell viability (Figure 2.13C). A strong positive correlation was observed between the number of Au nanoparticles on the surface and the cytotoxicity of these hybrid nanoparticles. Upon modification with the ligand, the Se–Au hybrid nanoparticles showed more significant inhibitory effect toward cell viability. My collaborators then evaluated the therapeutic effect of a series of Se–Au hybrid nanoparticles with different ligand distributions by observing morphological changes to F-actin of Hela cells through fluorescence microscopy (Figure 2.14). For the control group with no nanoparticles added (Figure 2.14A), the F-actin was well-organized and highly elongated. No significant change in morphology was observed for the cells cultured with the Se nanospheres and Se–Au<sub>1</sub> nanoparticles (Figure 2.14B,C), as their F-actin was still well-spread. When incubated with Se–Au<sub>3</sub> and Se–Au<sub>10</sub> nanoparticles (Figure 2.14D,E), the F-actin gradually became retracted and condensed. More pronounced collapse of the cell structure was observed when the cells were cultured with Se–Au<sub>1</sub>–Ligand, Se–Au<sub>3</sub>–Ligand, and Se–Au<sub>10</sub>–Ligand nanoparticles, respectively

(Figure 2.14F–H). The improved therapeutic effect might have resulted from the enhanced cellular uptake of Se–Au hybrid nanoparticles, and thereby enhanced cytotoxicity from elemental Se. Previous studies reported that *α*-Se nanoparticles exhibited a similar toxicity to selenite against a number of cancer cell lines, albeit the metabolism mechanism is yet to be elucidated [35].

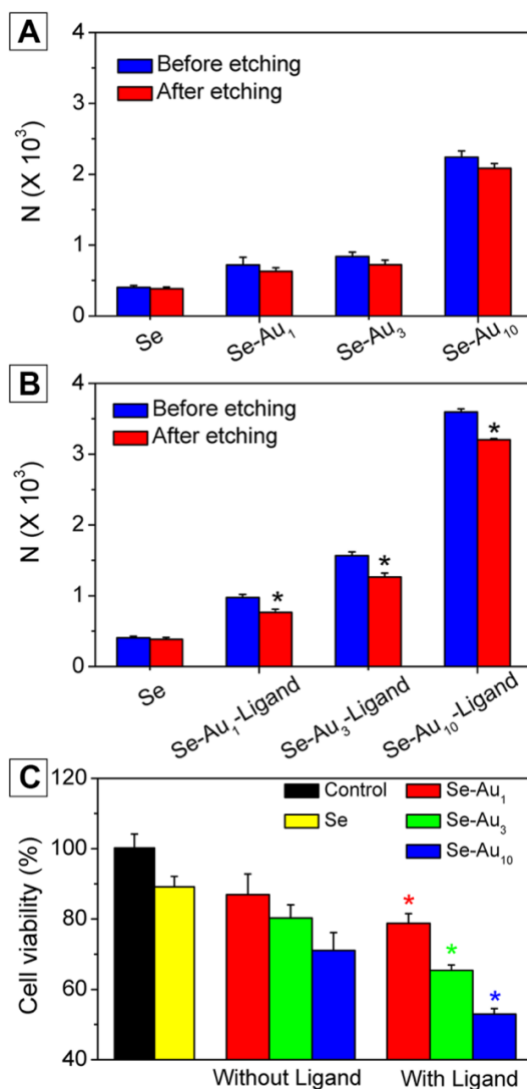


**Figure 2.13.** (A, B) The number of Se–Au hybrid nanoparticles internalized per HeLa cell in the cases of (A) without and (B) with surface ligand, respectively. The surface-bound nanoparticles were removed by etching with I<sub>2</sub>/KI etchant. \*p<0.05 when compared with I<sub>2</sub>/KI etchant. \*p<0.05 when compared with the group before etching. (C) Comparison of

the cell viability measured using MTT. \* $p < 0.05$  when compared with the group without ligand.

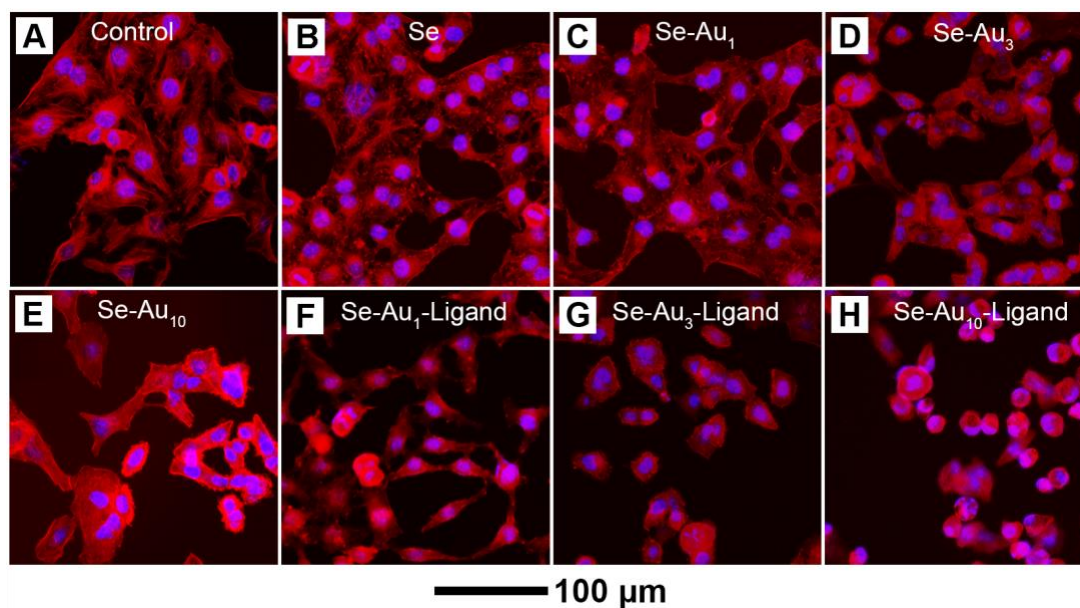


**Figure 2.14.** Fluorescence micrographs of HeLa cells that were cultured for 24 h with (A) no nanoparticles (control group), (B) Se, (C) Se-Au<sub>1</sub>, (D) Se-Au<sub>3</sub>, (E) Se-Au<sub>10</sub>, (F) Se-Au<sub>1</sub>-Ligand, (G) Se-Au<sub>3</sub>-Ligand, and (H) Se-Au<sub>10</sub>-Ligand, respectively, followed by staining of F-actin with Phalloidin-Alexa Fluor-555 (red) and nucleus with DAPI (blue).

It has been established that Se-based nanoparticles could induce cell apoptosis through mitochondrial dysfunction [36]. Loss of the mitochondrial membrane potential due to changes in permeability represents a step key to the induction of cell death [37]. In this study, the mitochondrial membrane potential was measured using fluorescence imaging, with JC-1 serving as a probe [38]. For HeLa cells in the control group, the majority of the mitochondria clustered around the nucleus, simultaneously presenting the bright red and green fluorescence (Figure 2.15A). In contrast, the HeLa cells treated with Se-Au<sub>1</sub>-Ligand, Se-Au<sub>3</sub>-Ligand, and Se-Au<sub>10</sub>-Ligand exhibited differences in loss of mitochondrial membrane potential as revealed by the decreased ratio of red to green fluorescence (Figure 2.15B-D), indicating gradually more dysfunctional mitochondria.

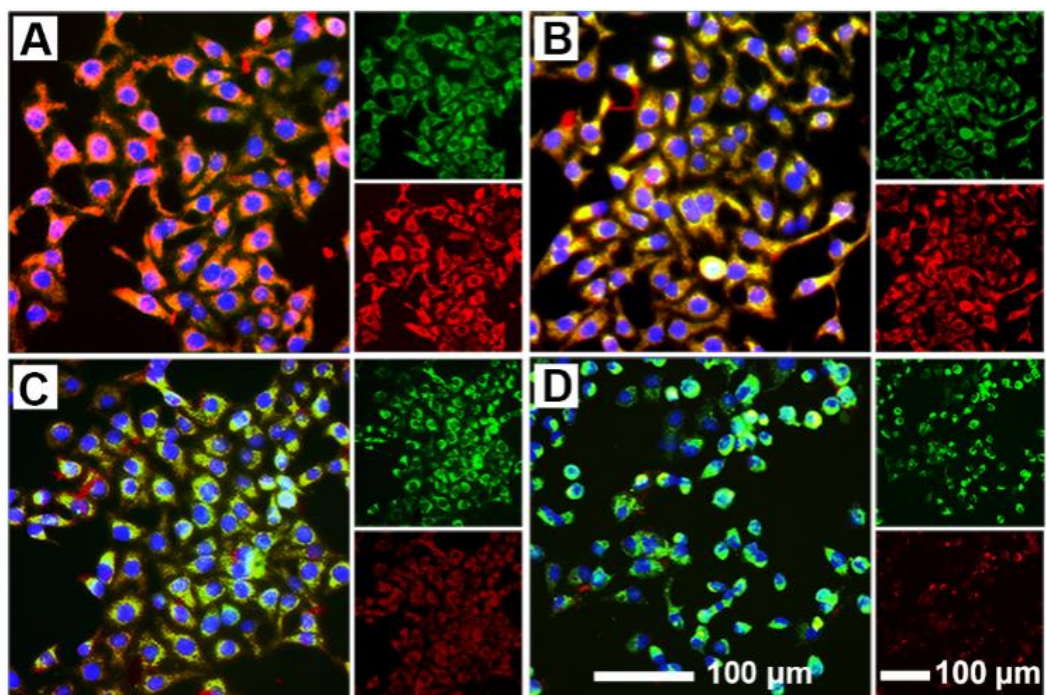


**Figure 2.15.** Fluorescence micrographs of the JC-1-stained HeLa cells that were cultured (A) without nanoparticles, and with (B) Se–Au<sub>1</sub>–Ligand, (C) Se–Au<sub>3</sub>–Ligand, and (D) Se–Au<sub>10</sub>–Ligand for 24 h, respectively.

### 2.3 Conclusion

I have investigated the role of initial reduction rate in controlling the heterogeneous nucleation and growth of Au on *a*-Se nanospheres. By controlling the experimental parameters, especially the initial pH value, the average number of Au nanoparticles formed on each *a*-Se nanosphere could be increased from 1 to 2, 3, 10, and more than 10. The different patterns of nucleation led to the formation of colloidal particles with diverse and controllable morphologies, enabling a systematic analysis of the cellular uptake of nanoparticles with different ligand distributions. Owing to their biological activity and pharmacological actions, the Se–Au hybrid nanoparticles can serve as a class of therapeutic agents for cancer nanomedicine. Our results suggest that Se–Au hybrid nanoparticles with a larger number and a more uniform distribution of ligands on the surface would be

internalized by cells at a greater efficiency, leading to decrease in cell viability and eventual cell death. Further investigation indicated that the dysfunction of mitochondria, as caused by the internalized nanoparticles, was mainly responsible for the cell death. This work not only enriched our understanding of the kinetically controlled nucleation process involving a metal precursor and an amorphous surface, but also shed light on the design and rational synthesis of hybrid nanomaterials for biomedical applications.

## 2.4 Experimental Section

**Chemicals.** Selenious acid ( $\text{H}_2\text{SeO}_3$ , >99.99%), hydrazine monohydrate ( $\text{N}_2\text{H}_4 \cdot \text{H}_2\text{O}$ , >98%), poly(vinylpyrrolidone) (PVP, molecular weight  $\approx 55\ 000$ ), gold(III) chloride trihydrate ( $\text{HAuCl}_4 \cdot 3\text{H}_2\text{O}$ ,  $\geq 99.9\%$ ), cetyltrimethylammonium bromide (CTAB,  $\geq 99.0\%$ ), aqueous solution of hydrochloric acid (HCl, 37%), sodium hydroxide (NaOH, >99.9%), ethylene diamine ( $\text{C}_2\text{H}_8\text{N}_2$ , 99.5%), folic acid (FA, >98%), dimethyl sulfoxide (DMSO, >99.8%), potassium iodide (KI,  $\geq 99.0\%$ ), iodine ( $\text{I}_2$ ,  $\geq 99.8\%$ ), and glutaraldehyde (50 wt % in  $\text{H}_2\text{O}$ ) were all obtained from Sigma-Aldrich and used as received. Orthopyridyl disulfide-PEG-succinimidyl valerate (OPSS-PEG-SVA, molecular weight  $\approx 50\ 000$ ) were ordered from Laysan Bio. Dulbecco's Modified Eagle Medium (DMEM), fetal bovine serum (FBS), penicillin/streptomycin, phosphate buffered saline (PBS, 10 mM, pH = 7.4), and 3-(4,5-dimethyl-2-thiazolyl)-2,5-diphenyl-2-H-tetrazolium bromide (MTT) were purchased from ThermoFisher Scientific.

**Synthesis of  $\alpha$ -Se Nanospheres.** In this work,  $\alpha$ -Se nanospheres served as a substrate to control the nucleation and growth of Au. They were synthesized by sequentially adding 100 mg of PVP and 387 mg of  $\text{H}_2\text{SeO}_3$  into 100 mL of deionized (DI)

water and magnetically stirred at room temperature for 10 min.<sup>5</sup> Then, 1.16 mL of  $\text{N}_2\text{H}_4 \cdot \text{H}_2\text{O}$  was introduced under magnetic stirring. After reaction at room temperature for another 3 h, the solid products were collected by centrifugation at a speed of 12 000 rpm for 20 min and washed three times with DI water. The final products were dispersed in 50 mL of DI water for further use.

**Synthesis of Se–Au Hybrid Nanoparticles.** In a standard protocol, 0.5 mL of CTAB (100 mM) and 0.15 mL of the as-prepared *a*-Se nanospheres were added into 4.5 mL of DI water. The mixture was stirred at room temperature for 10 min and the pH value of the mixture was adjusted to 8.2 by adding NaOH solution. Then, 0.5 mL of aqueous  $\text{HAuCl}_4$  solution (0.4 mM) was added dropwise at a rate of  $0.02 \text{ mL min}^{-1}$  into the mixture under magnetic stirring at room temperature (21 °C) over a period of 4 h. The solid products were collected by centrifugation at 12 000 rpm for 5 min and washed three times with DI water.

**Synthesis of Se–Au Hybrid Nanoparticles with Different Numbers of Au Nanoparticles on Each *a*-Se Nanosphere.** The procedure was the same as the standard protocol for the Se–Au hybrid nanoparticles except that the initial pH of the reaction solution was adjusted to different values. When the initial pH was set to 9.0, 10.0, 11.0, and 11.7, the average numbers of Au nanoparticles per *a*-Se nanosphere were 2, 3, 10, and greater than 10, respectively.

**Synthesis of Se@Au Core–Shell Nanoparticles.** In a typical synthesis, 0.15 mL of the suspension of *a*-Se nanospheres and 0.5 mL of CTAB (100 mM) were added into 4.5 mL of DI water and the as-obtained mixture was stirred at 60 °C for 10 min. Then, a

specific amount of the aqueous H<sub>2</sub>AuCl<sub>4</sub> solution (0.4 mM) was quickly added in one shot. The mixture was stirred at 60 °C for 4 h. The solid products were collected by centrifugation at 12 000 rpm for 5 min and washed twice with DI water, followed by redispersion in DI water.

**Analysis of the Reduction Rates for the Formation of Se–Au Hybrid Nanoparticles under Two Different Initial pH Values.** I compared the reduction rates at two different initial pH values by analyzing the concentrations of Au precursor remaining in the reaction solution at different time points using inductively coupled plasma mass spectrometry (ICP-MS). In a typical procedure, after 0.5 mL of CTAB (100 mM) had been added into 4.5 mL of water, the pH value of the mixture was adjusted to 8.2 or 11.0. Then, 0.15 mL of *a*-Se nanospheres and 0.5 mL of H<sub>2</sub>AuCl<sub>4</sub> (0.4 mM) were sequentially introduced in one shot. At different time points after the introduction of H<sub>2</sub>AuCl<sub>4</sub>, 0.5 mL of aliquot was sampled from the reaction mixture using a glass pipet and immediately injected into 1 mL of 37 wt % HCl to quickly quench the reaction. The sample was then centrifuged for 5 min to precipitate out all the nanoparticles, leaving behind Au precursor in the supernatant for collection, dilution, and ICP-MS analysis.

**Conjugation of Ligand to the Surface of Au Nanoparticles.** In a typical process, FA (200 mg), OPSS-PEG-SVA (20 mg), and 10 µL of ethylenediamine were dissolved in 10 mL of DMSO and stirred in the dark for 36 h to generate folic acid-terminated poly(ethylene glycol) disulfide conjugate (OPSS-PEG-FA). The mixture was then purified by dialysis (2 000 Da) for 3 days in DI water to remove free FA, DMSO, and ethylenediamine. Finally, the sample was dried under a vacuum to obtain OPSS-PEG-FA.

To single out the impact of ligand distribution on cellular uptake, I varied the average number of Au nanoparticles per *a*-Se nanosphere while keeping the size of the Au nanoparticles essentially the same. This was achieved by raising the initial pH to increase the number of Au nanoparticles per *a*-Se nanosphere while increasing the volume of HAuCl<sub>4</sub> accordingly to enlarge the size of the resultant Au nanoparticles. Specifically, a set of Se–Au hybrid nanoparticles was synthesized by following the standard protocol except that 0.25, 0.75, and 2.5 mL of HAuCl<sub>4</sub> (0.4 mM) were introduced into the reaction solution, with the initial pH adjusted to 8.2, 10.0, and 11.0, respectively. The average numbers of Au nanoparticles per *a*-Se nanosphere were about 1, 3, and 10, so the as-obtained Se–Au hybrid nanoparticles were denoted Se–Au<sub>1</sub>, Se–Au<sub>3</sub>, and Se–Au<sub>10</sub>, respectively. For the conjugation of OPSS-PEG-FA to the Au surface, the Se–Au<sub>1</sub>, Se–Au<sub>3</sub>, and Se–Au<sub>10</sub> (Se: 2 μmol) were washed and centrifuged twice with DI water, followed by dispersion in 100, 300, and 1 000 μL, respectively, of aqueous OPSS-PEG-FA solution (4.8 mg mL<sup>-1</sup>). The mixture was stirred in the dark for 24 h and then centrifuged at 12 000 rpm for 5 min to remove the free OPSS-PEG-FA. The supernatant was discarded, and the retrieved solid was washed three times with DI water and then redispersed in 1 mL of DI water. According to the average numbers of Au nanoparticles per *a*-Se nanosphere, the final products were denoted Se–Au<sub>1</sub>–Ligand, Se–Au<sub>3</sub>–Ligand, and Se–Au<sub>10</sub>–Ligand, respectively.

**Cell Culture.** Human cervical carcinoma cell line (Hela) was obtained from American Type Culture Collection (ATCC) and cultured in DMEM supplemented with 10% FBS and 1% penicillin/streptomycin. The cells were maintained in an incubator at 37 °C under a humidified atmosphere of 5% CO<sub>2</sub>.

**Cellular Uptake.** I quantified the number of Se–Au hybrid nanoparticles internalized per cell by removing the surface-bound particles with an etchant [33]. First, I prepared the etching solution by adding I<sub>2</sub> and KI into PBS at a molar ratio of 1:20. The concentration of I<sub>2</sub> was set to 0.34 mM. The HeLa cells were seeded in a 6-well plate and cultured at 37 °C for one day. The cells were then incubated with 1 mL of the culture medium containing *a*-Se, Se–Au<sub>1</sub>, Se–Au<sub>3</sub>, Se–Au<sub>10</sub>, Se–Au<sub>1</sub>–Ligand, Se–Au<sub>3</sub>–Ligand, or Se–Au<sub>10</sub>–Ligand (the concentration of *a*-Se was fixed at 5 μM) at 37 °C for 8 h. After the cells had been washed twice with 1 mL of fresh medium to remove the nonspecifically bound nanoparticles, the number of cells in each well was counted using hemocytometer. Then, the culture medium was replaced with 1 mL of the I<sub>2</sub>/KI etching solution to remove the surface-bound nanoparticles. After incubation at room temperature for 4 min, the cells were repeatedly frozen and thawed five times to disrupt the cell membrane. Finally, the cell debris was dissolved with aqua regia. The concentration of Se was analyzed using ICP-MS. The cellular uptake of the Se–Au hybrid nanoparticles was derived from the concentration of Se, the diameter of *a*-Se nanospheres, and the number of cells.

**Cell Viability.** After HeLa cells had been seeded in 96-well plate and cultured overnight, 150 μL of *a*-Se, Se–Au<sub>1</sub>, Se–Au<sub>3</sub>, Se–Au<sub>10</sub>, Se–Au<sub>1</sub>–Ligand, Se–Au<sub>3</sub>–Ligand, or Se–Au<sub>10</sub>–Ligand (the concentration of Se was set to 5 μM) was added into the well, followed by incubation at 37 °C for 24 h. The culture medium was then replaced with 200 μL of 10% MTT (v/v) in a serum-free medium, followed by incubation at 37 °C for 4 h. Following that, the medium was replaced with DMSO (150 μL per well). After shaking for 10 min in the dark, the optical absorbance of each well at 490 nm was measured using a microplate reader (TECAN Infinite 200).

**Analysis of Cell Morphology.** The morphology of the cells was analyzed by fluorescence microscopy. HeLa cells were seeded in 24-well plate and cultured overnight. The Se, Se–Au<sub>1</sub>, Se–Au<sub>3</sub>, Se–Au<sub>10</sub>, Se–Au<sub>1</sub>–Ligand, Se–Au<sub>3</sub>–Ligand, or Se–Au<sub>10</sub>–Ligand samples was added to achieve the Se concentration of 5  $\mu$ M in the culture medium and incubated with the cells (1 mL per well) at 37 °C for 24 h. Afterward, the cells were washed twice with PBS, followed by fixation with 3% glutaraldehyde (vol/vol) in PBS (pH=7.4) at room temperature for 10 min. Finally, the cells were permeabilized with 0.2% Triton X-100 (v/v) for 20 min. The F-actin and nucleus were labeled with Phalloidin-Alexa Fluor 555 for 20 min and DAPI for 10 min, respectively. The morphology of the cell was analyzed by imaging with a fluorescence microscope.

**Analysis of Mitochondrial Membrane Potential.** The mitochondrial membrane potential was analyzed through JC-1 staining. Generally, JC-1 can exist as aggregates (red fluorescence) or monomers (green fluorescence), corresponding to the preservation and loss of mitochondrial membrane potential, respectively [39]. The HeLa cells were seeded in a 24-well plate and cultured at 37 °C overnight, followed by the introduction of the suspension of Se–Au<sub>1</sub>–Ligand, Se–Au<sub>3</sub>–Ligand, or Se–Au<sub>10</sub>–Ligand sample to achieve the Se concentration of 5  $\mu$ M in the culture medium and incubation for 24 h. The cells were then stained with JC-1 and DAPI (for nucleus) for 15 min. Finally, the sample was washed repeatedly with serum-free medium and analyzed using a fluorescence microscope.

**Characterizations.** The sample for transmission electron microscopy (TEM) was dispersed in DI water, followed by deposition on a carbon-coated copper grid. All images were captured using a Hitachi HT7700 microscope (Japan) operated at 110 kV. High-resolution transmission electron microscopy (HRTEM) and high-angle annular dark-field

scanning transmission electron microscopy (HAADF-STEM) analyses were performed using a Hitachi HD2700 aberration-corrected STEM operated at 200 kV. The instantaneous concentrations of Au precursor were determined by inductively coupled plasma mass spectrometry (ICP-MS) (NexION 300Q, PerkinElmer). The pH was measured using a Five Easy pH Meter (Mettler Toledo, Columbus, OH). The ultraviolet–visible (UV–vis) spectra were collected using a Cary 60 spectrometer (Agilent Technologies, Santa Clara, CA). Size distributions of the particles were determined using a Zetasizer Nano ZS (Malvern Instruments, Worcestershire, UK). The FT-IR spectra were recorded on a Varian 640 IR spectrometer (Agilent Technologies, Santa Clara, CA). The as-prepared sample was also characterized by powder X-ray diffraction (XRD) on a Si zero-background holder using a Rigaku MiniFlex 600 diffractometer with a Cu K $\alpha$  X-ray source ( $\lambda = 1.5406 \text{ \AA}$ ) in the range of 20–90° (2 $\theta$ ). X-ray photoelectron spectroscopy (XPS) measurement was performed using a Thermo K-alpha spectrometer with an Al K $\alpha$  X-ray source (Thermo Scientific, Waltham, MA). The fluorescence micrographs of cells were acquired using a Leica DMI 6000B fluorescence microscope (Leica Microsystems, Buffalo Grove, IL).

## 2.5 Notes to Chapter 2

Part of this Chapter is adapted from the article “Controlling the Nucleation and Growth of Au on *a*-Se Nanospheres to Enhance Their Cellular Uptake and Cytotoxicity” published in *Journal of the American Chemical Society* [40].

## 2.6 References

- [1] Donahue, N. D.; Acar, H.; Wilhelm, S. *Adv. Drug Delivery Rev.* **2019**, *143*, 68–96.
- [2] Cho, E. C.; Zhang, Q.; Xia, Y. *Nat. Nanotechnol.* **2011**, *6*, 385–391.

- [3] Salatin, S.; Khosroushahi, A. Y. *J. Cell. Mol. Med.* **2017**, *21*, 1668–1686.
- [4] Chubertová, V.; Martinez-Veracoechea, F. J.; Vacha, R. *Soft Matter* **2015**, *11*, 2726–2730.
- [5] Cheng, H.; Zhou, S.; Xie, M.; Gilroy, K. D.; Zhu, Z.; Xia, Y. *ChemNanoMat* **2021**, *7*, 620–625.
- [6] Huang, Y.; He, L.; Liu, W.; Fan, C.; Zheng, W.; Wong, Y.-S.; Chen, T. *Biomaterials* **2013**, *34*, 7106–7116.
- [7] Liu, W.; Li, X.; Wong, Y.-S.; Zheng, W.; Zhang, Y.; Cao, W.; Chen, T. *ACS Nano* **2012**, *6*, 6578–6591.
- [8] Chen, T.; Wong, Y.-S.; Zheng, W.; Bai, Y.; Huang, L. *Colloids Surf. B.* **2008**, *67*, 26–31.
- [9] Chang, T.-W.; Wang, C.-W.; Chen, C.-H.; Li, Y.-C.; Hsu, C.-L.; Chang, H.-T.; Lin, Z.-H. *Nano Energy* **2016**, *22*, 564–571.
- [10] Cheng, H.; Cao, Z.; Chen, Z.; Zhao, M.; Xie, M.; Lyu, Z.; Zhu, Z.; Chi, M.; Xia, Y. *Nano Lett.* **2019**, *19*, 4997–5002.
- [11] Mayers, B.; Jiang, X.; Sunderland, D.; Cattle, B.; Xia, Y. *J. Am. Chem. Soc.* **2003**, *125*, 13364–13365.
- [12] Qiu, J.; Camargo, P. H. C.; Jeong, U.; Xia, Y. *Acc. Chem. Res.* **2019**, *52*, 3475–3487.
- [13] Camargo, P. H. C.; Lee, Y. H.; Jeong, U.; Zou, Z.; Xia, Y. *Langmuir* **2007**, *23*, 2985–2992.
- [14] Jeong, U.; Herricks, T.; Shahar, E.; Xia, Y. *J. Am. Chem. Soc.* **2005**, *127*, 1098–1099.
- [15] Xia, X.; Yang, M.; Wang, Y.; Zheng, Y.; Li, Q.; Chen, J.; Xia, Y. *ACS Nano* **2012**, *6*, 512–522.
- [16] Sun, Y.; Xia, Y. *J. Am. Chem. Soc.* **2004**, *126*, 3892–3901.
- [17] Au, L.; Lu, X.; Xia, Y. *Adv. Mater.* **2008**, *20*, 2517–2522.
- [18] Grzelczak, M.; Liz-Marzán, L. M. *Chem. Soc. Rev.* **2014**, *43*, 2089–2097.

- [19] Kim, Y.; Jung, S.-M.; Kim, K.-S.; Kim, H.-Y.; Kwon, J.; Lee, J.; Cho H.-S. Kim, Y.-T. *J. Am. Chem. Soc.* **2022**, *2*, 2491–2500.
- [20] Zheng, Y.; Ma, Y.; Zeng, J.; Zhong, X.; Jin, M.; Li, Z.-Y.; Xia, Y. *Chem. Asian J.* **2013**, *8*, 792–799.
- [21] Feng, D.; Taskinen, P. *J. Chem. Thermodynamics* **2014**, *71*, 98–102.
- [22] Fan, F.-R.; Liu, D.-Y.; Wu, Y.-F.; Duan, S.; Xie, Z.-X.; Jiang, Z.-Y.; Tian, Z.-Q. *J. Am. Chem. Soc.* **2008**, *130*, 6949–6951.
- [23] Liu, J.; Zhang, J. *Chem. Rev.* **2020**, *120*, 2123–2170.
- [24] Zhao, M.; Xia, Y. *Nat. Rev. Mater.* **2020**, *5*, 440–459.
- [25] Xia, Y.; Gilroy, K. D.; Peng, H.-C.; Xia, X. *Angew. Chem., Int. Ed.* **2017**, *56*, 60–95.
- [26] Li, C.-L.; Chen, J.-K.; Fan, S.-K.; Ko, F.-H.; Chang, F.-C. *ACS Appl. Mater. Inter.* **2012**, *4*, 5650–5661.
- [27] Luo, Y.-R. *Comprehensive Handbook of Chemical Bond Energies*. CRC Press: Boca Raton, **2007**: pp 65–66.
- [28] Alkilany, A. M.; Nagaria, P. K.; Hexel, C. R.; Shaw, T. J.; Murphy, C. J.; Wyatt, M. D. *Small* **2009**, *5*, 701–708.
- [29] Xiong, Y.; Washio, I.; Chen, J.; Cai, H.; Li, Z.-Y.; Xia, Y. *Langmuir* **2006**, *22*, 8563–8570.
- [30] Das, R.P.; Chakravarti, S.; Patel, S.S.; Lakhamje, P.; Gurjar, M.; Gota, V.; Singh, B.G.; Kunwar, A. *Int. J. Pharmaceut.* **2020**, *586*, 119522.
- [31] Wang, W.; Yang X.; Fang, Y.; Ding, J. *Appl. Energy* **2009**, *86*, 170–174.
- [32] Ebadi, M.; Bullo, S.; Buskara, K.; Hussein, M. Z.; Fakurazi, S.; Pastorin G. *Sci. Rep.* **2020**, *10*, 21521.
- [33] Cho, E. C.; Xie, J.; Wurm, P. A.; Xia, Y. *Nano Lett.* **2009**, *9*, 1080–1084.
- [34] Peterson, J. L.; Ceresa, B. P. *Cells* **2021**, *10*, 2409.
- [35] Weekley, C. M.; Harris, H. H. *Chem. Soc. Rev.* **2013**, *42*, 8870–8894.

- [36] Liao, W.; Yu, Z.; Lin, Z.; Lei, Z.; Ning, Z.; Regenstein, J. M.; Yang, J.; Ren, J. *Sci. Rep.* **2015**, *5*, 1–13.
- [37] Cheng, H.; Huo, D.; Zhu, C.; Shen, S.; Wang, W.; Li, H.; Zhu, Z.; Xia, Y. *Biomaterials* **2018**, *178*, 517–526.
- [38] Sharma, S.; Chockalingam, S.; Sanpui, P.; Chattopadhyay, A.; Ghosh, S. S. *Silver Adv. Healthcare Mater.* **2014**, *3*, 106–114.
- [39] Chen, Q.; Huo, D.; Cheng, H.; Lyu, Z.; Zhu, C.; Guan, B.; Xia, Y. *Adv. Healthcare Mater.* **2019**, *8*, 1801113.
- [40] Cheng, H.; Wang, C.; Lyu, Z.; Zhu, Z.; Xia, Y. *J. Am. Chem. Soc.* **2023**, *145*, 1216–1226.

# **CHAPTER 3. SYNTHESIS OF PALLADIUM@RHODIUM NANOCUBES WITH WELL-DEFINED {100} SURFACE AND CONTROLLED SHELL THICKNESSES**

## **3.1 Introduction**

Nanocrystals based on Rh have received great interests as heterogeneous catalysts with superior performance in a wide variety of reactions, including CO oxidation [1], NO reduction[2], and hydrogenations [3]. They have found commercial use as one of the key components in the three-way catalytic converters for automobiles [4]. However, as one of the rarest elements in the Earth's crust [5], the scarcity and thus high price of Rh have hindered its large-scale applications. As such, there is an urgent need to increase the utilization efficiency of Rh atoms. To this end, Rh nanocrystals with controlled shapes and twin structures, including cubes [6, 7], octahedra [7], decahedra [8], icosahedra [9], hexagonal plates [10], and concave cubes [11], have been synthesized and tested as heterogeneous catalysts in an effort to enhance the specific activity by optimizing their surface structures. As an alternative to this strategy, core-shell structures, with Rh as the shell and another metal as the core, have been synthesized with different shapes to help increase the surface exposure of Rh atoms [12]. The interior atoms in these structures, however, are still blocked from interacting with reactant molecules. As a solution to this issue, hollow nanostructures such as nanoframes have been fabricated, but this type of nanostructures fail to control the type of facet exposed on the surface [11].

In recent years, nanocages have emerged as a new type of hollow nanostructure featuring both high surface exposure and well-defined surface structure [13]. With sub-nanometer thin walls and capped by a certain type of facets (usually {100} or {111}), they have emerged as promising candidates for catalytic applications with both high activity and selectivity. Notable examples include Pt-based octahedral nanocages toward oxygen reduction [14], Ir-based cubic nanocages toward water oxidation [15], and Ru-based icosahedral nanocages for hydrazine decomposition [16]. The nanocages were prepared by depositing a thin layer of the desired metal onto Pd nanocrystals (*i.e.*, seeds or templates) of different shapes, followed by removal of the Pd core through selective etching to leave behind the nanocages. Despite successful synthesis of several types of nanocages of platinum-group metals (PGMs), it remains a challenge to produce Rh-based nanocages through the same approach. In a previous study, our research group demonstrated the synthesis of Pd@Rh nanocrystals by depositing Rh on Pd nanocrystals of 6–7 nm in size using Rh(OAc)<sub>3</sub> as the precursor [12]. Due to the fast reduction kinetics of this precursor, the reaction temperature was restricted to 185 °C to avoid homogeneous nucleation, which limited the surface diffusion of Rh adatoms on the surface of the seeds. This was especially problematic in the case of nanocubes where the lower coordination of atoms on the {100} surface of cubic seeds (as compared with the {111} surface of octahedral seeds) carries a higher energy barrier to surface diffusion [17]. As a result, layer-by-layer growth mode were only partially achieved when seeds of very small sizes (6–7 nm) were involved and the synthesis failed when switching to seeds of larger sizes (*i.e.*, 18 and 37 nm in that study). Moreover, when examined under high-resolution transmission electron microscope (HRTEM), concavities, terraces, and steps were observed on the side faces due to

inadequate surface diffusion. When these particles are subject to oxidative etching, the three-dimensional structure of the nanocages tend to collapse due to their uneven shell thickness and thus weak mechanical strength.

Herein I report a synthetic protocol to synthesize Pd@Rh nanocrystals featuring smooth, well-defined {100} facets and larger size for the successful preparation of Rh nanocages. Sodium hexachlororhodate(III) ( $\text{Na}_3\text{RhCl}_6$ ) with lower reactivity than  $\text{Rh}(\text{OAc})_3$  (0.431 V *versus* the standard hydrogen electrode,  $V_{\text{SHE}}$ , for  $\text{RhCl}_6^{3-} + 3e \rightarrow \text{Rh} + 6\text{Cl}^-$ , as compared with 0.758  $V_{\text{SHE}}$  for  $\text{Rh}^{3+} + 3e \rightarrow \text{Rh}$ ) [18] was used as a precursor to reduce the reaction rate and thus avoid homogeneous nucleation. The  $\text{Br}^-$  ions from KBr serve as a bifunctional ligand to further slowdown the reaction through ligand exchange [19] and promote the formation of Rh(100) surface [6]. The reaction was conducted at a high temperature of 210 °C to promote surface diffusion. Benefiting from the complete coverage of atomically thin Rh overlayer, the core-shell nanocubes exhibited significantly improved thermal stability when benchmarked against Pd mono-metallic counterparts through *in situ* electron microscopy observation. Through chemical wet etching of the core-shell nanocubes, Rh nanocages with well-defined {100} surface and ultrathin walls were successfully fabricated.

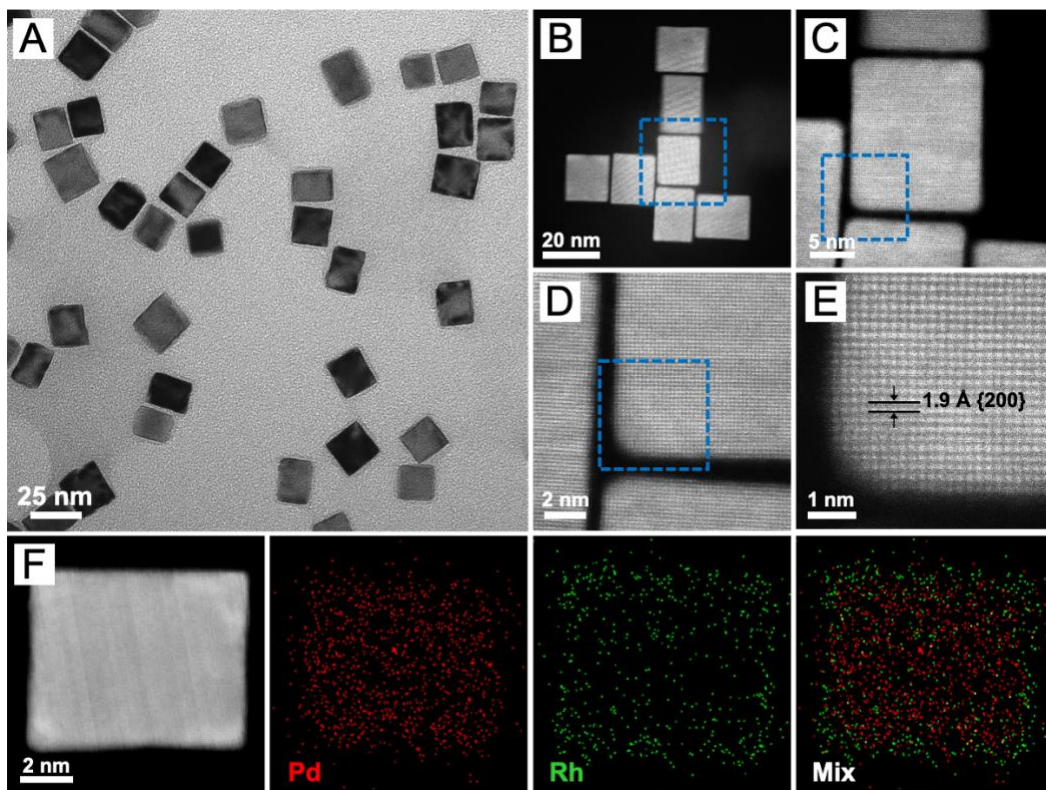
### 3.2 Results and Discussion

I first synthesized Pd nanocubes with an average edge length of 16.2 nm according to a protocol developed by our group [20]. After that, I deposited Rh shells on the Pd nanocubes in a layer-by-layer manner by dropwise adding a triethylene glycol (TEG) solution containing  $\text{Na}_3\text{RhCl}_6$  and poly(vinyl pyrrolidone) (PVP) into another solution

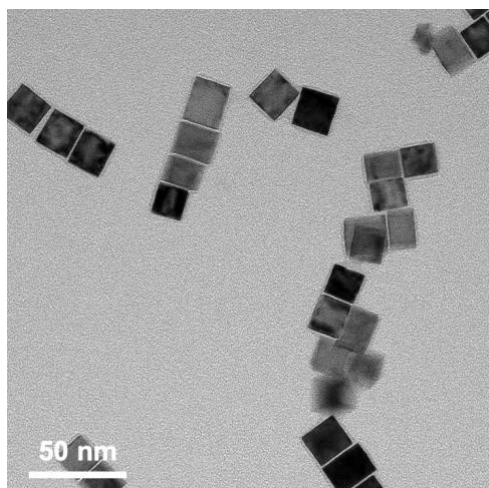
containing TEG, PVP, potassium bromide (KBr), and L-ascorbic acid (AA) under magnetic stirring over a course of 20 h. In this synthesis, AA acted as a reducing agent; TEG served as both a solvent and a precursor to a co-reducing agent; PVP was a colloidal stabilizer. On the other hand, KBr was an additive that had a multifaceted impact on the outcome of the synthesis, which will be discussed later in detail. The synthesis was conducted at a temperature of 210 °C to promote the diffusion of Rh adatoms on Pd surface. Figure 3.1A shows a typical transmission electron microscopy (TEM) image of the as-obtained Pd@Rh core-shell nanocubes, confirming a uniform size and shape of the sample. Unlike previously reported products that were plagued by island growth of Rh and a second population of Rh particles arising from homogeneous nucleation [12], the current product shows 100% layer-by-layer growth for the Rh atoms. The atomic composition of the product was determined to be Pd<sub>81.6</sub>Rh<sub>18.4</sub> using inductively coupled plasma mass spectrometry (ICP-MS), which corresponds to *ca.* three atomic overlayers of Rh on the Pd surface based on an inter-planar distance of 0.19 nm for the {200} planes of face-centered cubic (*fcc*) Rh and the 16.2-nm size of the Pd nanocubes.

Figure 3.1B–E shows high-angle annular dark-field scanning TEM (HAADF-STEM) images taken from a number of adjacent core-shell nanocubes, demonstrating smooth side faces and sharp corners for each nanocube. No atomic terraces, steps, or concavity was observed in the atomic-resolution image shown in Figure 3.1E. Figure 3.1F shows energy-dispersive X-ray (EDX) mapping of an individual Pd@Rh nanocube, revealing the core-shell spatial distribution of the two elements. It is worth mentioning that similar product could be obtained when the Na<sub>3</sub>RhCl<sub>6</sub> precursor is replaced with the same amount of Rh(acac)<sub>3</sub> (Figure 3.2), because Rh(acac)<sub>3</sub> is known to have moderate reduction

kinetics even at elevated temperatures [7]. The chemical states of the two metals were further analyzed by X-ray photoelectron spectroscopy (XPS). As shown in Figure 3.3, the characteristic doublets of  $3d$  orbitals of Rh and Pd were clearly resolved. Each elemental peak was dominated by the zero-valent state, with a very small portion for the oxidated species.



**Figure 3.1.** (A) A typical TEM image of the Pd@Rh<sub>3L</sub> nanocubes. (B–E) HAADF-STEM images of the Pd@Rh<sub>3L</sub> nanocubes at different magnifications. (F) HAADF-STEM image of an individual Pd@Rh<sub>3L</sub> nanocube and the corresponding EDX mappings of Pd and Rh elements.



**Figure 3.2.** A typical TEM image of the Pd@Rh nanocubes obtained using the standard protocol except for replacing  $\text{Na}_3\text{RhCl}_6$  with the same amount of  $\text{Rh}(\text{acac})_3$ .

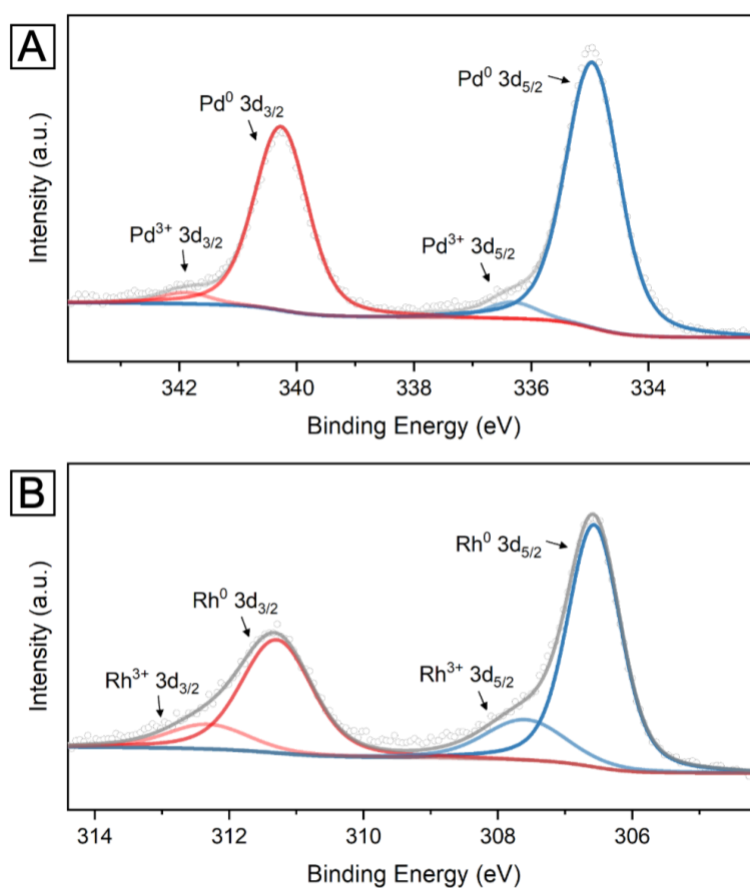


**Figure 3.3.** High-resolution XPS spectra and the corresponding fitted curves of Pd and Rh in the core-shell nanocubes. The zero-valent component is in dominance for both metals.

In order to verify the layer-by-layer growth mode during this synthesis, I reduced the volume of Rh precursor solution added from 5 mL to 3 and 1 mL, respectively. From the TEM images and corresponding HAADF-STEM images of the two samples shown in Figure 3.4, they exhibit a morphology similar to that of the Pd@Rh<sub>3L</sub> sample, including smooth side faces down to atomic scale. No self-nucleated particles were observed, eliminating the possible involvement of Ostwald ripening in the deposition of Rh onto the surface of Pd seeds. The atomic compositions (summarized in Table 3.1) of these two products were determined to be Pd<sub>96.0</sub>Rh<sub>4.0</sub> and Pd<sub>89.7</sub>Rh<sub>10.3</sub>, respectively, which corresponds to 0.6 and 1.5 atomic layers of Rh. In other words, the Rh atoms were indeed deposited on the seeds in a layer-by-layer fashion, with every 1 mL of the precursor solution contributing to *ca.* 0.5 layers of the Rh shell. Note that the atomic percentages of Rh in these samples were lower than the ideal values calculated from the amounts of Pd cubes and Rh precursor added. Specifically, the ideal atomic percentages of Rh were supposed to be 10.9, 19.5, and 26.6% after the addition of 1, 3, and 5 mL of Rh precursor solutions, respectively. The loss of Rh mass during the synthesis can be attributed to the incomplete reduction of the precursor and the formation of Rh clusters that were too small to be collected through centrifugation.

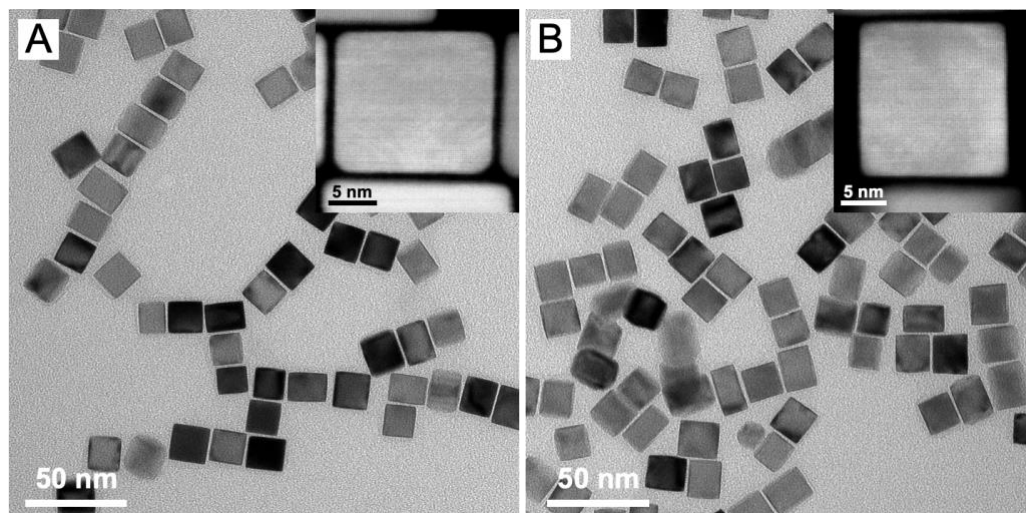


**Figure 3.4.** (A) TEM and HAADF-STEM (inset) images of the Pd@Rh<sub>0.6L</sub> nanocubes. (B) TEM and HAADF-STEM (inset) images of Pd@Rh<sub>1.5L</sub> nanocubes.

**Table 3.1.** Compositions of Pd@Rh nanocubes with different shell thicknesses determined using ICP-MS.

Sample	Atomic percentage (%)	
	Pd	Rh
Pd@Rh <sub>0.6L</sub>	96.0	4.0
Pd@Rh <sub>1.5L</sub>	89.7	10.3
Pd@Rh <sub>3L</sub>	81.6	18.4

Next, I analyzed the surface compositions of the core-shell nanocubes with different shell thicknesses through cyclic voltammetry (CV) scanning in an aqueous electrolyte containing 0.1 M HClO<sub>4</sub> (Figure 3.5). It has been established that the Pd (100) surface shows characteristic voltametric peaks in the hydrogen underpotential deposition region between 0.2–0.3 V *versus* the reversible hydrogen electrode ( $V_{RHE}$ ) but there is no such peak for Rh(100) [7, 21]. Indeed, two distinct peaks could be observed in the CV curve of pristine Pd nanocubes (Figure 3.5A). As more Rh was deposited onto the Pd{100} facets to form 0.6, 1.5, and finally 3 atomic layers of Rh (Figure 3.5B–D), the relative intensities of the voltametric peaks of Pd gradually decreased and eventually became

negligible. These results indicated that the surface of the Pd@Rh<sub>3L</sub> nanocubes was dominated by Rh instead of Pd–Rh alloy, which can be attributed to the immiscibility and thus spontaneous phase segregation between Rh and Pd over the entire composition range [22].

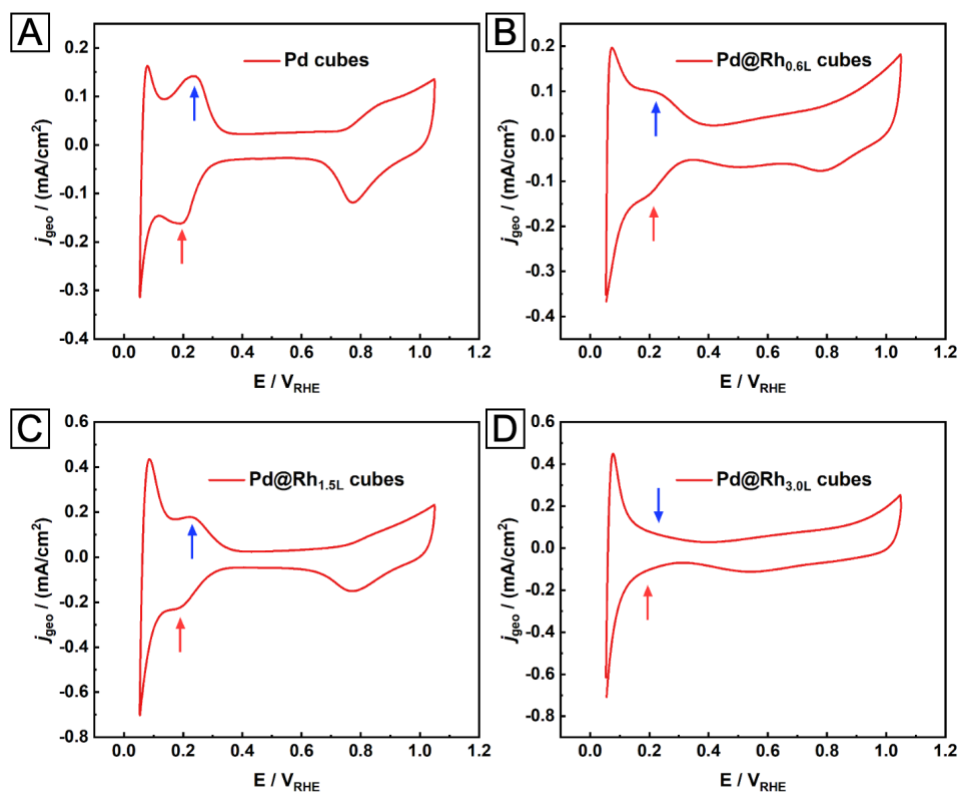


**Figure 3.5.** CV curves obtained from Pd nanocubes and Pd@Rh nanocubes of different thicknesses in an aqueous electrolyte containing 0.1 M HClO<sub>4</sub>.

It is worth emphasizing that a careful control over the reaction conditions, including the injection rate and amount of precursor solution, the reaction temperature, and the additives, is essential to the formation of a smooth surface. During the synthesis, the injection rate of the precursor had to be controlled at a low level in order to keep the concentration of Rh atoms in the reaction mixture at a low level to avoid supersaturation and homogeneous nucleation. In the standard protocol, the injection rate was carefully

controlled at  $0.25 \text{ mL h}^{-1}$  using a syringe pump. As a comparison, when this rate was increased to  $0.5 \text{ mL h}^{-1}$ , a second population of particles (arising from homogeneous nucleation) with sizes significantly smaller than the Pd cubic seeds became visible in the TEM image (Figure 3.6A). As discussed in Figure 3.4, the amount of precursor injected is also important as it directly controls the thickness of the Rh shell. Unfortunately, the Rh shell could not grow thicker than three atomic layers without altering the growth mode. As shown in Figure 3.6, when 7.8 mL of precursor solution was added, island growth was triggered on top of the smooth Rh shell due to inadequate surface diffusion, generating spikes from the corners of each nanocube. Interestingly, each spike has a rectangular shape with right angles under TEM, indicating a  $\{100\}$ -terminated surface. This could be attributed to the  $\{100\}$ -selective capping effect from  $\text{Br}^-$  ions [6, 23]. Moreover, the complex roles of KBr additive should not be overlooked. It has been established that  $\text{Br}^-$  could bind to Rh(III) ions to form a stable complex with low reactivity, thus changing the reaction rate constant of the precursor and slowing down the redox reaction [19]. Indeed, without the addition of KBr, the fast reduction of the Rh precursor would result in homogeneous nucleation and formation of tiny Rh particles instead of Rh shell (Figure 3.6C). Taken together, all the reaction parameters must be optimized in order to generate Pd@Rh nanocubes with a smooth surface while eliminating impurities such as surface islands and small Rh particles.

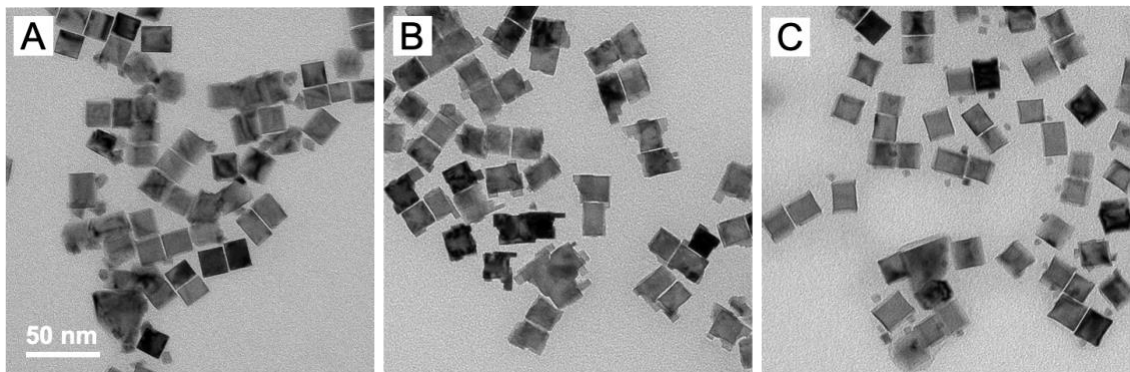


**Figure 3.6.** (A–C) TEM images of products obtained using the standard protocol expect that (A) the injection rate of the precursor was increased to  $0.5 \text{ mL h}^{-1}$ , (B) the amount of precursor solution injected was increased to  $7.8 \text{ mL}$ , and (C) no KBr was introduced.

Similar to the injection rate, reaction temperature is another essential parameter that must be carefully controlled because it influences both the reduction rate of the Rh precursors (*i.e.*, the deposition rate of the Rh atoms) and the surface diffusion rate of Rh adatoms. If the temperature was reduced to  $190 \text{ }^\circ\text{C}$  (Figure 3.7A), the Rh metal mainly existed as self-nucleated small particles instead of a shell on the surface of Pd cubes. This could be attributed to the stronger binding of  $\text{Br}^-$  to the Pd(100) surface at a relatively low temperature. The surface-adsorbed  $\text{Br}^-$  would block the access of Rh atoms to the Pd surface and force them to self-nucleate and generate individual particles [24]. On the other hand, when subject to a higher temperature of  $230 \text{ }^\circ\text{C}$  (Figure 3.7B), the faster reduction of the precursor and thus a higher rate of atom supply led to a deposition rate greater than surface diffusion, triggering island growth that made the surface rough and irregular.

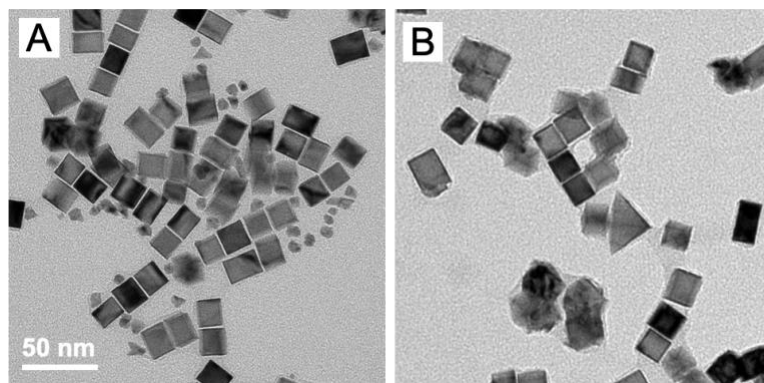


**Figure 3.7.** (A and B) TEM images of products obtained using the standard protocol expect that the temperature was changed to (A) 190 °C and (B) 230 °C, respectively.

As a catalytic metal, Rh is widely used to promote heterogeneous thermal catalytic reactions, such as syngas production and vehicle exhaust treatment, that are operated at elevated temperatures. In order to study the thermal stability of Pd@Rh nanocubes for potential application as thermal catalysts, I loaded the Pd and Pd@Rh samples onto a chip with 30–50 nm-thick SiN<sub>x</sub> membrane surrounded by a heating circuit and subjected them to *in situ* heating and observation in TEM. As shown in Figure 3.8, the original shapes of both samples exhibited sharp corners and smooth edges at room temperature. However, as the temperature was elevated, the shape evolution of these two samples started to differ. After being heated at 300 °C in vacuum for 30 min, the corners of each Pd cube became truncated and those close to each other started to merge together. For Pd@Rh cubes, in contrast, essentially no shape change was observed. When the temperature was further increased to 400 °C and then 500 °C, individual Pd cubes became more rounded and the particles in touch started to fuse into one particle with uniform contrast under TEM. On the contrary, the cubic shape of the Pd@Rh nanocubes was still well preserved, with only slight corner truncation. At a high temperature of 600 °C, the Pd nanocubes became near-spherical while the Pd@Rh nanocubes possessed a morphology similar to that of the Pd

sample at 300 °C. Taken together, with the full coverage by and protection from refractory Rh overlayer on Pd surface, the Pd@Rh nanocubes exhibited a thermal stability almost 300 °C higher than pristine Pd nanocubes of similar sizes, making the former promising candidate as thermal catalysts with higher utilization efficiency than pure Rh nanocrystals and uncompromised great thermal stability.

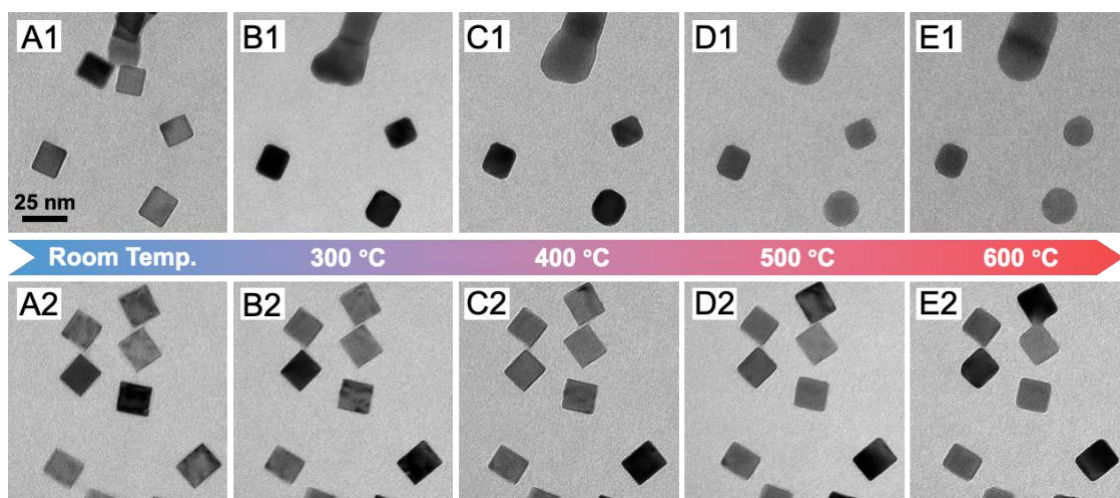


**Figure 3.8.** *In situ* TEM images recorded from the same (1) Pd cubes and (2) Pd@Rh<sub>3L</sub> cubes at (A) room temperature and then heated to (B) 300, (C) 400, (D) 500, and (E) 600 °C for 30 min, respectively. The scale bar in (A1) applies to all panels.

As noted earlier, the well-defined core–shell structure with smooth, three atomic layer-thick Rh shell could benefit the production of Rh nanocages by removing Pd in the core to leave behind Rh shell only. Owing to the relatively large difference in redox potential between Fe<sup>3+</sup>/Fe<sup>2+</sup> and PdBr<sub>4</sub><sup>2-</sup>/Pd (0.77 V<sub>SHE</sub> for Fe<sup>3+</sup>/Fe<sup>2+</sup> vs. 0.49 V<sub>SHE</sub> for PdBr<sub>4</sub><sup>2-</sup>/Pd) [11], this process can be easily achieved by treating the core–shell particles in an aqueous etchant containing KBr, FeCl<sub>3</sub>, and HCl at 80 °C for 1 h. In the etching process, the Fe<sup>3+</sup> from FeCl<sub>3</sub> served as an oxidizing agent to react with the Pd atoms in the core whereas Br<sup>-</sup> coordinated with the resultant Pd<sup>2+</sup> to form PdBr<sub>4</sub><sup>2-</sup> which was then dissolved

into the aqueous solution and removed from the nanocrystals. The use of HCl helped prevent both  $\text{Fe}^{3+}$  and  $\text{Fe}^{2+}$  from hydrolysis. Figure 3.9A and B shows typical TEM and HAADF-STEM images of the as-obtained Rh nanocages, respectively. A lattice spacing of 1.9 Å could be measured from the atomic-resolution image in Figure 3.9C, in agreement with the value obtained in Figure 3.1E. This result demonstrated that the crystal structure of the Rh shell was well-preserved during the etching process. I conducted ICP-MS to quantitatively analyze the elemental composition of the product. The atomic percentage of Rh increased from 18.4% to over 90% after the etching of Pd core, indicating a highly efficient and selective Pd removal process. Taken together, these data confirmed that the nanocages were essentially made of Rh. In order to demonstrate the necessity of using Pd nanocubes of larger sizes as seeds, Pd@Rh nanocrystals of smaller sizes were also prepared by employing Pd cubes of smaller sizes as seeds for the production of Rh nanocages as a comparison (Figure 3.10). It is obvious from the TEM images that core-shell nanocrystals possess different types of structural defects, including corner truncations, terraces, and steps (Figure 3.10A). The nanocages produced from these products are comprised of incomplete structure and debris (Figure 3.10B).

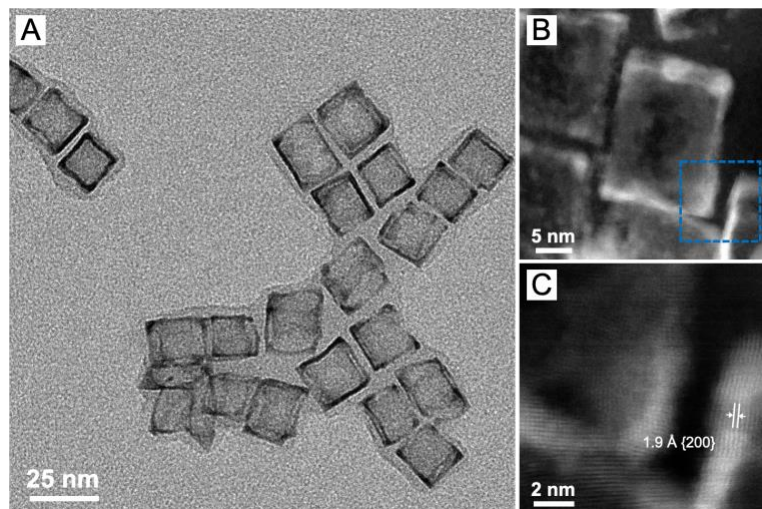


**Figure 3.9.** (A) A TEM image of Rh nanocages obtained by etching away Pd in Pd@Rh<sub>3L</sub> cubes using an FeCl<sub>3</sub>-based etchant. (B and C) HAADF-STEM images of Rh cages at two different magnifications.

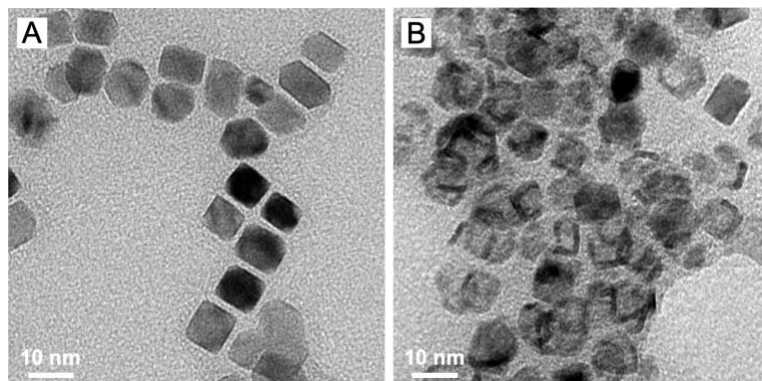


**Figure 3.10.** (A) Pd@Rh nanocubes prepared by using 6-nm Pd cubes as seeds. (B) Rh nanocages produced through etching of the Pd@Rh nanocubes in (A).

### 3.3 Conclusion

In summary, I have demonstrated the synthesis of Pd@Rh core-shell nanocubes with an ultrathin Rh shell and well-defined {100} facets. Under optimized injection rate of the precursor and reaction temperature, together with the addition of KBr, the growth mode was adjusted to layer-by-layer instead of surface island growth or self-nucleation. The complete coating of Pd nanocubes by a Rh shell significantly enhanced their thermal

stability, as established by *in situ* TEM observation. Moreover, Rh nanocages with ultrathin walls could be readily fabricated through wet etching. I also found that the size of the Pd seeds is of critical importance for generating a uniform shell with high mechanical strength to keep the nanocages from collapse during the etching process. It is expected that the method reported here will facilitate the development of novel catalysts with high utilization efficiency of precious metals in addition to high thermal stability.

### 3.4 Experimental Section

**Chemicals and Materials.** Triethylene glycol (TEG, 99%) was purchased from J. T. Baker. Poly(vinyl pyrrolidone) (PVP, with an average molecular weight of 55,000), potassium chloride (KCl, 99%), potassium bromide (KBr, 99%), hydrochloric acid (HCl, 37%), iron(III) chloride (FeCl<sub>3</sub>, 97%), sodium hexachlororhodate(III) (Na<sub>3</sub>RhCl<sub>6</sub>, 97%), rhodium(III) acetylacetonate (Rh(acac)<sub>3</sub>, 97%) were obtained from Sigma-Aldrich. L-ascorbic acid (AA, 99%) was ordered from BioXtra. Ethanol (anhydrous) was ordered from KOPTEC. Acetone was obtained from VWR Chemicals BDH. Syringes and syringe pump were purchased from KD Scientific. The temperatures of all syntheses were monitored using a thermal sensor acquired from ACE Glass. Aqueous solutions were prepared using deionized (DI) water with a resistivity of 18.2 MΩ·cm at room temperature.

**Synthesis of Pd Cubes with different sizes.** Pd cubes were synthesized according to a protocol reported by our group. In a typical synthesis of 18-nm Pd cubes, 8.0 mL of an aqueous solution containing PVP (105 mg), AA (60 mg), and KBr (600 mg) was placed in a 20-mL vial and pre-heated at 80 °C for 10 min under magnetic stirring (400 rpm). Afterwards, 3.0 mL of an aqueous solution containing 57 mg of Na<sub>2</sub>PdCl<sub>4</sub> was added using

a pipette. After the vial had been capped, the reaction was continued at 80 °C for 3 h. The solid products were collected by centrifugation and washed three times with water, and then re-dispersed in water for further use. For the synthesis of 6-nm cubes, 5 mg KBr and 185 mg KCl were added instead.

**Synthesis of Pd@Rh nanocubes with different sizes and shell thicknesses.** In a typical synthesis of 18-nm Pd@Rh<sub>3L</sub> nanocubes, 5 mL of a TEG solution containing Pd cubes (0.48 mg), AA (25 mg), KBr (50 mg), and PVP (100 mg) was transferred into a glass vial and heated at 210 °C under magnetic stirring (380 rpm) for 10 min. After that, 5 mL of another TEG solution containing 0.63 mg of Na<sub>3</sub>RhCl<sub>6</sub> and 100 mg PVP was added into the flask at 0.25 mL h<sup>-1</sup>. After all the precursor solution had been added, the reaction was continued for another one hour and solid products were then collected by precipitation with acetone, washed three times with a mixture of ethanol and acetone, and finally re-dispersed in water for further use. To obtain Pd@Rh<sub>1.5L</sub> and Pd@Rh<sub>0.6L</sub>, the amounts of precursor solution added were reduced to 3 mL and 1 mL, respectively. To obtain 8-nm Pd@Rh nanocubes, 0.18 mg of the 6-nm Pd cubes were used instead.

**Formation of Rh nanocages.** Chemical etching was conducted in an acidic aqueous solution to generate Rh nanocages. Typically, 1 mL of the as-prepared Pd@Rh nanocubes was dispersed in a mixture containing 50 mg of KBr, 50 mg of PVP, 10 mg of FeCl<sub>3</sub>, 0.06 mL of HCl (37%), and 6 mL of H<sub>2</sub>O and then heated at 80 °C under magnetic stirring (380 rpm) for 1 h. Afterwards, the solid product was collected by centrifugation, washed three times with ethanol, and finally re-dispersed in water for further characterization.

**Characterizations.** Transmission electron microscopy (TEM) images were taken using a Hitachi HT7700 microscope operated at 120 kV. High-angle annular dark-field scanning transmission electron microscopy (HAADF-STEM) images and energy-dispersive X-ray (EDX) spectroscopy mapping data were acquired on an aberration-corrected Hitachi HD-2700 STEM operated at 200 kV. Inductively coupled plasma mass spectrometry (ICP-MS, NexION 300Q, PerkinElmer) was used to determine the metal contents in the as-obtained nanocrystals. X-ray diffraction (XRD) patterns were obtained with a PANalytical X'Pert PRO Alpha-1 diffractometer using a 1.8 kW ceramic copper tube source. The X-ray photoelectron spectroscopy (XPS) data were collected on a Thermo K-Alpha spectrometer with an Al K $\alpha$  source.

### 3.5 Notes to Chapter 3

Part of this Chapter is adapted from the article “Synthesis of Pd@Rh Nanocubes with Well-Defined {100} Surface and Controlled Shell Thicknesses for the Fabrication of Rhodium Nanocages” published in *Surface Science* [25].

### 3.6 References

- [1] Liu, K.; Wang, A. Q.; Zhang, T. *ACS Catalysis* **2012**, *2*, 1165–1178.
- [2] Parvulescu, V. I.; Grange, P.; Delmon, B. *Catalysis Today* **1998**, *46*, 233–316.
- [3] Etayo, P.; Vidal-Ferran, A. *Chem. Soc. Rev.* **2013**, *42*, 728–754.
- [4] Yakoumis, I.; Panou, M.; Moschovi, A. M.; Pantias, D. *Cleaner Engineer. Technol.* **2023**, *3*, 100112.
- [5] Ojeda, C. B.; Rojas, F.S. *Talanta* **2007**, *71*, 1–12.

- [6] Zhang, H.; Li, W.; Jin, M.; Zeng, J.; Yu, T.; Yang, D.; Xia, Y. *Nano Lett.* **2011**, *11*, 898–903.
- [7] Zhao, M.; Chen, Z.; Shi, Y.; Hood, Z. D.; Lyu, Z.; Xie, M.; Chi, M.; Xia, Y. *J. Am. Chem. Soc.* **2021**, *143*, 6293–6302.
- [8] Lee, S.R.; Vara, M.; Hood, Z. D.; Zhao, M.; Gilroy, K. D.; Chi, M.; Xia, Y. *ChemNanoMat* **2018**, *4*, 66–70.
- [9] Choi, S. I.; Lee, S. R.; Ma, C.; Oliy, B.; Luo, M.; Chi, M.; Xia, Y. *ChemNanoMat* **2016**, *2*, 61–66.
- [10] Jang, K.; Kim, H. J.; Son, S. U. *Chem. Mater.* **2010**, *22*, 1273–1275.
- [11] Xie, S.; Lu, N.; Xie, Z.; Wang, J.; Kim, M. J.; Xia, Y. *Angew. Chem. Int. Ed.* **2012**, *51*, 10266–10270.
- [12] Choi, S. I.; Young, A.; Lee, S. R.; Ma, C.; Luo, M.; Chi, M.; Tsung, C.-K.; Xia, Y. *Nanoscale Horiz.* **2019**, *4*, 1232–1238.
- [13] Zhao, M.; Wang, X.; Yang, X.; Gilroy, K. D.; Qin, D.; Xia, Y. *Adv. Mater.* **2018**, *30*, 1801956.
- [14] Zhang, L.; Roling, L. T.; Wang, X.; Vara, M.; Chi, M.; Liu, J.; Choi, S. I.; Park, J.; Herron, J. A.; Xie, Z.; Mavrikakis, M.; Xia, Y. *Science* **2015**, *349*, 412–416.
- [15] Zhu, J.; Chen, Z.; Xie, M.; Lyu, Z.; Chi, M.; Mavrikakis, M.; Jin, W.; Xia, Y. *Angew. Chem. Int. Ed.* **2019**, *58*, 7244–7248.
- [16] Zhao, M.; Xu, L.; Vara, M.; Elnabawy, A. O.; Gilroy, K. D.; Hood, Z. D.; Zhou, S.; Figueroa-Cosme, L.; Chi, M. F.; Mavrikakis, M.; Xia, Y. *ACS Catalysis* **2018**, *8*, 6948–6960.
- [17] Xia, X.; Xie, S.; Liu, M.; Peng, H.-C.; Lu, N.; Wang, J.; Kim, M. J.; Xia, Y. *Proc. Natl. Acad. Sci. U. S. A.* **2013**, *110*, 6669–6673.
- [18] Milazzo, G.; Carioli, S. *Tables of Standard Electrode Potentials*; Wiley: New York, 1979.
- [19] Yao, S.; Yuan, Y.; Xiao, C.; Li, W.; Kou, Y.; Dyson, P. J.; Yan, N.; Asakura, H.; Teramura, K.; Tanaka, T. *J. Phys. Chem. C* **2012**, *116*, 15076–16086.

- [20] Jin, M.; Liu, H.; Zhang, H.; Xie, Z.; Liu, J.; Xia, Y. *Nano Res.* **2011**, *4*, 83–91.
- [21] Previdello, B. A. F.; Sibert, E.; Maret, M.; Soldo-Olivier, Y. *Langmuir* **2017**, *33*, 2087–2095.
- [22] Tripathi, S. N.; Bharadwaj, S. R. *J. Phase Equilibria* **1994**, *15*, 208–212.
- [23] Yang, T.-H.; Shi, Y.; Janssen, A.; Xia, Y. *Angew. Chem. Int. Ed.* **2020**, *59*, 15378–15401.
- [24] Xie, S.; Peng, H.-C.; Lu, N.; Wang, J.; Kim, M. J.; Xie, Z.; Xia, Y. *J. Am. Chem. Soc.* **2013**, *135*, 16658–16667.
- [25] Wang, C.; Lyu, Y.; Xia, Y. *Surf. Sci.* **2023**, *736*, 122339.

# CHAPTER 4. FACET-CONTROLLED SYNTHESIS OF PLATINUM-GROUP-METAL QUATERNARY ALLOYS: THE CASE OF NANOCUBES AND {100} FACETS

## 4.1 Introduction

Multi-metallic alloys refer to solid solutions comprised of three or more elements [1–3], and they have received ever-increasing interest as an innovation platform for the rapid development of more effective heterogeneous catalysts [4–7]. Because of the inherent complexity in composition and thus numerous possible atomic configurations, the surface of multi-metallic nanoparticles (MMNPs) offers an extremely large number of distinctive coordination environments to generate a near-continuum distribution of adsorption energies for the key intermediates of various reactions [8], especially those involving complex electron transfer processes [9]. More significantly, the optimal binding sites can dominate the catalytic process and thereby determine the overall activity and selectivity. When prepared as nanocrystals featuring well-controlled compositions and surface atomic structures, MMNPs hold great promises for the accelerated discovery of advanced catalytic materials with exceptional activity and selectivity. Furthermore, various studies have demonstrated that the high-entropy nature of MMNPs (*e.g.*, RuRhPdPtCe nanoparticles) would endow them with high durability and efficiency when used as catalysts toward high-temperature reactions such as ammonia oxidation [4, 10], suggesting a viable system for the fabrication of robust catalysts.

A number of techniques have been developed to generate MMNPs, with the simplest one based on cryomilling [11]. The samples obtained using this technique typically lack controls in terms of size, composition, and morphology. The samples have been greatly improved in quality by switching to advanced techniques [2, 4, 12, 13], including those involving carbothermal shock [4], fast moving bed pyrolysis [12] and nanoreactor-confined calcination [2, 13]. These techniques rely on the fast heating of a mixture of metal precursors to a temperature greater than 900 °C, followed by fast quenching, to generate a single-phase MMNPs. Recently, a number of solution-phase methods have also been explored for the synthesis of MMNPs [9, 14–17], with notable examples including those built on polyol reduction [9], laser ablation towards water [14], ultrasonication-assisted wet chemistry [15], droplet-mediated electrodeposition [16], and solvothermal conditions [17]. A combination of solution-phase colloidal synthesis and thermal annealing has also been explored [18]. Despite remarkable progress, it remains an unmet challenge for the robust synthesis of MMNPs featuring all merits key to the establishment of structure-property relationship and thus theory-guided design of catalytic materials. In general, the MMNPs reported in literature are often plagued by the following issues: *i*) relatively large (>10 nm) and/or broadly distributed sizes; *ii*) a poorly defined surface in terms of both composition and atomic structure; *iii*) a polycrystalline structure with multiple domains in the same particle; and *iv*) multiple phases rather than a single phase. Due to these issues, no prior study has been able to provide atomistic information about the surface in terms of elemental composition and distribution. As a result, we still do not have a quantitative and accurate description of the structure-property relationship

for MMNPs, not mentioning its implication for the rational development of improved or new catalysts.

Among all the aforementioned techniques, solution-phase colloidal synthesis is one of the most promising approaches toward robust and controlled synthesis of MMNPs. For instance, it was recently reported that multi-metallic nanoribbons could be synthesized through a multi-step process involving galvanic exchange between metal precursors and Ag nanowire template and subsequent removal of the template [19]. Nevertheless, the product of this synthesis was essentially polycrystalline. So far, none of the synthetic protocols has succeeded in producing MMNPs with well-controlled composition and shape (or surface atomic structure). The failure can be attributed to two main reasons. As for composition, there is a lack of control over the rates at which the constituent metal atoms are formed. In the case of surface structure, a robust and universal strategy is yet to be demonstrated for regulating the shape evolution.

The opportunities and challenges noted above motivate me to develop a transformative method capable of generating MMNPs with controlled elemental compositions and surface structures. I focus on platinum-group metals (PGMs) for their similarity in crystal structure, widespread use in industrial catalysis, and recent advancement in their synthesis as nanocrystals with well-controlled shapes [20, 21]. Through the use of seed-mediated growth involving well-defined and stable cubic seeds and halide-free precursors, together with a tight control over the reduction kinetics, here I report a robust method for the synthesis of nanocrystals featuring {100} facets and a nearly equimolar RuRhPdPt alloy on the surface. Although many previous studies reported the capability to manipulate the compositions of MMNPs, this work demonstrates the

feasibility to not only control the surface composition of MMNPs, but also manipulate their facet or atomic arrangement on the surface. The as-prepared alloy nanocubes exhibited superior thermal stability in terms of both shape and composition, as well as enhanced catalytic performance toward ethanol oxidation.

## 4.2 Results and Discussion

**Synthesis and Characterization of Rh@RuRhPdPt Alloy Nanocubes.** I began with the preparation of cubic seeds for the eventual presentation of {100} facets on the alloy nanocrystals. To ensure adequate surface diffusion of adatoms across the surface [22], the seeds are supposed to be compact in size, chemically and thermally stable, and well-defined in terms of facet or surface atomic structure. Among the candidates, Rh nanocubes stand out as an optimal choice because they can be readily synthesized with an edge length down to 4.5 nm [23], together with an outstanding thermal stability because of the high Rh–Rh bond energy ( $285 \text{ kJ mol}^{-1}$ , as compared to  $100 \text{ kJ mol}^{-1}$  for Pd–Pd) [24]. If needed, Rh nanocrystals in other shapes and surface atomic structures can also be synthesized using colloidal methods. Figure 4.1A shows a typical transmission electron microscopy (TEM) image of Rh cubes synthesized using a published protocol [23]. I then conducted seed-mediated growth to conformally deposit an alloy shell on the Rh cubic seeds for the generation of Rh@alloy nanocrystals with a cubic shape (denoted Rh@A thereafter). To enable the epitaxial growth of an ultrathin, conformal shell, I used a relatively high temperature of  $220 \text{ }^\circ\text{C}$  and a relatively weak reducing agent based on tetraethylene glycol (TTEG) to promote the surface diffusion of adatoms and decelerate the reduction of metal precursors, respectively. To avoid the possible involvement of oxidative etching, I used halide-free metal acetylacetonate complexes,  $\text{M}(\text{acac})_x$ , as the precursors [22, 25]. A major

challenge in utilizing these precursors is their enormous difference in reactivity and thus reduction kinetics. When added into the reaction solution in one shot without any intervention, these precursors will be reduced sequentially rather than simultaneously, making it impossible to control the elemental composition and surface atomic structure of the as-deposited shell [22]. Figure 4.1B shows a TEM image of the products obtained by injecting a mixture of the precursors in one shot. The truncated octahedral or cuboctahedral shape of the products suggested a growth mode in which the atoms were piled up on the {100} facets of the seeds in the form of pyramids to generate {111} facets, rather than being deposited in a layer-by-layer fashion to replicate the {100} facets on the seeds. The appearance of particles smaller than the seeds also indicated the occurrence of homogeneous nucleation in the reaction solution, in addition to the desired heterogeneous nucleation on the seeds.

To address the issues of homogeneous nucleation and inadequate surface diffusion, a syringe pump and a capillary tube were employed to introduce the precursor mixture in the form of tiny droplets, with only a small quantity of precursors (*ca.* 2.2 nmol for each metal element) in each droplet. During the dropwise addition at a rate of 10 mL h<sup>-1</sup>, the atoms freshly formed from all the four precursors were deposited onto the seeds concurrently and then allowed to diffuse across the surface to form a uniform layer, resulting in the formation of a conformal shell comprised of an alloy of the four elements. After adding 10 mL (Figure 4.1C) and 18 mL (Figure 4.1D) of the precursor mixture (0.5 mM for each precursor) into a reaction solution containing 3.0 mg of the Rh cubic seeds, nanocubes with a well-retained cubic shape but enlarged sizes were obtained. No self-nucleation was observed, demonstrating the dominance of surface reduction and layer-by-

layer growth on the {100} facets of the cubic seeds. The edge length of the cubic nanocrystals increased from 5.1 nm to 6.6 nm (Figure 4.1E), equivalent to an alloy shell of 3–4 atomic layers in thickness.

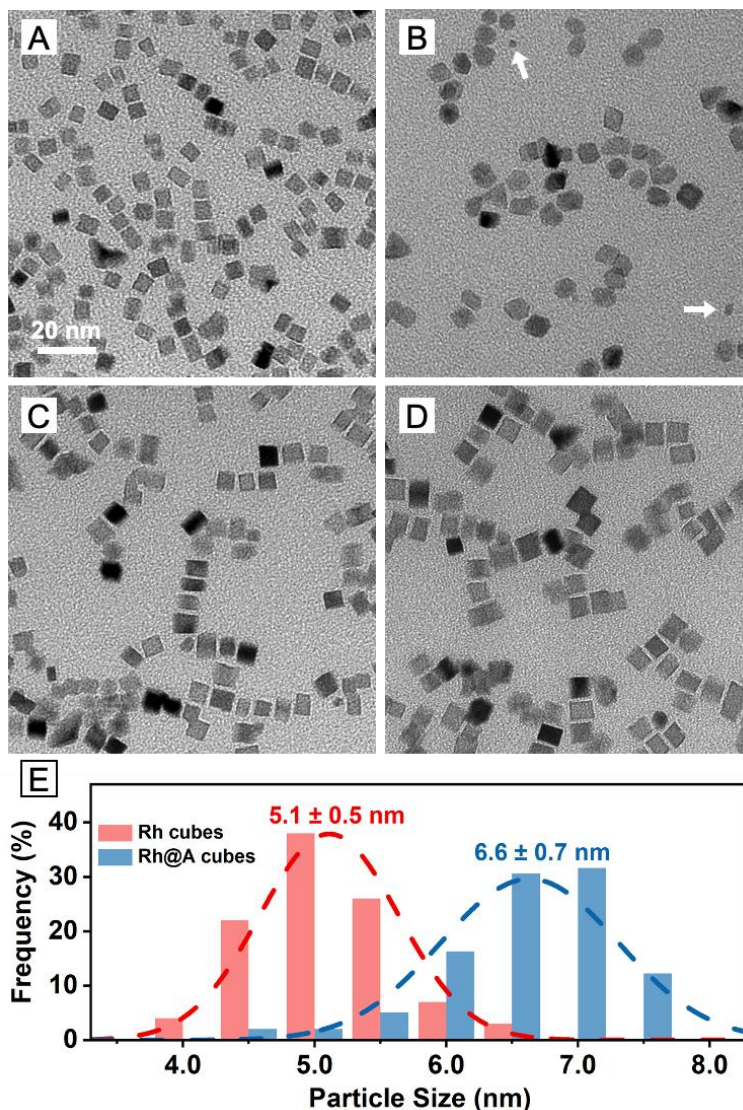


**Figure 4.1.** TEM images of (A) the Rh cubic seeds and the products prepared via (B) one-shot injection of 18 mL or dropwise addition of (C) 10 mL and (D) 18 mL of the precursor mixture, respectively. The arrows in (B) indicate a second population of particles arising from homogeneous nucleation. The scale bar applies to all panels. (E) Size distributions of the Rh cubic seeds in panel A and the core–shell cubes in panel D.

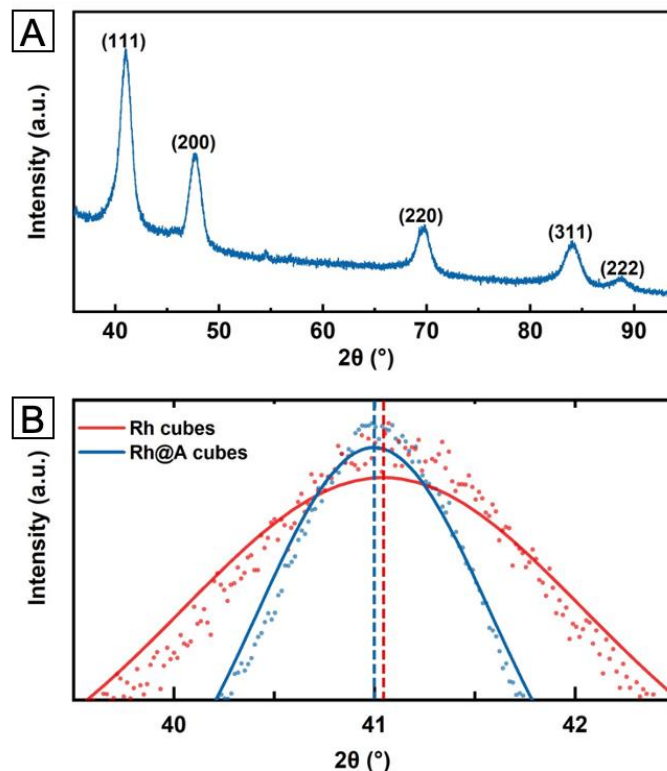


**Figure 4.2.** (A) XRD pattern recorded from the 6.6-nm core–shell nanocubes. (B) Comparison of the normalized (111) diffraction peaks from the Rh cubes (*i.e.*, the seeds) and core–shell cubes.

The single-phase, face-centered cubic (*fcc*) structure of the product was validated by the X-ray diffraction (XRD) pattern in Figure 4.2. The characteristic peaks of *fcc* structure can be clearly observed in Figure 4.2A. Compared to that of Rh seeds, the normalized (111) diffraction peak of the Rh@A cubes was narrowed and slightly shifted to a lower  $2\theta$  value, indicating an enlarged particle size and the formation of an alloy (Figure 4.2B). According to the Scherrer Equation:

$$r = K \cdot \lambda / (\beta \cdot \cos\theta) \quad (4.1)$$

where  $r$  is the mean crystallite size;  $K$  is a shape factor that has a typical value of about 0.89;  $\lambda$  is the X-ray wavelength;  $\beta$  is the peak width at half the maximum intensity;  $\theta$  is the

Bragg angle. In this work,  $\lambda_{\text{Cu-K}\alpha} = 0.154 \text{ nm}$ ;  $\beta_{(111)} = 1.27^\circ = 0.0222 \text{ rad}$ ;  $\theta_{(111)} = 20.50^\circ = 0.358 \text{ rad}$ . As such, the mean crystallite size calculated from the (111) peak was 6.17 nm, consistent with the edge length derived from TEM images (Figure 4.1E) and further confirming the single-crystal nature of the product. As a comparison, many of the colloidal MMNPs reported in previous studies exhibited weak XRD signals and much broadened XRD peaks, implying the polycrystalline structure of these products [9, 19, 26, 27]. The elemental states of the four metals were further confirmed by X-ray photoelectron spectroscopy (XPS). As shown in Figure 4.3 and Figure 4.4, the characteristic doublets of 3*d* orbitals of Ru, Rh, and Pd and 4*f* orbitals of Pt were clearly resolved. The valence band spectrum of Rh@A (Figure 4.5) measured by XPS is “featureless”, revealing a common characteristic of MMNPs originating from the orbital hybrid [26, 27]. This result indicates that the atoms in MMNPs have various atomic configurations and thus lower degeneracy in energy level, in contrast to mono-metallic nanoparticles in which most atoms would have identical atomic configuration [27]. Table 4.1 shows a summary of the atomic percentage of each element derived from the inductively-coupled plasma mass spectrometry (ICP-MS) and XPS data.

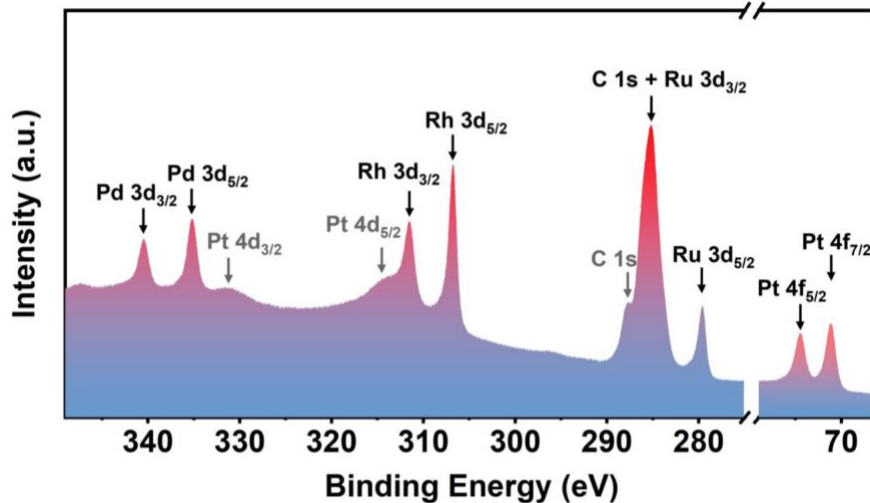


**Figure 4.3.** Core-level XPS spectra recorded from the core-shell cubes in the regions of 275–350 eV and 65–80 eV.

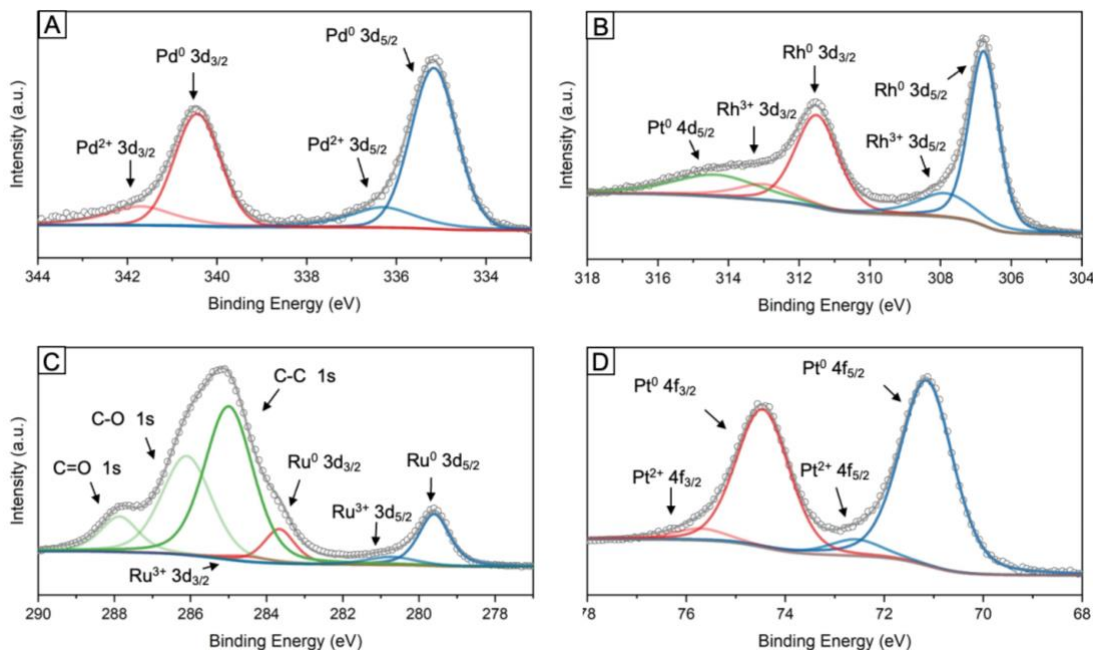


**Figure 4.4.** High-resolution XPS spectra and the corresponding fitted curves of the four metals in the core-shell cubes. The zero-valent component is in dominance for each metal.

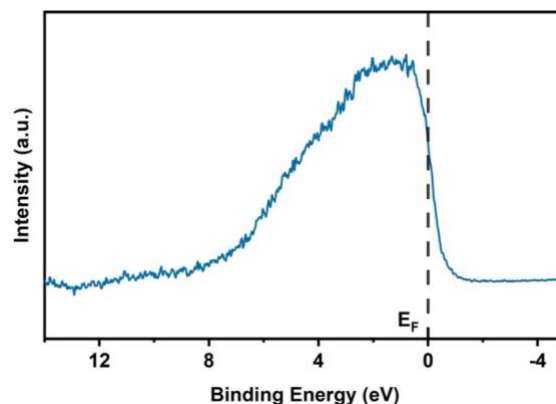


**Figure 4.5.** XPS valence band structure of the core–shell cubes after background subtraction. The dashed line indicates the position of Fermi energy level ( $E_F$ ).

**Table 4.1.** Compositions of the core–shell nanocubes derived from ICP-MS and XPS measurements.

source	atomic percentage (%)			
	Rh	Ru	Pd	Pt
ICP-MS	52.9	13.8	17.4	15.8
XPS	43.3	18.7	22.1	15.9

I also characterized the atomic structure and distribution of the elements in each Rh@A cube using advanced electron microscopy. Figure 4.6A shows a high-angle annular dark-field scanning transmission electron microscopy (HAADF-STEM) image taken from a Rh@A cube along the [001] zone axis. The lattice fringe spacing of 1.9 Å can be assigned to the {200} planes. According to the energy-dispersive X-ray spectroscopy (EDX) line profiles in Figure 4.6B, Rh was distributed throughout the entire particle, but with a higher intensity over a distance of *ca.* 5 nm in the middle. In contrast, the other three metals were mainly distributed in the outmost layer of *ca.* 1 nm thick on both sides. The EDX mapping in Figure 4.6C confirms a cubic core comprised of Rh and a shell containing all the four elements as a uniform alloy.

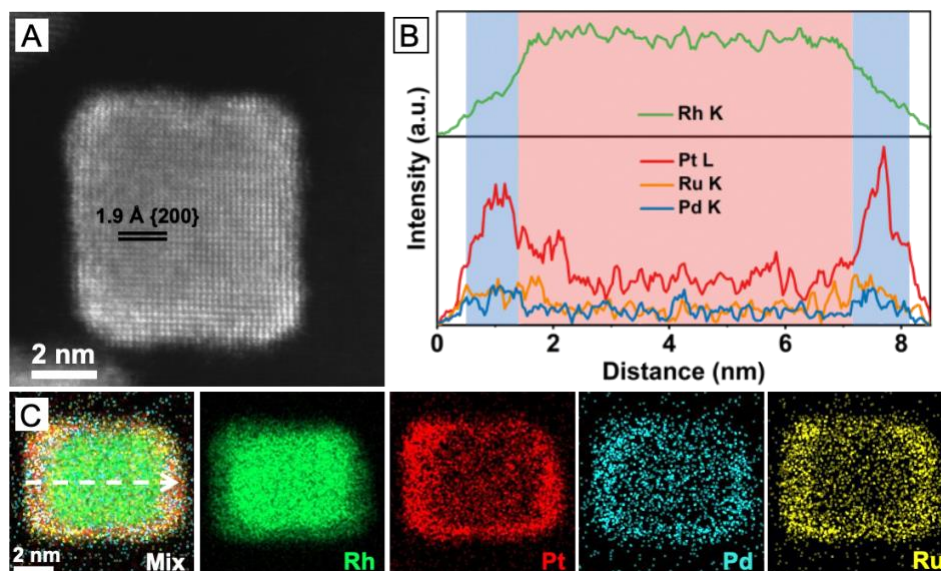


**Figure 4.6.** (A) HAADF-STEM image of a core-shell cube. (B) Line profiles of EDX intensities across the particle as indicated in panel C. (C) EDX elemental mapping of a core-shell cube, showing the spatial distributions of Rh, Pt, Pd, and Ru.

**Mechanistic Study of the Synthesis.** As demonstrated in Figure 4.1, during the synthesis of Rh@A nanocrystals, the injection rate of the precursor mixture had to be controlled in order to keep the deposition rates of metal atoms at a low level to avoid homogeneous nucleation. Besides the injection rate, the reaction temperature is another important parameter that should be taken into consideration to control both the reduction rate of the metal precursors (*i.e.*, the deposition rate of the resultant metal atoms) and the surface diffusion rate of adatoms. In general, the influences of reaction temperature and injection rate share some similarities, as they both affect the reaction rate directly. It is necessary to have a sufficiently high temperature to support not only the generation of metal atoms through reduction reactions but also their surface diffusion. However, if the temperature is too high, the drastically increased deposition rate could result in a shift of the growth mode. Figure 4.7 shows TEM images of products prepared using the standard

protocol except for the use of higher temperatures. At 240 °C (Figure 4.7A) and 250 °C (Figure 4.7B), nanocrystals featuring octahedral and cuboctahedral shapes instead of a cubic shape were obtained. Meanwhile, homogeneous nucleation was triggered as the concentration of freshly formed metal atoms in the reaction mixture was elevated. By reducing the concentration of each precursor to 0.25 mM at 240 °C (Figure 4.7C), the reduction rates of the precursors could be reduced to achieve layer-by-layer growth, yet homogeneous nucleation still occurred. The distinct contrast between the morphologies of these samples and that of the standard sample shown in Figure 4.1D highlights the importance to optimize the reaction temperature for the formation of desired products.

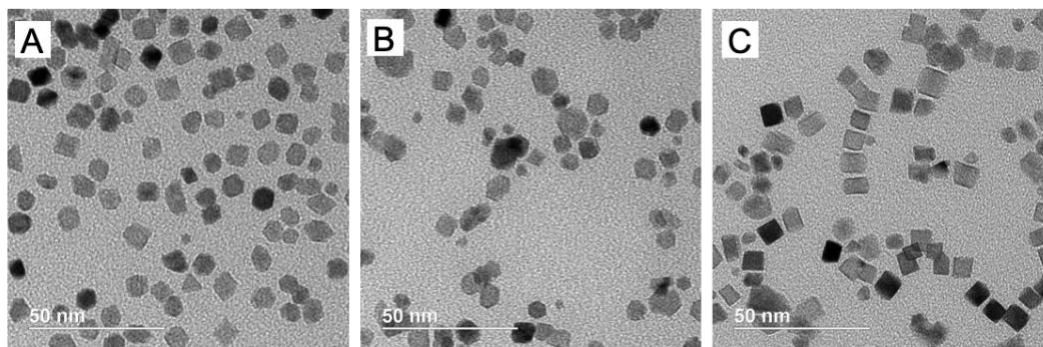


**Figure 4.7.** Influence of the reaction temperature. (A and B) TEM images of the products prepared using the standard protocol except for the use of higher temperatures: (A) 240 °C and (B) 250 °C, respectively. (C) TEM image of the product obtained using the standard protocol except for the use of 240 °C while the concentration of each precursor was reduced to 0.25 mM.

To achieve a quantitative understanding of the layer-by-layer growth mode, I analyzed the reduction kinetics of the four precursors under the same experimental conditions. Figure 4.8A shows a comparison of the concentrations of the precursors measured using ICP-MS. Even though started at the same concentration, the instantaneous concentrations of  $M(\text{acac})_x$  at the same time point differed substantially from each other.

Specifically, Pd(acac)<sub>2</sub> was almost depleted after 5 min into the reaction whereas nearly 50% of Rh(acac)<sub>3</sub> still remained after 30 min, confirming their remarkable difference in term of reactivity. From these data, I obtained the rate constants (Figure 4.8B), which was further used to calculate the instantaneous concentrations and thus reduction rates of the precursor under dropwise addition. Below is a detailed discussion of the mathematical derivation process.

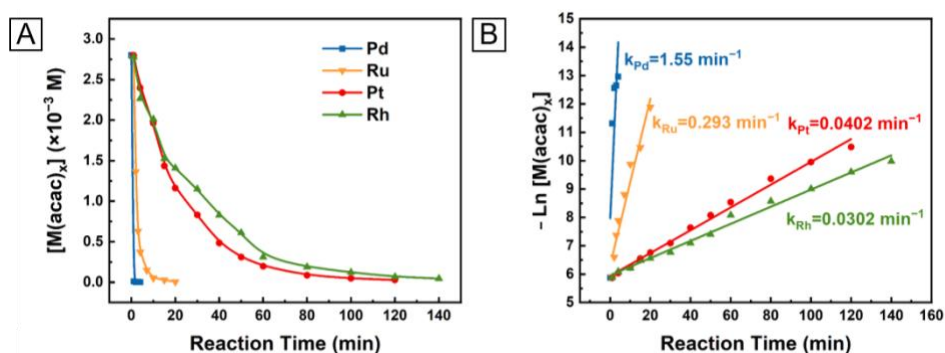


**Figure 4.8.** (A) Plots showing the concentrations of M(acac)<sub>x</sub> remaining in the reaction solution as a function of reaction time for one-shot injection of the precursor. (B) Plots showing the linear relationship between  $-\ln([M(acac)_x])$  and reaction time and the fittings based on the pseudo-first-order kinetics.

A colloidal synthesis typically involves the reduction of a metal precursor ( $M^{n+}$ ) by a reductant for the production of atoms, followed by their nucleation and growth into seeds and then nanocrystals [28]. At the beginning of a synthesis, the reduction kinetics should follow a second-order rate law because of the involvement of collision and electron transfer between the precursor and reductant molecules [29]. As such, the reduction rate is directly proportional to the concentrations of the precursor and reductant. When the reductant (*i.e.*, TTEG) is used in large excess relative to the precursor, the reduction can be approximated as a pseudo-first-order reaction, with the overall reaction rate ( $R$ ) being written as:

$$R = -d[M^{n+}]/dt = k_1 [M^{n+}] \quad (4.2)$$

where  $k_1$  is the rate constant. After the formation of seeds, the precursor can also be reduced on the surface of the just-formed seeds (denoted as  $S_x$ ). As such, the reduction of a precursor may follow two different pathways: reduction in the solution phase ( $M^{n+} + ne^- \rightarrow M$ , with a rate constant of  $k_1$ ) or autocatalytic reduction on the surface of the seeds ( $M^{n+} + S_x + ne^- \rightarrow S_xM$ , with a rate constant of  $k_2$ ) [30]. Taken together, the overall reduction rate involved in a nanocrystal synthesis can be expressed as:

$$R = k_1 [M^{n+}] + k_2 [S_x] [M^{n+}] \quad (4.3)$$

where  $[S_x]$  is the concentration of atoms presented on the surface of the seeds and the rate constants  $k_1$  and  $k_2$  correspond to the solution and surface reduction pathways, respectively.

In this study, I measured the reduction rate constants of the four precursors by injecting the precursor mixture into the growth solution containing poly(vinylpyrrolidone) (PVP), TTEG, and Rh seeds in one shot. In the presence of pre-formed Rh seeds, surface reduction should dominate the reduction process. Although the one-shot synthesis and dropwise synthesis would introduce different changes to the composition and shape of the seeds, here I assume the catalytic effects of the pre-formed seeds and the corresponding rate constants ( $k_2$ ) in both syntheses are the same, and do not change significantly as the reaction proceeds. I also assume that the concentration of the surface atoms,  $[S_x]$ , takes a fixed, known value in both cases throughout the synthesis. As such, it is feasible to obtain

$k_1$  and  $k_2$  by plotting the precursor concentration as a function of the reaction time and then fitting the data. For simplicity, the overall reduction rate can be written as:

$$R = k [M^{n+}] \quad (4.4)$$

where  $k = k_1 + k_2 [S_x]$ . In this case, the reduction rate law becomes:

$$\ln[M^{n+}]_t = -k t + \ln[M^{n+}]_0 \quad (4.5)$$

where  $[M^{n+}]_0$  and  $[M^{n+}]_t$  represent the concentrations of the precursor at the beginning of a synthesis and at a specific time point  $t$ , respectively. When  $-\ln[M^{n+}]_t$  was plotted as functions of reaction time in Figure 4.8B, straight lines were obtained, with the slopes corresponding to  $k$  values of each of the four redox reactions.

During one-shot synthesis, the concentration of a precursor in the reaction mixture can be expressed as:

$$c_t = c_0 e^{-kt} \quad (4.6)$$

where  $c_t$  represents the instantaneous concentration of a precursor in the reaction solution;  $c_0$  is the initial concentration of the precursor in the reaction solution;  $k$  is the reduction rate constant of the precursor derived from Figure 4.8B;  $t$  is the reaction time. In the case of dropwise addition as schematically illustrated in Figure 4.9A,  $c_t$  can be expressed as a sum of contributions from all the drops added up to this time point:

$$c_t = c_0 e^{-kt} + c_0 e^{-k(t-\tau)} + c_0 e^{-k(t-2\tau)} + \dots + c_0 e^{-k(t-N\tau)} = c_0 e^{-kt} (1 - e^{-Nk\tau + k\tau}) / (1 - e^{-k\tau}) \quad (4.7)$$

where  $c_0$  is the increase of concentration contributed by each drop;  $\tau$  is the interval of time between adjacent droplets; and  $N$  is the total number of droplets added into the solution up to time  $t$ .

According to Equation 4.4.7,  $c_t$  of a precursor in the reaction mixture is determined by  $k$ ,  $c_0$ , and  $\tau$ , and can be calculated for any combination of  $c_0$  and  $\tau$  if  $k$  is known. Figure 4.9B illustrates how  $c_t$  will change as a function of the reaction time. The instantaneous reduction rate ( $R_t$ ) is:

$$R_t = c_t k \quad (4.8)$$

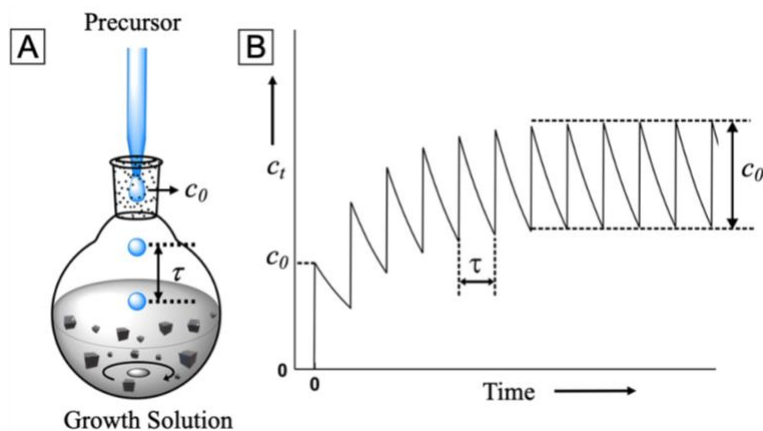


**Figure 4.9.** Mathematical description of the reduction process of a precursor during dropwise addition. (A) Schematic illustration of the experimental setup used for seed-mediated growth with the dropwise addition of a precursor. (B) Plot showing the instantaneous concentration ( $c_t$ ) of the precursor in the growth solution as a function of the reaction time ( $t$ ), the duration of time between adjacent drops ( $\tau$ ), and the increase of concentration contributed by each drop ( $c_0$ ). After the introduction of a certain number of drops,  $c_t$  will reach a steady state and only oscillate within a range defined by  $c_0$ . The plot was modified with permission from ref. [31]. Copyright 2015 American Chemical Society.

During dropwise addition of a precursor, the value of  $R_t$  will quickly reach a steady state, in which it will only fluctuate slightly between a lower limit ( $R_{low}$ ) and an upper limit

( $R_{up}$ ). In the steady state, when a droplet of the precursor solution is introduced,  $R_t$  will quickly increase from  $R_{low}$  to  $R_{up}$ , followed by decay from  $R_{up}$  to  $R_{low}$  until the next droplet is added.

After the establishment of steady state, the instantaneous reaction rate will be  $R_{up}$  when a new droplet is introduced into the reaction. The increase in reaction rate ( $c_0 \cdot k$ ) resulting from the addition of this new droplet should be equal to the decrease in reaction rate ( $R_{up} - R_{up} \cdot e^{-k\tau}$ ) in the following decay process until the next droplet is added. As such, we have:

$$c_0 \cdot k = R_{up} - R_{up} \cdot e^{-k\tau} = R_{up} (1 - e^{-k\tau}) \quad (4.9)$$

Therefore,  $R_{up}$  can be expressed as:

$$R_{up} = c_0 k / (1 - e^{-k\tau}) \quad (4.10)$$

Accordingly,  $R_{low}$  is the reaction rate at the end of this decay process:

$$R_{low} = R_{up} \cdot e^{-k\tau} = c_0 k e^{-k\tau} / (1 - e^{-k\tau}) \quad (4.11)$$

The average  $R_t$  ( $R_{avg}$ ) in the steady state can be calculated as the total area under the decay curve between two adjacent droplets divided by the duration of time ( $\tau$ ):

$$R_{avg} = \int_0^\tau R_{up} e^{-kt} dt / \tau = \{ \int_0^\tau [c_0 k / (1 - e^{-k\tau})] e^{-kt} dt \} / \tau = c_0 / \tau \quad (4.12)$$

Since the value of  $R_{avg}$  is only dependent on  $c_0$  and  $\tau$ , the reaction rates of all four precursors, that is,  $Ru(acac)_3$ ,  $Rh(acac)_3$ ,  $Pd(acac)_2$ , and  $Pt(acac)_2$ , should stay at

approximately the same level in the steady state regardless of their difference in reactivity (*i.e.*,  $k$  value). Figure 4.10A illustrates how the reduction rates of the four precursors changed as a function of time. In the initial stage, they all gradually increased, but at different paces. As the reaction proceeded, however, a steady state would be established, in which the reduction rates of all the precursors reaching approximately the same level. From this analysis, it is clear that dropwise addition can be used to ensure that the precursors are co-reduced at the same rate to achieve a composition close to nearly equimolar RuRhPdPt. For comparison, in the case of one-shot injection (Figure 4.10B), the reduction rates of the precursors are dependent on the values of  $k$ , so they tended to follow drastically different exponential decay curves because of their large difference in reactivity (*i.e.*,  $k$  value). The reaction rates of the precursors may differ by many folds at the beginning and the difference tend to vary as a function of the reaction time, leading to continuous variations to the compositions of the deposited shell.

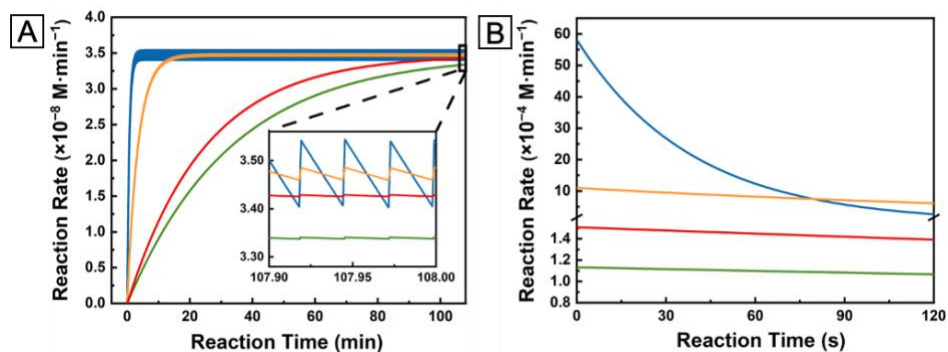


**Figure 4.10.** Simulated reaction rates as functions of reaction time in the cases of (A) dropwise injection and (B) one-shot injection of the precursor mixture, respectively. Inset in panel A: a segment of the curves in the last 0.1 min of the synthesis.

During the standard synthesis of Rh@alloy nanocubes, the total volume of the reaction solution containing TTEG, PVP, and Rh seeds was  $2.40 \times 10^{-3} \text{ L}$  at  $220 \text{ }^\circ\text{C}$ ; the

volume of each droplet was controlled at  $4.44 \times 10^{-6}$  L using a capillary; the concentration of each precursor in the precursor solution was  $5.0 \times 10^{-4}$  mol L<sup>-1</sup>; and the injection rate was set to  $1.67 \times 10^{-4}$  L min<sup>-1</sup>, thus:

$$c_0 = (4.44 \times 10^{-6} \text{ L}) \times (5.0 \times 10^{-4} \text{ mol L}^{-1}) / (2.40 \times 10^{-3} \text{ L}) = 9.25 \times 10^{-10} \text{ mol L}^{-1}$$

$$\tau = (4.44 \times 10^{-6} \text{ L}) / (1.67 \times 10^{-4} \text{ L min}^{-1}) = 2.66 \times 10^{-2} \text{ min}$$

Using these  $c_0$  and  $\tau$  values, as well as the  $k$  values measured using ICP-MS, the values of  $R_{up}$ ,  $R_{low}$ ,  $R_{avg}$  can be calculated using Equations 4.4.10, 4.4.11, and 4.4.12. As an example, for the reduction of Pd(acac)<sub>2</sub> precursor,  $k_{Pd} = 1.55$  min<sup>-1</sup>, thus:

$$\begin{aligned} R_{up,Pd} &= c_0 \cdot k / (1 - e^{-k\tau}) \\ &= (9.25 \times 10^{-10} \text{ mol L}^{-1}) \times (1.55 \text{ min}^{-1}) / [1 - e^{(-1.55 \text{ min}^{-1} \times 2.66 \times 10^{-2} \text{ min})}] \\ &= 3.550 \times 10^{-8} \text{ mol L}^{-1} \text{ min}^{-1} \end{aligned}$$

$$\begin{aligned} R_{low,Pd} &= c_0 \cdot k \cdot e^{-k\tau} / (1 - e^{-k\tau}) \\ &= (9.25 \times 10^{-10} \text{ mol L}^{-1}) \times (1.55 \text{ min}^{-1}) \times e^{(-1.55 \text{ min}^{-1} \times 2.66 \times 10^{-2} \text{ min})} / \\ &[1 - e^{(-1.55 \text{ min}^{-1} \times 2.66 \times 10^{-2} \text{ min})}] \\ &= 3.407 \times 10^{-8} \text{ mol L}^{-1} \text{ min}^{-1} \end{aligned}$$

$$\begin{aligned} R_{avg,Pd} &= c_0 / \tau \\ &= (9.25 \times 10^{-10} \text{ mol L}^{-1}) / (2.66 \times 10^{-2} \text{ min}) \end{aligned}$$

$$= 3.477 \times 10^{-8} \text{ mol L}^{-1} \text{ min}^{-1}$$

The  $R_{up}$ ,  $R_{low}$ , and  $R_{avg}$  values calculated for the four precursors are listed in Table 4.2.

**Table 4.2.**  $R_{up}$ ,  $R_{low}$ , and  $R_{avg}$  values calculated for the four precursors using Equations 4.4.10, 4.4.11, and 4.4.12 and experimental parameters in the standard protocol.

element	$k$ ( $\text{min}^{-1}$ )	reaction rate ( $10^{-8} \text{ mol L}^{-1} \text{ min}^{-1}$ )		
		$R_{up}$	$R_{low}$	$R_{avg}$
Ru	0.293	3.491	3.464	3.477
Rh	0.0302	3.479	3.476	3.477
Pd	1.55	3.550	3.407	3.477
Pt	0.0402	3.480	3.476	3.477

It is worth emphasizing that well-controlled reaction kinetics is only one of the many key prerequisites for the successful synthesis of Rh@A nanocrystals with a cubic shape and thereby {100} facets on the surface. As we do not have a universal capping agent to regulate the shape of nanocrystals with complex surface compositions, a physical template (*i.e.*, seed) is indispensable for controlling the shape taken by alloy nanocrystals. As shown in Figure 4.11, in the absence of Rh seeds to guide heterogeneous nucleation, different types of twin structures and various shapes, including cubes, rods, and irregular particles, were formed in the same batch of synthesis. As reported in the literature, multiple nucleation and growth mechanisms would be involved in the formation of such particles with diverse shapes and internal structures. The difference in reduction kinetics would also cause non-uniformity to the surface composition.

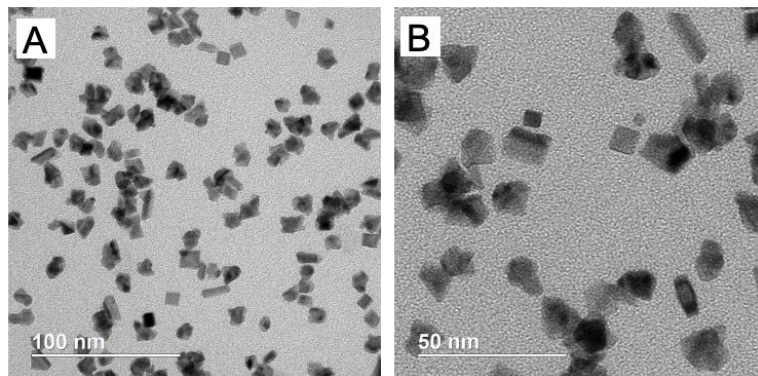


**Figure 4.11.** Influence of the pre-formed seeds. (A and B) TEM images of the products obtained using the standard protocol except for the absence of Rh seeds to direct heterogeneous nucleation. In this case, a variety of nanocrystals with different twin structures, shapes, morphologies, and compositions were formed, demonstrating the necessity to control the products with pre-formed seeds.

**Evaluation of the Thermal Stability.** The quaternary alloy nanocubes featuring a uniform distribution of elements and a well-controlled surface structure hold promise for a wide range of applications. For example, multi-metallic catalysts based on Rh, Pd, and Pt are widely employed in industry as advanced catalysts for reactions such as ammonia oxidation [4, 10], CO oxidation [32, 33], and NO<sub>x</sub> reduction [34, 35]. The introduction of Ru was reported to enhance the resistance to poisoning [34]. To evaluate the potential of the Rh@A cubes at elevated temperatures, I subjected them to *in situ* heating under HAADF-STEM. As shown in Figure 4.12, the cubic shape was well retained when heated up to 300 °C. At 400 °C, the terraces and steps on the side faces became slightly smoother due to the accelerated surface diffusion of atoms. Upon further heating to 500 °C, the particle evolved into a rounded cube, but the side faces were still dominated by {100} facets. Taken together, the Rh@A cubic nanocrystals could retain their {100} facets when heated up to 500 °C under vacuum. Moreover, the EDX data in Figure 4.13 indicated the cubic shell was still made of RhRuPdPt alloy after annealing at 500 °C for 30 min,

demonstrating excellent thermal stability of the Rh@A cubes in terms of both geometrical shape and elemental composition.

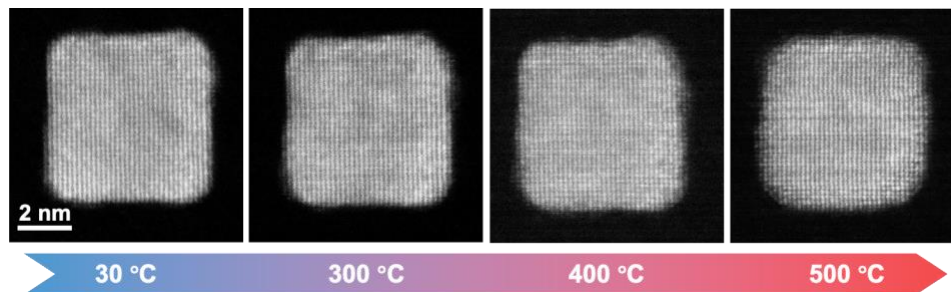


**Figure 4.12.** In situ HAADF-STEM images recorded from the same 6.6-nm core-shell cube at room temperature and then heated to 300 °C for 1 h, 400 °C for 30 min, and 500 °C for 30 min, respectively. The scale bar applies to all panels.

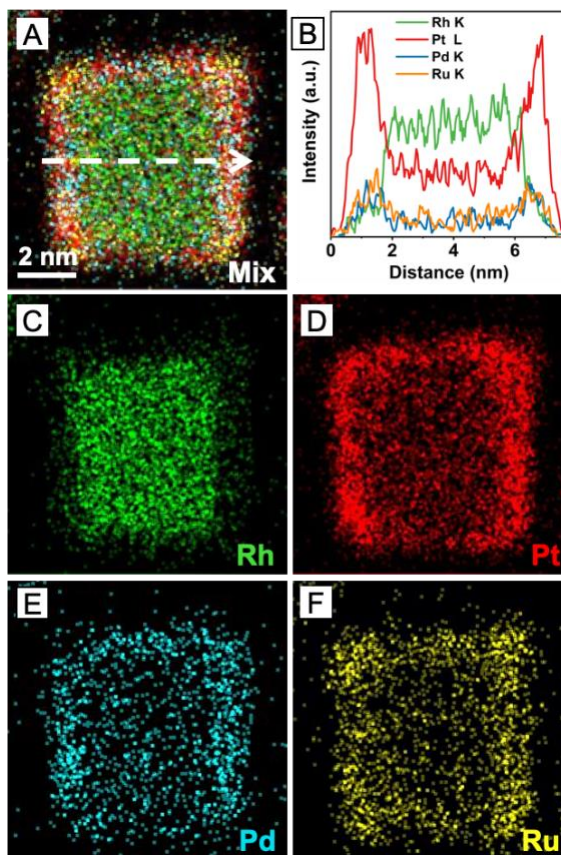


**Figure 4.13.** (A, C–F) EDX elemental mappings of a core-shell cube and (B) the corresponding line profiles of EDX intensities across the cube after annealing at 500 °C

for 30 min, showing the spatial distributions of Rh, Pt, Pd, and Ru. The scale bar applies to all panels.

**Evaluation of the Catalytic Performance.** Alloy nanoparticles made of PGMs have been utilized to effectively catalyze ethanol oxidation reaction (EOR), an anodic reaction pivotal to the operation of direct ethanol fuel cells [9]. As a complex 12-electron and 12-proton reaction, it requires the integration of multiple dehydrogenation and oxidation steps with cleavage of the C–C bond to have ethanol completely oxidized to CO<sub>2</sub>. In general, mono-metallic catalysts such as those based on Pd and Pt can only catalyze 4e-transfer processes to partially release the chemical energy stored in ethanol molecule [36, 37]. On the contrary, multi-metallic catalysts such as those based on Au@PtIr/C and PGM alloys have been demonstrated to be able to promote the 12e process with much higher efficiency [9, 38].

Prior to evaluating the catalytic performance of the as-prepared Rh@A cubes toward EOR, the electrochemical active surface areas (ECSAs) of the three catalysts were determined from charges associated with underpotentially deposited Cu for further analysis. The Cu stripping curves recorded in an aqueous electrolyte containing 0.5 M H<sub>2</sub>SO<sub>4</sub> and 5 mM CuSO<sub>4</sub> are shown in Figure 4.14. The ECSAs and total metal loadings of the three catalysts are provided in Table 4.3. I then benchmarked it against mono-metallic Pd cubes of a similar size (5.8 nm), as well as a commercial Pt/C catalyst. The CV curves recorded in 0.1 M HClO<sub>4</sub> are shown in Figure 4.15A. Note that the CV curve of Rh@A cubes is essentially featureless (with no specific voltametric peaks), indicating an alloy composition on the surface of the catalytic particles. Figure 4.15B shows the positive-going EOR polarization curves of the three catalysts recorded in an aqueous electrolyte

containing 1 M KOH and 1M ethanol, with that of Rh@A cubes exhibiting the highest specific activity ( $j_{\text{specific}}$ , normalized to ECSA), as well as the most negative oxidative peak potential relative to the other two catalysts. I further compared the  $j_{\text{specific}}$  values at 0.45 and 0.60 V *versus* reversible hydrogen electrode ( $V_{\text{RHE}}$ ) directly derived from the positive-going curves in Figure 4.15B (Figure 4.15C). At 0.45  $V_{\text{RHE}}$ , the Rh@A cubes showed a current density of 1.4 and 0.5 times higher than those of Pd cubes and Pt/carbon catalyst, respectively. The enhancement was more prominent at 0.60  $V_{\text{RHE}}$ , where the Rh@A cubes was 2.2 and 1.9 times more active than the Pd and Pt mono-metallic counterparts, respectively.

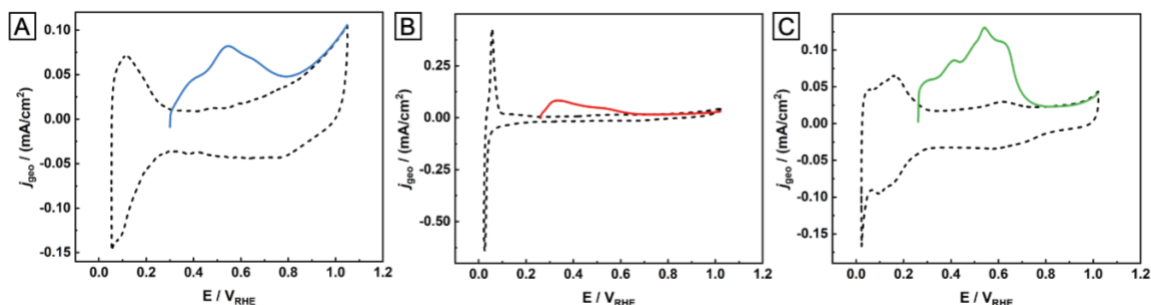


**Figure 4.14.** (A–C) Cyclic voltammetry curves (dashed lines, recorded in 0.5 M  $\text{H}_2\text{SO}_4$  at  $10 \text{ mV s}^{-1}$ ) and Cu stripping curves (solid lines, recorded in 0.5 M  $\text{H}_2\text{SO}_4$  and 5 mM  $\text{CuSO}_4$  at  $10 \text{ mV s}^{-1}$ ) of (A) Rh@A cubes, (B) Pd cubes, and (C) commercial Pt/carbon catalyst, respectively.

**Table 4.3.** The electrochemical active surface areas derived from underpotentially deposited Cu and the total metal loadings of the three catalysts.

Sample	Rh@A cubes	Pd cubes	Pt/carbon
ECSA ( $\text{cm}^2$ )	0.91	0.75	1.34
Mass ( $\mu\text{g}$ )	2.75	1.93	2.10
Specific ECSA ( $\text{m}^2/\text{g}$ )	33.1	38.9	63.8

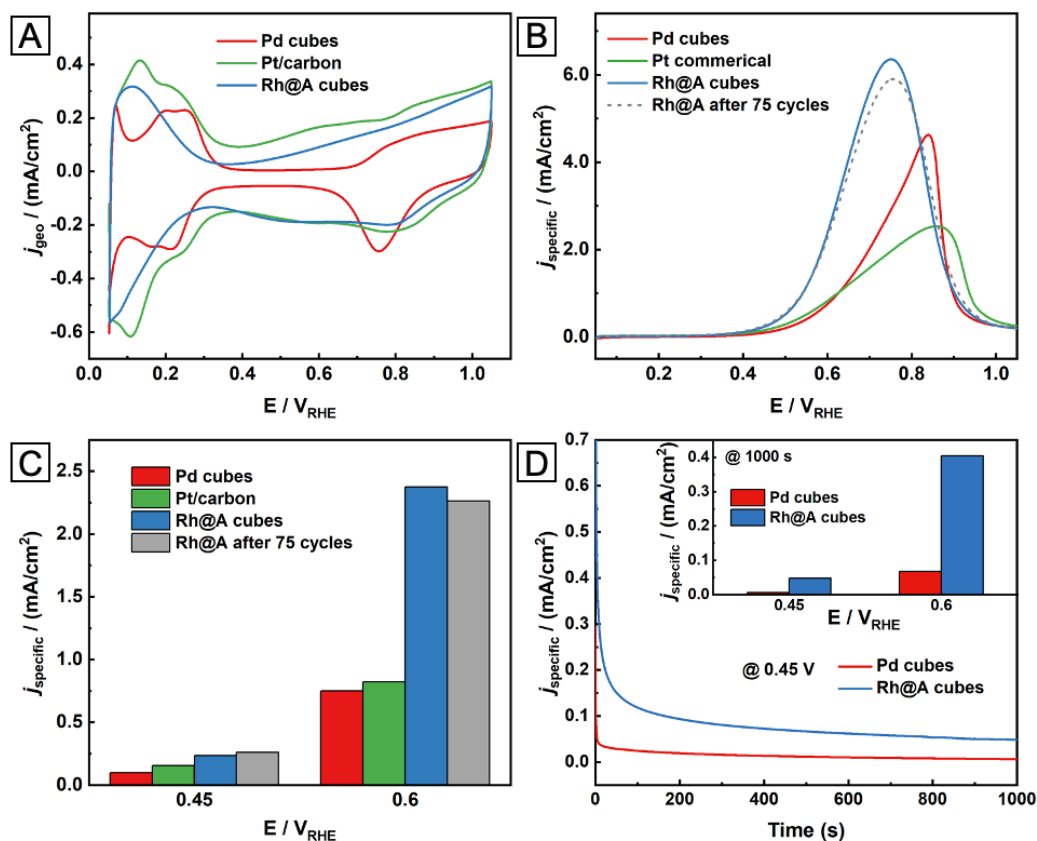
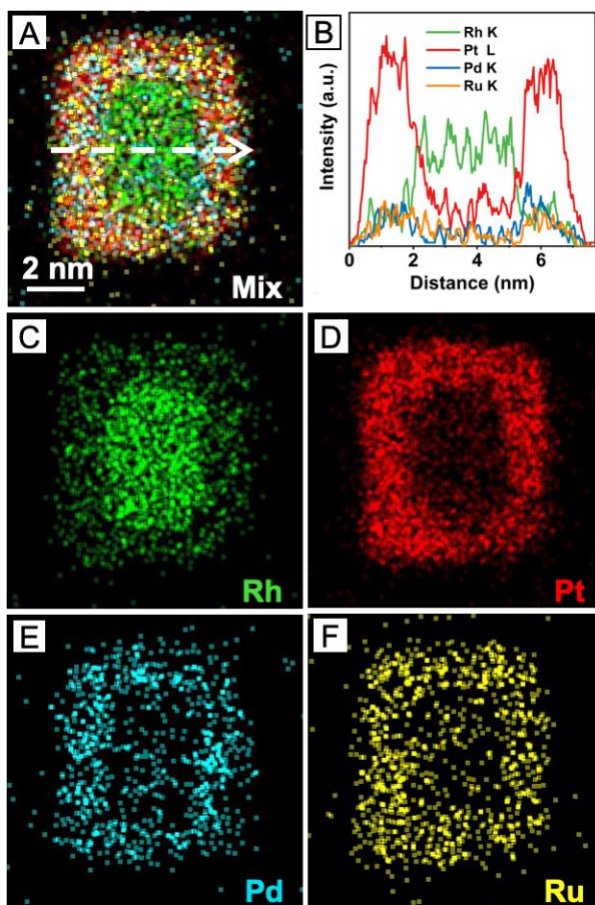


**Figure 4.15.** (A, B) Comparison of (A) CV curves and (B) EOR specific activities of three different catalysts. (C) Comparison of the specific activities of the three catalysts at potentials of 0.45 and 0.6  $V_{\text{RHE}}$  in the forward scan. (D) Stability test of Rh@A cubes and Pd cubes at a fixed potential of 0.45  $V_{\text{RHE}}$ . Inset in panel D: comparison of the steady state current densities at  $t = 1000$  s.

Remarkably, the high EOR activity of Rh@A cubes could be well retained even after 75 continuous CV scans in the aqueous electrolyte containing 1 M KOH and 1M ethanol (see the dashed curve in Figure 4.15B and grey columns in Figure 4.15C). Chronoamperometry was adopted to further demonstrate the superior catalytic durability of the alloy catalyst. I fixed the electrode potential at 0.45 and 0.60  $V_{\text{RHE}}$ , respectively, and monitored the current changes to the Rh@A cubes and Pd cubes over a period of 1000 s (Figure 4.15D and the inset). After 1000 s of cycling, the steady current densities of the Rh@A cubes were 7.6 (at 0.45  $V_{\text{RHE}}$ ) and 4.9 (at 0.60  $V_{\text{RHE}}$ ) times higher than those of Pd

cubes, respectively. To confirm the electrochemical stability of the Rh@A cubes in terms of both geometric shape and elemental composition, we conducted EDX mapping on the sample after 75 cycles of CV scanning in the aqueous electrolyte containing 1 M KOH and 1M ethanol. As shown in sFigure 4.16, the cubic shape and core–shell distribution of the elements were well-preserved during the electrochemical test. These results suggest that the alloy surface of the Rh@A cubes was stable enough to resist compositional and structural changes during the electrochemical measurement.



**sFigure 4.16.** EDX elemental mappings of a core–shell cube and the corresponding line profiles of EDX intensities across the cube after 75 cycles of CV scanning in the electrolyte containing 1 M KOH and 1 M ethanol, showing the spatial distributions of Rh, Pt, Pd, and Ru.

### 4.3 Conclusion

In summary, I have demonstrated a facile, robust method for the facet-controlled synthesis of multi-metallic nanocrystals. The success of this synthesis can be attributed to a number of factors, including the use of well-controlled and stable seeds to define the type of facet and thus surface atomic arrangement. The use of dropwise addition instead of one-shot injection allows me to keep the instantaneous reduction rates of different precursors in a similar range for the formation of an alloy with a uniform and consistent distribution in elemental composition. The multi-metallic shell of the nanocrystals significantly enhances their thermal and electrochemical stability without involving surface segregation or phase separation. It is anticipated that this facile, solution-phase method will find widespread use in the future exploration of multi-elemental noble-metal catalysts for various electro- and thermal-chemical reactions.

### 4.4 Experimental Section

**Chemicals and Materials.** Poly(vinylpyrrolidone) (PVP, with an average molecular weight of 55 000), potassium chloride (KCl, 99%), potassium bromide (KBr, 99%), hexachlororhodate ( $\text{Na}_3\text{RhCl}_6$ , 97%), rhodium(III) acetylacetonate ( $\text{Rh}(\text{acac})_3$ , 97%), ruthenium(III) acetylacetonate ( $\text{Ru}(\text{acac})_3$ , 97%), palladium(II) acetylacetonate ( $\text{Pd}(\text{acac})_2$ , 97%), platinum(II) acetylacetonate ( $\text{Pt}(\text{acac})_2$ , 97%), potassium hydroxide (KOH), tetraethylene glycol (TTEG, 99%), sulfuric acid ( $\text{H}_2\text{SO}_4$ , 99.999%), and copper(II) sulfate ( $\text{CuSO}_4$ , anhydrous powder, 99.99%) were all obtained from Sigma-Aldrich. Ethylene glycol (EG, 99%) was purchased from J. T. Baker. L-ascorbic acid (AA, 99%) was ordered from BioXtra. Ethanol ( $\text{C}_2\text{H}_5\text{OH}$ , anhydrous) was purchased from KOPTEC.

Perchloric acid ( $\text{HClO}_4$ , 70%, PPT grade) was purchased from GFS Chemicals. Acetone was obtained from VWR Chemicals BDH. Syringes and syringe pumps were acquired from KD Scientific. Capillary was purchased from Molex. The temperature of each synthesis was monitored using a thermal sensor acquired from ACE Glass. All aqueous solutions were prepared using deionized water with a resistivity of  $18.2 \text{ M}\Omega\cdot\text{cm}$  at room temperature.

**Synthesis of Rh Cubes.** I synthesized the 5.1-nm Rh cubes according to a protocol developed by my research group [22]. Typically, 13 mL of an EG solution containing AA (52.8 mg), KBr (108 mg), and PVP (133 mg) was transferred into a three-neck flask and heated at  $140 \text{ }^\circ\text{C}$  under magnetic stirring (600 rpm) for 1 h. Meanwhile, 6 mL of another EG solution containing 46.2 mg of  $\text{Na}_3\text{RhCl}_6$  was added into the flask at  $60 \text{ mL h}^{-1}$  for the first 1.1 mL and  $4 \text{ mL h}^{-1}$  for the remaining 4.9 mL, respectively. One hour after all the precursor solution had been added, the solid products were collected by precipitation with the addition of 60 mL of acetone, and then washed three times with a mixture of ethanol and acetone (1:3 v/v).

**Synthesis of Pd Cubes.** I synthesized the Pd cubes according to a protocol reported by my research group [39]. In a typical synthesis of 5.8-nm Pd cubes, 8.0 mL of an aqueous solution containing PVP (105 mg), AA (60 mg), KBr (5 mg), and KCl (185 mg) were placed in a 20-mL vial and pre-heated at  $80 \text{ }^\circ\text{C}$  for 10 min under magnetic stirring (400 rpm). Afterwards, 3.0 mL of an aqueous solution containing 57 mg of  $\text{Na}_2\text{PdCl}_4$  was added using a pipette. After the vial had been capped, the reaction was continued at  $80 \text{ }^\circ\text{C}$  for 3 h. The solid products were collected by centrifugation and washed three times with water, and then re-dispersed in water for further use.

**Synthesis of Rh@RuRhPdPt Alloy Nanocubes.** To avoid the reduction of precursors in a polyol prior to seed-mediated growth, acetone was used as a solvent to dissolve all the precursors, which quickly evaporated upon introduction into the reaction solution. In the standard protocol, 3.0 mg of the as-prepared 5.1-nm Rh cubes and 300 mg of PVP were mixed in 2 mL of TTEG. The mixture was then transferred into a 20-mL vial and heated at 220 °C for 10 min under magnetic stirring (400 rpm). Afterwards, 18 mL of an acetone solution containing Ru(acac)<sub>3</sub>, Rh(acac)<sub>3</sub>, Pd(acac)<sub>2</sub>, and Pt(acac)<sub>2</sub> (0.5 mM for each precursor) was added into the growth solution at a rate of 10 mL h<sup>-1</sup> using a syringe pump. The volume of each droplet was controlled at 4.4 μL using a capillary with an inner diameter of 50 μm. After all the precursor solution had been added, the reaction mixture was cooled down to room temperature and the solid products were collected by precipitation with acetone and washed three times with a mixture of ethanol and acetone (1:3 v/v).

**Instrumentation.** Transmission electron microscopy (TEM) images were taken using a Hitachi HT7700 microscope operated at 120 kV. High-angle annular dark-field scanning transmission electron microscopy (HAADF-STEM) images were acquired using an Cs-corrected Hitachi HD2700 STEM operated at 200 kV. Energy-dispersive X-ray spectroscopy (EDX) data were acquired using a Cs-corrected FEI Titan 80/300 kV TEM/STEM at Oak Ridge National Laboratory. X-ray diffraction (XRD) patterns were recorded on a PANalytical X'Pert PRO Alpha-1 diffractometer using a 1.8 kW ceramic copper tube source. The X-ray photoelectron spectroscopy (XPS) data were collected on a Thermo K-Alpha spectrometer with an Al K $\alpha$  source. Inductively-coupled plasma mass

spectrometry (ICP-MS, NexION 300Q, PerkinElmer) and XPS were used to determine the metal contents in the as-synthesized nanocrystals.

**Quantitative Analysis of Reduction Kinetics.** In a typical study, 0.1 mL aliquot was sampled from the reaction solution at different time points of a synthesis. The aliquot was then mixed with 9.9 mL of acetone to help precipitate out all the particles, followed by centrifugation to only leave behind the unreacted metal precursors in the supernatant. The supernatant was then collected and diluted for ICP-MS analysis.

**Evaluation of Thermal Stability.** The thermal stability of the nanocrystals was evaluated using Hitachi HD2700 STEM coupled with a Hitachi Blaze heating holder. An aqueous suspension of the as-prepared nanocrystals was drop-cast onto the MEMS Norcada heating chip with 30–50 nm-thick SiN<sub>x</sub> membrane and then allowed to dry under ambient conditions. The sample was then heated to and maintained at various temperatures in the range of 30–500 °C at a heating rate of 200 °C min<sup>-1</sup>.

**Preparation of the Catalysts.** In a typical process, 5 mg of carbon black (Vulcan XC-72) was dispersed in water and sonicated in an ice bath for 1 h, followed by the introduction of an aqueous suspension of the nanocrystals (*ca.* 1 mg). The mixture was sonicated in an ice bath for another 1 h and the resultant powder was collected by centrifugation at 10 000 rpm for 10 min. The catalyst was then dispersed in 5 mL of acetic acid and heated at 60 °C for 3 h to clean the surface of the catalytic particles and washed three times with ethanol. After that, the catalyst was dried in an oven held at 80 °C for 5 h.

**Electrochemical Measurements.** All electrochemical measurements were carried out in a three-electrode cell connected to a CHI 600E electrochemical workstation at room

temperature. Glassy carbon (GC, 5 mm in diameter) and Pt mesh ( $1 \times 1 \text{ cm}^2$ ) served as working and counter electrodes, respectively, for all measurements. Reversible hydrogen electrode (RHE, HydroFlex, Gasketel) served as a reference electrode for the CV scanning in aqueous electrolytes containing  $\text{HClO}_4$  or  $\text{KOH}$ . For Cu underpotential deposition (UPD), saturated calomel electrode was used as a reference electrode. Catalyst ink was prepared by mixing 2.5 mg of the dried carbon-supported nanocrystals, 10  $\mu\text{L}$  of Nafion (5 wt %, Aldrich), and 2.5 mL of ethanol in a glass vial and sonicated in an ice bath for 1 h. For each measurement, 10  $\mu\text{L}$  of the catalyst ink was dropped on a pre-cleaned GC electrode and dried at room temperature. In my discussion, unless otherwise specified, all potentials were presented with reference to RHE. All data were corrected with 85%  $iR$  compensation to account for the voltage drop between working electrode and reference electrode.

The catalyst was first cycled in an Ar-saturated  $\text{HClO}_4$  solution (0.1 M) between 0.05–1.05  $V_{\text{RHE}}$  at  $500 \text{ mV s}^{-1}$  for several hundred cycles until a stable cyclic voltammetry (CV) curve was obtained. CV curves were then recorded at a scan rate of  $50 \text{ mV s}^{-1}$  in the same aqueous electrolyte solution. The electrode was then cycled in an Ar-saturated solution containing 1 M  $\text{KOH}$  between 0.05–1.05  $V_{\text{RHE}}$  at a scan rate of  $500 \text{ mV s}^{-1}$  until the current density reached a stable value. Afterwards, the ethanol oxidation activity test was carried in a mixture of 1 M ethanol and 1 M  $\text{KOH}$  solution between 0.05–1.05  $V_{\text{RHE}}$  at a scan rate of  $50 \text{ mV s}^{-1}$ .

The electrochemical active surface areas (ECSAs) of the three catalysts were further determined using  $\text{Cu}_{\text{upd}}$  for analysis of catalytic performance [9]. Briefly, the electrode was first cycled in Ar-saturated 0.5 M  $\text{H}_2\text{SO}_4$  from 0.02–1.02  $V_{\text{RHE}}$  at a scan rate

of  $10 \text{ mV s}^{-1}$  after cleaning the electrode at  $500 \text{ mV s}^{-1}$  for several hundred cycles. Then, the potential was fixed at  $0.26 \text{ V}_{\text{RHE}}$  for 100 s in an Ar-saturated aqueous electrolyte containing  $0.5 \text{ M H}_2\text{SO}_4$  and  $5 \text{ mM CuSO}_4$ , followed by a linear scan from  $0.26\text{--}1.02 \text{ V}_{\text{RHE}}$  to collect the Cu UPD curve. The ECSAs were calculated by integrating the stripping charge of  $\text{Cu}_{\text{upd}}$  and subtracting the charge obtained under the same conditions in  $0.5 \text{ M H}_2\text{SO}_4$ , assuming a charge density of  $420 \mu\text{C cm}^{-2}$  for all the catalysts.

#### 4.5 Notes to Chapter 4

Part of this Chapter is adapted from the article “Facet-Controlled Synthesis of Platinum-Group-Metal Quaternary Alloys: The Case of Nanocubes and  $\{100\}$  Facets” published in *Journal of the American Chemical Society* [40].

#### 4.6 References

- [1] Kusada, K.; Wu, D.; Kitagawa, H. *Chem. Eur. J.* **2020**, *26*, 5105–5130.
- [2] Chen, P.-C.; Liu, X.; Hedrick, J. L.; Xie, Z.; Wang, S.; Lin, Q.-Y.; Hersam, M. C.; David, V. P.; Mirkin, C. A. *Science* **2016**, *352*, 1565–1569.
- [3] Kwon, S. G.; Krylova, G.; Phillips, P. J.; Klie, R. F.; Chattopadhyay, S.; Shibata, T.; Bunel, E. E.; Liu, Y.; Prakapenka, V. B.; Lee, B.; Shevchenko, E. V. *Nat. Mater.* **2015**, *14*, 215–223.
- [4] Yao, Y.; Huang, Z.; Xie, P.; Lacey, S. D.; Jacob, R. J.; Xie, H.; Chen, F.; Nie, A.; Pu, T.; Rehwoldt, M.; Yu, D.; Zachariah, M. R.; Wang, C.; Shahbazian-Yassar, R.; Li, J.; Hu, L. *Science* **2018**, *359*, 1489–1494.
- [5] Katiyar, N. K.; Nellaiappan, S.; Kumar, R.; Malviya, K. D.; Pradeep, K. G.; Singh, A. K.; Sharma, S.; Tiwary, C. S.; Biswas, K. *Mater. Today Energy* **2020**, *16*, 100393.
- [6] Tomboc, G. M.; Kwon, T.; Joo, J.; Lee, K. *J. Mater. Chem. A* **2020**, *8*, 14844–14862.

- [7] Xin, Y.; Li, S.; Qian, Y.; Zhu, W.; Yuan, H.; Jiang, P.; Guo, R.; Wang, L. *ACS Catal.* **2020**, *10*, 11280–11306.
- [8] Batchelor, T. A. A.; Pedersen, J. K.; Winther, S. H.; Castelli, I. E.; Jacobsen, K. W.; Rossmeisl, J. *Joule* **2019**, *3*, 834–845.
- [9] Wu, D.; Kusada, K.; Yamamoto, T.; Toriyama, T.; Matsumura, S.; Kawaguchi, S.; Kubota, Y.; Kitagawa, H. *J. Am. Chem. Soc.* **2020**, *142*, 13833–13838.
- [10] Liu, X.; Han, Y.; Jia, H. *Rare Met. Mater. Eng.* **2017**, *46*, 339–343.
- [11] Kumar, N.; Tiwary, C. S.; Biswas, K. *J. Mater. Sci.* **2018**, *53*, 13411–13423.
- [12] Gao, S.; Hao, S.; Huang, Z.; Yuan, Y.; Han, S.; Lei, L.; Zhang, X.; Shahbazian-Yassar, R.; Lu, J. *Nat. Commun.* **2020**, *11*, 2016.
- [13] Chen, P.-C.; Liu, G.; Zhou, Y.; Brown, K. A.; Chernyak, N.; Hedrick, J. L.; He, S.; Xie, Z.; Lin, Q.-Y.; Dravid, V. P.; O’Neill-Slawecki, S. A.; Mirkin, C. A. *J. Am. Chem. Soc.* **2015**, *137*, 9167–9173.
- [14] Waag, F.; Li, Y.; Ziefuß, A. R.; Bertin, E.; Kamp, M.; Duppel, V.; Marzun, G.; Kienle, L.; Barcikowski, S.; Gökce, B. *RSC Adv.* **2019**, *9*, 18547–18558.
- [15] Liu, M.; Zhang, Z.; Okejiri, F.; Yang, S.; Zhou, S.; Dai, S. *Adv. Mat. Interfaces* **2019**, *6*, 1900015.
- [16] Broge, N. L. N.; Bondesgaard, M.; Søndergaard-Pedersen, F.; Roelsgaard, M.; Iversen, B. B. *Angew. Chem. Int. Ed.* **2020**, *59*, 21920–21924.
- [17] Bondesgaard, M.; Broge, N. L. N.; Mamakhel, A.; Bremholm, M.; Iversen, B. B. *Adv. Funct. Mater.* **2019**, *29*, 1905933.
- [18] Bueno, S. L.; Lenoardi, A.; Kar N.; Chatterjee, K.; Zhan, X.; Chen, C.; Wang, Z.; Engel, M.; Fung, V.; Skrabalak, S. E. *ACS Nano* **2022**, *16*, 18873–18885.
- [19] Tao, L.; Sun, M.; Zhou, Y.; Luo, M.; Lv, F.; Li, M.; Zhang, Q.; Gu, L.; Huang, B.; Guo, S. A. *J. Am. Chem. Soc.* **2022**, *144*, 10582–10590.
- [20] Shi, Y.; Lyu, Z.; Zhao, M.; Chen, R.; Nguyen, Q. N.; Xia, Y. *Chem. Rev.* **2021**, *121*, 649–735.
- [21] Xia, Y.; Gilroy, K. D.; Peng, H.-C.; Xia, X. *Angew. Chem. Int. Ed.* **2016**, *56*, 60–95.

- [22] Zhao, M.; Chen, Z.; Shi, Y.; Hood, Z. D.; Lyu, Z.; Xie, M.; Chi, M.; Xia, Y. *J. Am. Chem. Soc.* **2021**, *143*, 6293–6302.
- [23] Zhang, H.; Li, W.; Jin, M.; Zeng, J.; Yu, T.; Yang, D.; Xia, Y. *Nano Lett.* **2011**, *11*, 898–903.
- [24] Lide, D. *CRC Handbook of Chemistry and Physics*, 84th ed.; CRC Press: Boca Raton, FL, 2003; Vol. 9, pp 52–64.
- [25] Zheng, Y.; Zeng, J.; Ruditskiy, A.; Liu, M.; Xia, Y. *Chem. Mater.* **2013**, *26*, 22–33.
- [26] Zhan, C.; Xu, Y.; Bu, L.; Zhu, H.; Feng, Y.; Yang, T.; Zhang, Y.; Yang, Z.; Huang, B.; Shao, Q.; Huang, X. *Nat. Commun.* **2021**, *12*, 6261.
- [27] Wu, D.; Kusada, K.; Nanba, Y.; Koyama, M.; Yamamoto, T.; Toriyama, T.; Matsumura, S.; Seo, O.; Gueye, I.; Kim, J.; Kumara, L. S. R.; Sakata, O.; Kawaguchi, S.; Kubota, Y.; Kitagawa, H. *J. Am. Chem. Soc.* **2022**, *144*, 3365–3369.
- [28] Rodrigues, T. S.; Zhao, M.; Yang, T.-H.; Gilroy, K. D.; da Silva, A. G. M.; Camargo, P. H. C.; Xia, Y. *Chem. Eur. J.* **2018**, *24*, 16944–16963.
- [29] Luty-Błoch, M.; Pačławski, K.; Wojnicki, M.; Fitzner, K. *Inorg. Chim. Acta* **2013**, *395*, 189–196.
- [30] Yang, T.-H.; Peng, H.-C.; Zhou, S.; Lee, C.-T.; Bao, S.; Lee, Y.-H.; Wu, J.-M.; Xia, Y. *Nano Lett.* **2017**, *17*, 334–340.
- [31] Peng, H.-C.; Park, J.; Zhang, L.; Xia, Y. *J. Am. Chem. Soc.* **2015**, *137*, 6643–6652.
- [32] Westerström R.; Wang, J. G.; Ackermann, M. D.; Gustafson, J.; Resta, A.; Mikkelsen A.; Andersen, J. N.; Lundgren, E.; Balmes, O.; Torrelles, X. *J. Phys.: Condens. Matter.* **2008**, *20*, 184018.
- [33] Kang, S. B.; Han, S. J.; Nam, I.-S.; Cho, B. K.; Kim, C. H.; Oh, S. H. *Chem. Eng. J.* **2014**, *241*, 273–287.
- [34] Taylor, K. C.; Schlatter, J. C. *J. Catal.* **1980**, *63*, 53–71.
- [35] Chernyshov, B. V. I.; Kisil, I. M. *Platin. Met. Rev.* 1993, *37*, 136–143.
- [36] Fang, X.; Wang, L.; Shen, P.-K.; Cui, G.; Bianchini, C. *J. Power Sources* **2010**, *195*, 1375–1378.

- [37] Lai, S.; Koper, M. *J. Phys. Chem. Lett.* **2010**, *1*, 1122–1125.
- [38] Liang, Z.; Song, L.; Deng, S.; Zhu, Y.; Stavitski, E.; Adzic R. R.; Chen, J.; Wang, J. *J. Am. Chem. Soc.* **2019**, *141*, 9629–9636.
- [39] Jin, M.; Liu, H.; Zhang, H.; Xie, Z.; Liu, J.; Xia, Y. *Nano Res.* **2011**, *4*, 83–91.
- [40] Wang, C.; Huang Z.; Ding, Y.; Xie, M.; Chi, M.; Xia, Y. *J. Am. Chem. Soc.* **2023**, *145*, 2553–2560.

## CHAPTER 5. CONCLUSIONS AND FUTURE DIRECTIONS

### 5.1 Conclusions

This dissertation concentrates on the application of a combined approach involving seed-mediated growth and dropwise injection of precursor for the synthesis of noble-metal nanocrystals with precise control over their sizes, morphologies, and compositions, which were then evaluated for biomedical and catalytic applications. The first project delves into the manipulation of Au nanoparticle's nucleation and growth behaviors on the surface of amorphous Se nanosphere through a galvanic replacement reaction. The as-obtained Se–Au hybrid nanostructures with a spectrum of morphologies showed enhanced cellular uptake efficiency and cytotoxicity. The second project showcases the successful synthesis of Pd@Rh cubic nanocrystals with a smooth Rh shell and augmented stability for the fabrication of Rh nanocages. The third project demonstrates the versatility of the two synthetic strategies in controlling the size, morphology, and composition of complex multi-metallic alloy nanocrystals.

Specifically, I investigated the decisive role played by the initial reduction rate in directing the heterogeneous nucleation and growth behavior of Au on *a*-Se nanospheres. By varying the initial pH value of the reaction solution from 8.2 to 11.7 through the addition of NaOH, the galvanic replacement reaction between Se and Au precursor was gradually accelerated. This led to an increased number of nucleation sites on each *a*-Se nanosphere, resulting in the formation of 1 to 2, 3, 10, and more than 10 Au nanoparticles. These Au nanoparticles exhibited polycrystalline structures and irregular shapes. The distinct nucleation patterns gave rise to the generation of Se–Au hybrid nanoparticles with diverse

morphologies. Following the conjugation of ligands to the surface of the Au nanoparticles, the hybrid nanoparticles were evaluated for their potential as therapeutic agents in cancer nanomedicine. The findings indicated that Se–Au hybrid nanoparticles with a larger number of Au nanoparticles on the surface, thus more uniform distribution of ligands, exhibited enhanced cellular internalization efficiency. Consequently, these nanoparticles induced a more significant reduction in cell viability, ultimately leading to cell death. By uncovering new insights into the kinetically-controlled nucleation process involving a metal precursor and an amorphous surface, this work provides a new pathway for the design and rational synthesis of hybrid nanomaterials for biomedical applications.

Transitioning from mono- to bi-metallic system, I controlled the deposition of Rh overlayers on Pd cubic nanocrystals through polyol reduction and slow dropwise injection of Rh precursor. By carefully optimizing a series of kinetic parameters including reaction temperature, injection rate of precursor, and the inclusion of bromide ligand, the deposition mode was tailored to proceed in a layer-by-layer fashion, as opposed to island growth or homogeneous nucleation. The thickness of the Rh shell could be adjusted from 0.6 to 1.5 and 3.0 atomic layers by simply varying the amount of Rh precursor added from 1 to 3 and 5 mL. The complete coating of Pd nanocubes by the Rh shell was demonstrated through electrochemical characterization. Notably, the Rh shell significantly improved the thermal stability of the cubic shape, withstanding heating up to 300 °C, as established by *in situ* TEM observation. Furthermore, Rh nanocages with ultrathin walls could be readily fabricated through wet etching of Pd core from the Pd@Rh nanocrystals.

Taking a leap forward, I further explored the composition control for complex multi-metallic nanocrystals. Building upon the insights gained from the previous two

projects, which encompassed the significance of reaction temperature, template, injection rate, and precursor type, I developed a robust synthetic protocol for the generation of core-shell nanocrystals consisting of a 5.1-nm Rh cube as the core and a well-controlled RuRhPdPt quaternary alloy as the shell. The success of this synthesis hinged upon several key factors. Firstly, a high reaction temperature coupled with a slow injection rate of the precursor facilitated the surface atomic diffusion while controlling the reaction kinetics of each precursor. Additionally, the use of Rh cubic template with exceptional thermal stability supported synthesis at a high temperature, whereas halide-free acetylacetonate precursors were chosen to prevent oxidative etching. This rationally-designed combination of conditions and precursors played a pivotal role in achieving the desired outcome. The resulting alloy nanocubes exhibited remarkable thermal stability, maintaining both their shape and composition up to 500 °C. Moreover, they demonstrated enhanced catalytic performance toward ethanol oxidation when benchmarked against Pd nanocubes and commercial Pt/carbon catalyst.

Overall, my research offers a range of synthetic strategies for the production of noble-metal nanocrystals with precise control over their sizes, morphologies, and compositions, spanning mono-, bi-, and multi-metallic systems. Leveraging the availability of state-of-the-art analytical techniques, including *in situ* TEM and ICP-MS, I further explored the potential applications of these nanomaterials in the fields of biomedicine and heterogeneous catalysis. These studies not only offer facile approaches to nanomaterials synthesis but also reveal the mechanisms underlying their formation, providing guidelines for the rational synthesis of complex and multifunctional nanostructures.

## 5.2 Future Directions

The synthetic protocols and knowledge established in this dissertation seek to facilitate rational design and engineering of the size, morphology, and composition of noble-metal nanocrystals for the achievement of improved performance in biomedicine and catalysis. Despite significant accomplishments, several challenges and opportunities still demand future attention before the potential of these nanomaterials can be fully harnessed. In the following discussion, I provide a concise discussion of potential directions that call for further exploration, with the intention of inspiring readers to embark on new research projects within this dynamic field.

1. Advancement in Characterization Techniques. While this dissertation has extensively discussed the synthetic mechanisms and growth pathways of various nanostructures, such as Se–Au hybrid nanoparticles, Pd@Rh core–shell nanocubes, and Rh@alloy nanocrystals, it is important to acknowledge the limitations of indirect empirical observations through *ex situ* characterization techniques such as TEM imaging and ICP-MS elemental analysis. The conclusions drawn from these observations may not always be entirely accurate. This issue is deeply rooted in two factors. First, the weak coupling between the structural features of a nanocrystal and trackable physical properties (*e.g.*, optical absorption and nuclear magnetic resonances, among others) poses challenges in identifying and monitoring the intermediate products, especially in syntheses involving fast kinetics. In addition, the variations among particles within the same batch of product due to random or systematic influences further complicate the analysis. These challenges call for the development of techniques capable of directly observing the shape evolution of individual particles *in situ* and in real time. Advanced characterization techniques hold

great promise in revealing intricate and concealed details of the formation process of a nanocrystal. Noteworthy tools include liquid-cell TEM that enables direct and rapid imaging in the solution phase [1–3], three-dimensional electron tomography that offers visualization of the spatial distribution of each element within a single particle [4–6], and probe-based spectroscopic methods that are capable of *in situ* and real-time detection on large scale [7, 8].

2. Scale-up Production. The utilization of nanomaterials in various application requires their production in a scalable and cost-effective manner without compromising their qualities. The studies conducted in this dissertation primarily focused on batch synthesis typically conducted in small-scale reactors such as 20-mL vials or 50-mL flasks. However, the limited quantity of particles generated, typically less than 10 mg per batch, is insufficient for industrial applications. In general, it is impractical to scale up the production of colloidal nanocrystals by simply increasing the reagent amount in larger reactors due to spatial/temporal heterogeneity in temperature and chemical composition, which can cause severe deterioration to product quality [9]. To address this issue, we need a scalable platform that can be operated in both small and large volumes under nearly identical conditions for the purposes of parameter optimization and high-volume production, respectively. The widely applied continuous flow system could not be directly adopted into the protocols developed here [10]. This is because all the three projects relied on the gradual dropwise injection of precursor into the reaction solution to achieve a precise kinetic control over different attributes of the product. Therefore, the development of a novel system for high-throughput production is necessary to better accommodate the requirement for slow and controlled introduction of chemicals.

3. Practical Assessment through Real-World Testing. The evaluation of the thermal, biomedical, and catalytic properties of the nanomaterials prepared in the present studies primarily took place in controlled laboratory environments. For example, the thermal stability test involved loading the sample onto a SiN<sub>x</sub> substrate and subjecting it to heating in vacuum under electron beam exposure for TEM analysis. However, it is important to note that the physical and chemical environments in these experiments differ from those encountered in practical scenarios, where factors such as reactive gaseous, moisture, and substrate may hasten structural degradation [11]. In the future, these nanomaterials should be comprehensively assessed in a laboratory setup that more closely resembles real-world conditions in order to acquire comparable data and thus better evaluate their potential in the targeted applications.

### 5.3 Notes to Chapter 5

Part of this Chapter is adapted from “Colloidal Synthesis of Metal Nanocrystals: From Asymmetrical Growth to Symmetry Breaking” published in *Chemical Reviews* [12], “Bi-metallic Core–Shell Nanocrystals: Opportunities and Challenges” published in *Nanoscale Horizons* [13], “Controlling the Nucleation and Growth of Gold on Amorphous Selenium Nanospheres to Enhance Their Cellular Uptake and Cytotoxicity” published in *Journal of the American Chemical Society* [14], “Synthesis of Pd@Rh Nanocubes with Well-Defined {100} Surface and Controlled Shell Thicknesses for the Fabrication of Rh Nanocages” published in *Surface Science* [15], and “Facet-Controlled Synthesis of Platinum-Group-Metal Quaternary Alloys: The Case of Nanocubes and {100} Facets” published in *Journal of the American Chemical Society* [16].

## 5.4 References

- [1] Liao, H.-G.; Zheng, H. *Annu. Rev. Phys. Chem* **2016**, *67*, 719–747.
- [2] Shi, F.; Li, F.; Ma, Y.; Zheng, F.; Feng, R.; Song, C.; Tao, P.; Shang, W.; Deng, T.; Wu, J. *ChemNanoMat* **2019**, *5*, 1439–1455.
- [3] Chee, S. W.; Pratt, S. H.; Hattar, K.; Duquette, D.; Ross, F. M.; Hull, R. *Chem. Commun.* **2015**, *51*, 168–171.
- [4] Jenkinson, K.; Liz-Marzán, L. M.; Bals, S. *Adv. Mater.* **2022**, *34*, 2110394.
- [5] Mychinko, M.; Skorikov, A.; Albrecht, W.; Sanchez-Iglesias, A.; Zhuo, X.; Kumar, V.; Liz-Marzan, L. M.; Bals, S. *Small* **2021**, *17*, e2102348.
- [6] Skorikov, A.; Albrecht, W.; Bladt, E.; Xie, X.; van der Hoeven, J. E. S.; van Blaaderen, A.; Van Aert, S.; Bals, S. *ACS Nano* **2019**, *13*, 13421–13429.
- [7] Wu, Y.; Qin, D. *J. Am. Chem. Soc.* **2018**, *140*, 8340–8349.
- [8] Ding, K.; Cullen, D. A.; Zhang, L.; Cao, Z.; Roy, A. D.; Ivanov, I. N.; Cao, D. *Science* **2018**, *362*, 560–564.
- [9] Sebastian, V. *Nanoscale* **2022**, *14*, 4411–4447.
- [10] Liu, G. Zhang, L.; Ruditskiy, A.; Wang, L.; Xia, Y. *Nano Lett.* **2018**, *18*, 3879–3884.
- [11] Ye, F.; Xu, M.; Dai, S.; Tieu, P.; Ren, X.; Pan, X. *Catalysts* **2020**, *10*, 779.
- [12] Nguyen, Q. N.; Wang, C.; Shang, Y.; Janssen, A.; Xia, Y. *Chem. Rev.* **2023**, *123*, 3693–3760.
- [13] Wang, C.; Shi, Y.; Qin, D.; Xia, Y. Bi-metallic Core–Shell Nanocrystals: Opportunities and Challenges. *Nanoscale Horiz.* **2023**, DOI: 10.1039/D3NH00098B.
- [14] Cheng, H.; Wang, C.; Lyu, Z.; Zhu, Z.; Xia, Y. *J. Am. Chem. Soc.* **2023**, *145*, 1216–1226.
- [15] Wang, C.; Lyu, Y.; Xia, Y. *Surf. Sci.* **2023**, 736, 122339.

[16] Wang, C.; Huang Z.; Ding, Y.; Xie, M.; Chi, M.; Xia, Y. *J. Am. Chem. Soc.* **2023**, *145*, 2553–2560.